Chem Soc Rev

REVIEW ARTICLE

View Article Online
View Journal | View Issue

Cite this: *Chem. Soc. Rev.*, 2025, **54**, 9939

Single-crystal perovskites for photovoltaic and high-energy detection applications

Bingyao Shao, †[a] Xin Song, †[a] Hongwei Zhu, †[a] Youcef A. Bioud,†[a] Wentao Wu,[a] Mutalifu Abulikemu,[a] Hamad Saiari,[b] Sarah Aqeel,[b] Issam Gereige,[b] Omar F. Mohammed *[a] and Osman M. Bakr *[a]

Received 3rd June 2025

DOI: 10.1039/d5cs00625b

rsc.li/chem-soc-rev

Metal halide perovskites have garnered widespread attention for optoelectronic applications, owing to their high optical absorption coefficients, tunable bandgaps, long carrier diffusion lengths, and high carrier mobilities. Their compatibility with simple, low-temperature processing methods further establishes them as promising next-generation semiconductors. However, the numerous defects present in the bulk and at the interfaces of polycrystalline perovskites lead to poor stability, hindering their commercialization. In contrast, single-crystal (SC) perovskites contain far fewer defects and thus exhibit inherently superior stability and optoelectronic properties, making them a promising platform for developing advanced perovskite-based devices. This review provides a comprehensive analysis of the advantages of SC perovskites, evaluates the merits and limitations of various crystal growth methods, and highlights their use in photovoltaics and high-energy radiation detection. Finally, we discuss the challenges that hinder the practical implementation of SC perovskites and propose strategies to facilitate their large-scale commercialization.

1. Introduction

Metal halide perovskites have a three-dimensional crystal structure formed by corner-sharing BX_6^- octahedra, with the chemical formula ABX_3 (Fig. 1A), where A is a monovalent metal or organic cation (*e.g.*, Cs^+, formamidinium (FA^+), or methylammonium (MA^+)),[1–3] B is a divalent metal cation (*e.g.*, Pb^{2+} or Sn^{2+}),[4–6] and X is a halide anion (*e.g.*, Cl^-, Br^-, or I^-).[7,8] Based on dimensionality and symmetry, perovskites can be classified into three-dimensional (3D), two-dimensional (2D), one-dimensional (1D), and zero-dimensional (0D) structures, each exhibiting unique structural and optoelectronic properties.[9–13] Compared to traditional inorganic semiconductors, perovskites exhibit superior optoelectronic properties and greater versatility

[a] *Center for Renewable Energy and Storage Technologies (CREST), King Abdullah University of Science and Technology, Thuwal 23955-6900, Kingdom of Saudi Arabia. E-mail: omar.abdelsaboor@kaust.edu.sa, osman.bakr@kaust.edu.sa*
[b] *Aramco Research Center, King Abdullah University of Science and Technology, Thuwal 23955-6900, Kingdom of Saudi Arabia*
† These authors contributed equally.

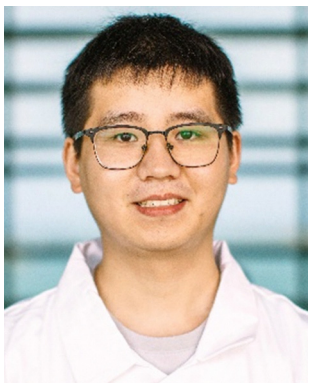

Bingyao Shao

Bingyao Shao received his BS and MS degrees from the University of Electronic Science and Technology of China (UESTC) in 2017 and 2020, respectively. He obtained his PhD in Materials Science and Engineering in 2025 under the supervision of Prof. Osman M. Bakr at King Abdullah University of Science and Technology (KAUST), where his research focused on perovskite-based optoelectronic devices.

Xin Song

Xin Song is currently a postdoctoral fellow at the Center for Renewable Energy and Storage Technologies (CREST), King Abdullah University of Science and Technology (KAUST) with Prof. Osman and Prof. Omar. She earned her PhD in Materials Science from Shaanxi Normal University with Prof. Shengzhong (Frank) Liu and Prof. Kui Zhao in 2021. Her research interests focus on growth of new perovskite single crystals, their structure–property relations, and applications for X-ray devices.

across a wide range of applications, including in solar cells,[14–16] light-emitting diodes (LEDs),[17–19] lasers,[20,21] high-energy (*e.g.*, X-ray and gamma-ray) radiation detectors,[22–24] and scintillators.[25,26]

To date, most high-performance perovskite optoelectronic devices are fabricated using polycrystalline films, which—despite their ease of fabrication and high efficiency—suffer from intrinsic stability limitations that hinder the commercialization of perovskite technologies.[27–29] The inferior stability arises from the formation of defects during crystallization, which are primarily concentrated at the grain boundaries and surfaces of the perovskite,[30–35] these defects can accelerate the degradation of the perovskite under external stressors such as moisture, heat, oxygen, bias voltage, and light.[36–39] To address these issues, numerous studies have focused on crystallization control and post-processing techniques for defect passivation.[40–43] However, even after passivation, polycrystalline perovskites still exhibit a defect density that is several orders of magnitude higher than that of single-crystal (SC) perovskites, making SC growth essential for fundamentally enhancing the stability of perovskite-based optoelectronic devices.

This review sheds light on the distinct optoelectronic properties and superior stability of SC perovskites and provides a comprehensive discussion of various SC growth methods aimed at achieving high-quality, tailored, and scalable SC materials for diverse applications. It is followed by a systematic presentation of strategies related to device architecture and SC material innovations to advance the application of SC perovskites in photovoltaic devices and high-energy radiation detection. Finally, we discuss the key challenges and potential strategies concerning the long-term operational stability of SC

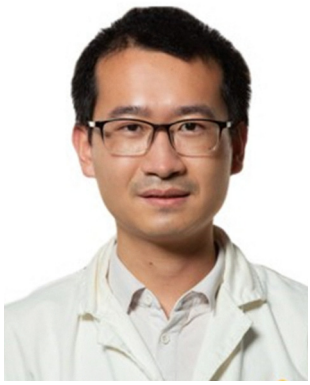

Hongwei Zhu

Hongwei Zhu received his BS degree from Tiangong University in 2014 and his MS and PhD degrees from Tianjin University in 2021. He is currently a postdoctoral fellow (2021–2024) and a research scientist (2024-present) at King Abdullah University of Science and Technology (KAUST). His research mainly focuses on the development of high-performance perovskite-based solar cells.

Youcef A. Bioud

Youcef A. Bioud is a postdoctoral researcher at KAUST's Center for Renewable Energy and Storage Technologies (CREST), where he develops multi-band infrared imagers monolithically integrated onto CMOS circuits. Previously, he was a visiting researcher at Fraunhofer ISE (Germany) and research coordinator at the Institut Quantique (Canada). He holds a PhD in Electrical Engineering (Sherbrooke) and a Master's in Physics (Rennes 1), and completed a research stay at École polytechnique (Paris). His honors include the DAAD Fellowship, the Jean Capelle Medal, and the FRQNT Relève étoile award. His research focuses on nano/microfabrication, scalable heterogeneous integration, infrared optoelectronics, and solar energy.

Omar F. Mohammed

Omar F. Mohammed is a Professor of Materials Science and Engineering at KAUST. He received his PhD degree in Physical Chemistry from Humboldt University of Berlin, Germany. His research group focuses on the development of highly efficient solar cells materials, as well as X-ray imaging scintillators and detectors for high resolution and low dose X-ray medical diagnostic and security checks. He is a Fellow of the Royal Society of Chemistry, a Fellow of the Institute of Physics and a Clarivate Highly Cited Researcher from 2019–2024.

Osman M. Bakr

Osman M. Bakr is a Professor of Materials Science and Engineering and Associate Vice President of Research at KAUST, and serves as Executive Editor for ACS Materials Letters. He received his BSc from MIT and PhD in Applied Physics from Harvard University. His research group focuses on the design, synthesis, and self-assembly of hybrid organic–inorganic semiconductors, including perovskites and quantum dots, for optoelectronic and renewable energy applications. He is the founder of Quantum Solutions, a company developing optoelectronic devices. His contributions have been recognized with the Kroll Medal & Prize, the Kuwait Prize, and recognition as a Clarivate Highly Cited Researcher.

perovskites, as well as their prospects in flexible device applications.

2. Properties and advancements in SC perovskites

Fig. 1B illustrates the development timeline of SC perovskite materials and their representative applications in photovoltaics and high-energy radiation detection. The hybrid organic–inorganic halide perovskite with the chemical formula $CH_3NH_3PbX_3$ (X = Cl, Br, I) was first reported in 1978.[57] Since then, halide perovskites with various compositions have been developed and widely applied in optoelectronics.[58] In 2009, metal halide perovskites were introduced as visible-light sensitizers in dye-sensitized solar cells,[45] a development that subsequently evolved into the next-generation photovoltaic technology of perovskite solar cells (PSCs).[46,59,60] However, the adoption of SC perovskites in optoelectronic devices progressed more slowly. Momentum grew following systematic studies of the optoelectronic properties of SC $MAPbI_3$ and SC $MAPbBr_3$ in 2015,[47,48] coupled with the development of facile growth methods like inverse temperature crystallization.[61] Since then, SC perovskites have demonstrated significant advancements in photovoltaics and high-energy radiation detection, highlighting their strong potential for commercialization.[22,62,63]

2.1 Optical properties

One of the most notable distinctions between SC and polycrystalline perovskite films lies in their optical absorption properties. SC perovskites exhibit a redshifted absorption onset compared to their polycrystalline counterparts. As shown in Fig. 2A, the absorption onset in SC $MAPbI_3$ extends to approximately 850 nm, whereas it is restricted to around 800 nm in polycrystalline films.[48] This redshift is attributed to below-bandgap absorption mechanisms induced by Rashba splitting of the conduction band, as illustrated in Fig. 2B.[64] However, the absorption coefficient for this below-bandgap transition is several orders of magnitude lower than that for the primary above-gap transition. Consequently, perovskite films would need to be several hundred micrometers thick to achieve

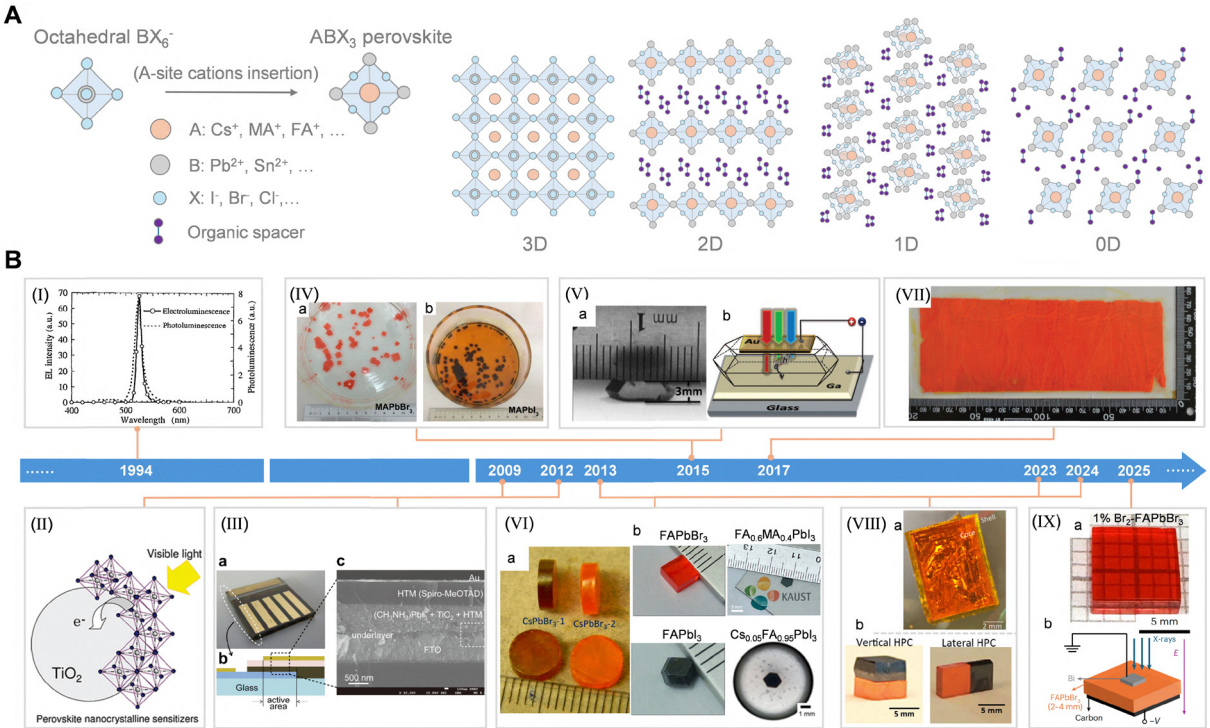

Fig. 1 (A) Schematic representation of the general ABX_3 perovskite lattice and typical structures of 3D, 2D, 1D, 0D ABX_3 perovskites. (B) Milestones timeline of single-crystal (SC) perovskites development, from materials to optoelectronic applications. (I) First application of $(C_6H_5C_2H_4NH_3)PbI_4$ as an electroluminescence emitter. Reproduced with permission from ref. 44, Copyright 1994, AIP Publishing. (II) First introduction of perovskites as light absorbers in dye-sensitized solar cells. Reproduced with permission from ref. 45, Copyright 2009, American Chemical Society. (III) First solid-state perovskite photovoltaic device. Reproduced with permission from ref. 46, Copyright 2012, Springer Nature. (IV) and (V) SC $MAPbI_3$ and $MAPbBr_3$ with superior optoelectronic properties. Reproduced with permission from ref. 47 and 48, Copyright 2015, The American Association for the Advancement of Science. (VI) Evolution of various SC perovskite compositions. Reproduced with permission from ref. 49–52, Copyright 2013, 2016, and 2023, American Chemical Society. (VII) Photograph of a $MAPbBr_3$ crystal film with a thickness of 0.4 mm and an area of 120 cm^2. Reproduced with permission from ref. 53, Copyright 2017, Wiley-VCH Verlag GmbH & Co. KGaA, Weinheim. (VIII) Optical images of the core–shell perovskite heterocrystal and the lateral- and vertical-orientated heterodimensional perovskite crystals. Reproduced with permission from ref. 54, Copyright 2024, American Chemical Society, and ref. 55, Copyright 2023, Wiley-VCH GmbH. (IX) An optical image of the 1% Br_2-treated $FAPbBr_3$ crystal (thickness: 2 mm) and schematic of the detector structure. Reproduced with permission from ref. 56, Copyright 2025, Springer Nature.

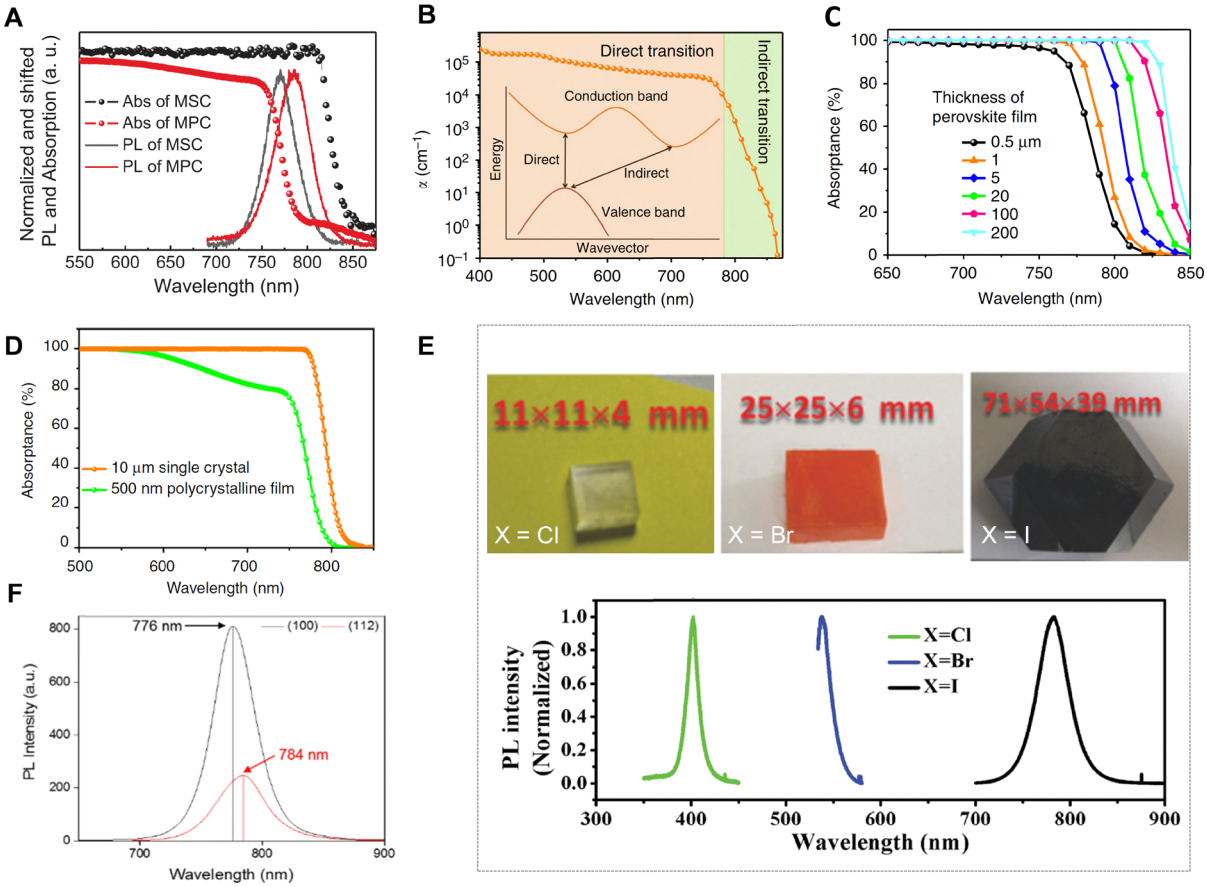

Fig. 2 (A) Normalized PL and absorption spectra of the $MAPbI_3$ single crystals (MSCs) and $MAPbI_3$ polycrystalline (MPC) thin films. Reproduced with permission from ref. 48, Copyright 2015, The American Association for the Advancement of Science. (B) Schematic illustration of direct and below-bandgap transitions, along with the absorption coefficient of a polycrystalline $MAPbI_3$ film. (C) The calculated absorption of $MAPbI_3$ films with different thickness. (D) Absorption spectra of a 10-μm-thick $MAPbI_3$ thin single crystal and a 500-nm-thick polycrystalline film. Reproduced with permission from ref. 67, Copyright 2017, Springer Nature. (E) Photographs of as-grown $CH_3NH_3PbX_3$ (X = Cl, Br, I) single crystals and their corresponding PL spectra. Reproduced with permission from ref. 75, Copyright 2015, Wiley-VCH Verlag GmbH & Co. KGaA, Weinheim. (F) PL spectra of (100) and (112) facets of SC $MAPbI_3$. Reproduced with permission from ref. 72, Copyright 2019, American Chemical Society.

sufficient absorption (Fig. 2C and D), which far exceeds the typical carrier diffusion length in polycrystalline perovskite films. In contrast, SC perovskites inherently offer superior below-bandgap absorption owing to their reduced defect density and the longer optical path lengths afforded by their greater thickness.[65–67] The high quality and minimal in-gap defect states in SC perovskites result in sharp band edge cutoffs without excitonic features or sub-bandgap tails.[47,68] Furthermore, the greater thickness of SC perovskites enables stronger high-energy radiation attenuation, thereby facilitating efficient charge generation throughout the entire active region during high-energy radiation (*e.g.*, X-ray) detection processes. Theoretical calculations indicate that achieving 98% attenuation of 50 keV X-ray photons requires a thickness of approximately 1.0 mm for $MAPbI_3$ and 2.0 mm for $MAPbBr_3$.[22] Such thickness is impractical for state-of-the-art polycrystalline perovskite films due to the limitations imposed by their carrier diffusion lengths,[22,67] whereas SC perovskites can readily fulfill these requirements.

Additionally, SC perovskites exhibit sharper and more intense photoluminescence (PL) peaks, which suggests a reduced density of the trap states typically introduced by grain boundaries. The PL peak positions of SC $MAPbX_3$ (X = Cl, Br, I) (Fig. 2E) appear at 402 nm, 537 nm, and 784 nm, respectively.[69] These peaks are slightly redshifted compared to their polycrystalline counterparts, owing to reduced quantum confinement effects and lower exciton binding energies.[70] Three-dimensional (3D) SC perovskites also possess significant optical anisotropy across different crystal facets and lattice planes.[71] For instance, In SC $MAPbI_3$, the (100) plane exhibits higher PL intensity and superior optoelectronic properties than the (112) plane (Fig. 2F).[72] This optical and electrical anisotropy becomes even more pronounced in low-dimensional SC perovskites (*e.g.*, 2D or 1D structures), due to their enhanced quantum confinement.[73,74]

2.2 Electrical properties

SC perovskites also exhibit superior electrical properties compared to their polycrystalline counterparts. Representative SC perovskites and their corresponding electrical parameters are summarized in Table 1. Key electrical properties include:

(a) Low defect density and high radiation hardness

Table 1 Representative SC perovskites with corresponding electrical parameters

	Mobility ($cm^2 V^{-1} s^{-1}$)	Lifetime (ns)	Resistivity (Ω cm)	Defect density (cm^{-3})	Ion migration energy (eV)	$\mu\tau$ product ($cm^2 V^{-1}$)
$MAPbCl_3$[68,94–96]	179	662	3.7×10^7	7.9×10^9	—	—
$MAPbBr_3$[22,76–78]	130	1.15×10^3	1.25×10^8	2.28×10^9	0.2	1.4×10^{-2}
$MAPbI_3$[97–100]	620	1×10^4	10^8–10^9	1.8×10^9	0.984	1×10^{-2}
$FAPbBr_3$[50,91,101,102]	62	7.2×10^4	3.42×10^9	2.5×10^{10}	0.58	2.1×10^{-4}
$FAPbI_3$[102,103]	150	4.3×10^3	5.5×10^7	1.3×10^{10}	0.49	1.4×10^{-2}
$CsPbI_3$[104,105]	44.3	1.19×10^5	7.4×10^9	—	0.58	3.63×10^{-3}
$CsPbBr_3$[105–109]	181 (e), 56.5 (h)	2.96×10^5	8.5×10^9	1.5×10^{10}	0.42	1.32×10^{-2}
$CsPbCl_3$[110]	28 (e), 20 (h)	438	1.7×10^9	—	—	0.3×10^{-3}
$Cs_2AgBiBr_6$[111–113]	7.02	700	1.6×10^{11}	1.74×10^9	0.33	6.3×10^{-3}
$(NH_4)_3Bi_2I_9$[74]	213	—	—	4.48×10^9	0.91	1.1×10^{-2}
$Cs_3Bi_2I_9$[114,115]	4.3 (e), 1.7 (h)	16.7	—	2.78×10^9	—	2.18×10^{-3}
$FA_3Bi_2I_9$[116]	4	3×10^4	7.8×10^{10}	9.48×10^9	0.56	1.3×10^{-4}
$MA_3Bi_2I_9$[117–120]	70	3.12	2.28×10^{11}	1.2×10^{10}	1.18	4.6×10^{-5}
DABCO-NH_4Br_3[121,122]	2.08	6×10^4	2.36×10^8	2.6×10^{10}	0.25	1.2×10^{-3}

Note: (DABCO, *N*-*N*′-diazabicyclo[2.2.2]octonium).

SC perovskites exhibit significantly fewer grain boundaries, with defect densities ranging from 10^9 to 10^{10} cm^{-3},[22,76–78] which is several orders of magnitude lower than that of polycrystalline perovskites (10^{14}–10^{17} cm^{-3}).[79,80] Moreover, the defect states in SC perovskites typically lie at shallow energy levels, a property that allows them to benign or easily passivated. This intrinsically lower defect density prolongs carrier lifetimes, enhances charge collection, mitigates degradation pathways, which in turn improves photon-to-electron conversion efficiency and environmental stability.[81,82] Additionally, the reduced trap density contributes to a higher open-circuit voltage in solar cells.[83]

Another remarkable feature of SC perovskites is their exceptional defect tolerance, which contributes to their long carrier diffusion lengths and high radiation hardness.[48,84,85]

(b) Long carrier lifetime

SC perovskites typically exhibit longer carrier lifetimes, primarily because their low defect density reduces non-radiative recombination. The low ion migration rate in SC perovskites also contributed to their extended carrier lifetimes. In photovoltaic devices, prolonged carrier lifetimes improve the collection efficiency of photogenerated charges and enhance conversion efficiency, while in high-energy radiation detectors, they extended carrier drift distances, improving signal-to-noise ratios (SNR) and sensitivity.[70]

(c) High carrier mobility

Carrier mobility (μ) is a key parameter that quantifies the ability of electrons or holes to move within a material under an electric field. The carrier mobility of perovskites is a complex parameter influenced by temperature, crystal structure, carrier concentration, and doping level. In general, SC perovskites exhibit higher mobility due to their low defect density, ordered crystal structure, and long carrier lifetime,[86] enabling efficient charge transport in both solar cells and radiation detectors.

(d) Low ion migration

SC perovskites exhibit lower ion migration than the polycrystalline perovskites, which is essential for enhancing the long-term stability of devices. The suppression of ion migration is primarily attributed to their lower defect density, which limits the available pathways for ion movement,[87] as well as to the strong ionic bonding (*e.g.*, Pb–I bonds) that imposes higher energy barriers for ion displacement.[87,88]

(e) High $\mu\tau$ product

The $\mu\tau$ product quantifies the ability of photogenerated carriers to transport within a semiconductor material and serves as a key factor in optoelectronic performance. The $\mu\tau$ product represents the carrier drift distance before recombination, with larger values indicating more efficient charge transport to the electrodes and reduced charge loss. The combination of high carrier mobility, low defect density, and a well-ordered crystal structure in SC perovskites enables efficient charge transport. Moreover, high-quality crystal growth further contributes to enhanced $\mu\tau$ values. An increased $\mu\tau$ product reduces recombination losses before charge collection, improving photoelectric conversion efficiency.[89] Additionally, higher $\mu\tau$ values indicates reduced carrier recombination caused by electric field inhomogeneity, leading to improved stability and making SC perovskites ideal for high-performance X-ray detectors.[76,90–92]

2.3 Superior stability

SC perovskites exhibit superior intrinsic stability compared to polycrystalline counterparts due to their few grain boundaries and reduced defect accumulation. In general, defects in perovskites can be categorized into 0D point defects, 1D line defects, 2D planar defects, and 3D volumetric defects (Fig. 3A and B).[93]

Among these, 0D point defects—including vacancies, interstitials, and anti-site defects—are the most critical factors impacting optoelectronic device performance.[123] The high defect density in perovskites results from the interplay of intrinsic and extrinsic factors. The soft ionic lattice and low formation energy of perovskites naturally make them prone to defect formation, as the structural flexibility of perovskite allows for lattice distortions.[124,125] Furthermore, rapid crystallization and non-uniform nucleation during the annealing process can induce heterogeneous crystal growth, leading to the generation of 0D point defects.[6,43,126] These combined

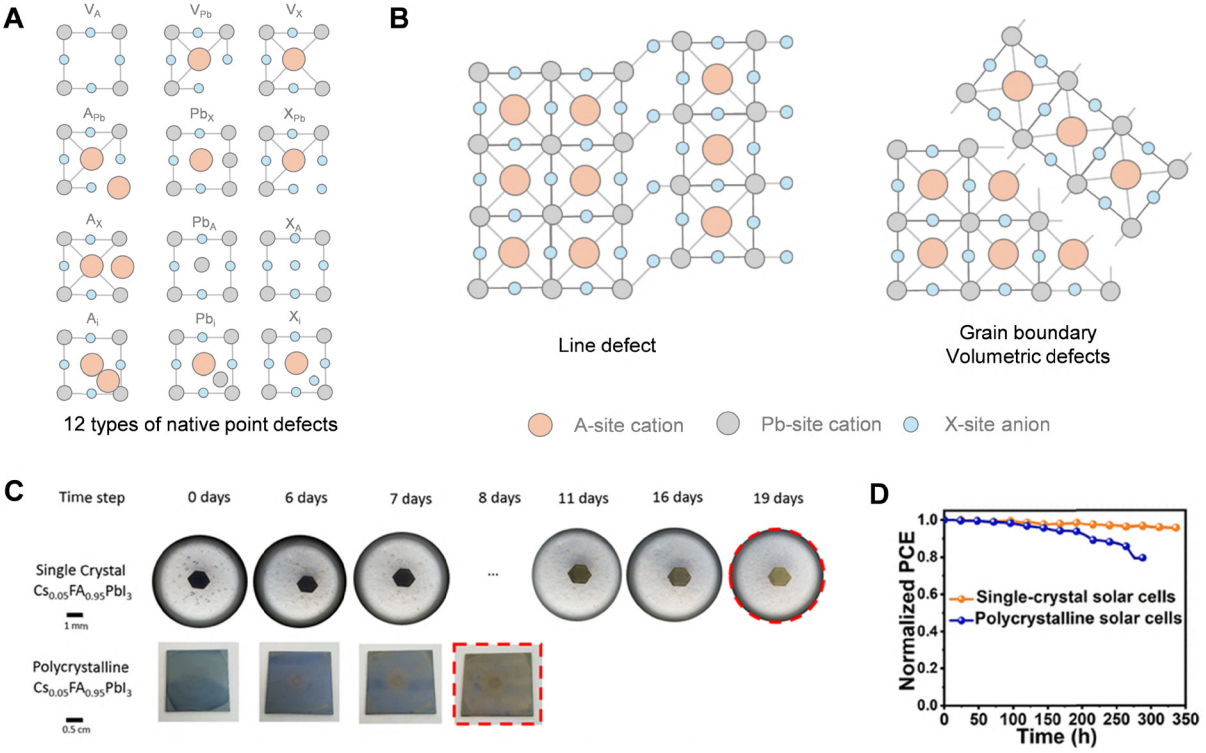

Fig. 3 (A) Schematic representation of 12 types of native point defects in the $APbX_3$-type perovskite. (B) Schematic diagram of line and volumetric defects. (C) Optical images for the phase transition of SC $Cs_{0.05}FA_{0.95}PbI_3$ and polycrystalline $Cs_{0.05}FA_{0.95}PbI_3$ film under damp-heat conditions (85 °C/65% relative humidity). Reproduced with permission from ref. 52, Copyright 2023, American Chemical Society. (D) Operational stability of 200 μm $FA_{0.55}MA_{0.45}PbI_3$ SC PSCs and 500 nm polycrystalline thin-film PSCs. Reproduced with permission from ref. 145, Copyright 2022, American Chemical Society.

factors contribute to the overall defect density, which in turn influence the optoelectronic properties and performance of perovskite-based devices.

Defects in perovskites have a profound impact on the stability of optoelectronic devices.[33,127–129] Vacancy defects, for example, facilitate additional ion migration pathways. This promotes the migration of ions like I^-, MA^+, and Pb^{2+} under an external electric field, which in turn contributes to the degradation of perovskite, particularly at the perovskite/charge transport layer interface. It can also be accelerated under other external stressors (*e.g.* light, humidity, and heat).[130–133] Defects, particularly those located at grain boundaries or surfaces of perovskite, serve as entry points for moisture and oxygen, thereby accelerating degradation.[134–136] For instance, moisture can hydrolyze organic cations (*e.g.*, MA^+ or FA^+), causing the decomposition of the perovskite structure into PbI_2 octahedra and other byproducts, thereby affecting the stability and performance of perovskite-based devices.[137–140] Furthermore, defects in perovskites can accelerate photo-induced degradation mechanisms, including the generation of Pb^0 clusters under light exposure and halide vacancy migration, which lead to a phase segregation.[141,142] These defects also reduce the thermal stability of perovskites, promoting phase transitions or decomposition under thermal stress.[139,143] Additionally, defects facilitate the reaction between oxygen and iodine vacancies, generating deep trap states that further degrade device performance.[36,144]

The superior stability of SC perovskites is not merely theoretical; owing to their lower defect density, it has also been proven by numerous experimental results. As shown in Fig. 3C, SC $Cs_{0.05}FA_{0.95}PbI_3$ perovskite maintains a stable black α-phase after two weeks under 85 °C and 65% relative humidity conditions, exhibiting superior stability under damp-heat conditions, while its polycrystalline counterpart transforms into the yellow δ-phase within one week.[52] Moreover, a comparison of the storage stability of SC and polycrystalline $MA_{0.75}FA_{0.25}PbI_3$-based (PSCs) shows that the efficiency of unencapsulated polycrystalline device rapidly dropped to 50% of its initial value after being transferred from a nitrogen atmosphere to ambient conditions (~50% relative humidity), whereas the SC device retained over 95% of its initial efficiency after 4 days.[146] In addition, it is observed that SC and polycrystalline $FA_{0.55}MA_{0.45}PbI_3$-based PSCs (Fig. 3D) exhibit different operational stability under maximum power point tracking, with the SC device showing no degradation after 330 hours of operation, while the polycrystalline device has a 20% efficiency loss after 300 hours.[145]

In summary, intrinsic defects are the primary cause of poor stability in perovskite-based optoelectronic devices. By minimizing these defects, SC perovskites exhibit superior stability and thus hold greater potential than their polycrystalline counterparts.

3. Growth methods of SC perovskites

SC perovskites have been widely investigated for various optoelectronic devices, demonstrating significant potential for

advancing perovskite technologies. The synthesis of high-quality SC perovskites is fundamental to achieving superior optoelectronic performance. Given the diversity in SC perovskite compositions and application scenarios, numerous SC perovskite growth methodologies have been developed. This section presents a comprehensive analysis of SC perovskite growth techniques, focusing on two key aspects: bulk crystal growth and SC thin-film fabrication. Defect density and size statistics of SC perovskite bulk or films prepared by different methods are summarized in the Table S1 (SI).

3.1 Bulk SC perovskites growth

The thickness of bulk SC perovskites plays a pivotal role in device performance, particularly for photodetectors, where thicker crystals enhance photon absorption. It is especially important for vertical-type perovskite detectors used in high-energy detection, as thicker films enable more efficient capture of high-energy photons. Moreover, bulk SC perovskites serve as a valuable platform for investigating the intrinsic properties of these materials—such as their mechanical resilience, electronic behavior, and ferroelectric characteristics—thereby supporting both device optimization and fundamental research.

Bulk SC perovskites can be grown using two primary methods: solution-based and solid-state techniques. Solution-based methods, such as inverse temperature crystallization, solution temperature-lowering, and antisolvent vapor-diffusion crystallization, are favored for their flexibility and ease of use. Solid-state techniques, such as the Bridgman method, are also employed to produce larger, high-quality crystals. Although challenges such as carrier recombination can arise in larger crystals, high-quality bulk SC perovskites remain crucial for advancing both research and material applications.

3.1.1 Bridgman method. The Bridgman technique is a widely adopted approach for growing high-quality single crystals through controlled directional solidification. In this method, precursor materials and seed crystals are sealed within a quartz ampoule under vacuum or an inert atmosphere (Fig. 4A).[152,153] The ampoule is then gradually translated from a high-temperature region—where the material fully melts—toward a cooler zone, ensuring a controlled solidification process. As the temperature decreases, nucleation begins at the tip of the ampoule, followed by the gradual formation of a well-ordered crystalline structure.[152,153] This method has been pivotal in advancing metal halide single-crystal research, yielding high-purity compounds with exceptional optoelectronic properties. Crystals such as $CsPbBr_3$, $CsPbCl_3$, and $TlPbI_3$, grown *via* Bridgman processing, have demonstrated outstanding X-ray detection capabilities.[152,154,155] However, despite its advantages, the Bridgman method has inherent challenges. The slow cooling process leads to extended growth times, making large-scale production less efficient. Furthermore, maintaining a stable temperature gradient is technically demanding due to thermal convection and heat dissipation effects, which can impact crystal uniformity. The technique is also unsuitable for materials with high thermal expansion coefficients or volatile organic components, limiting its use to all-inorganic perovskites such as $CsPbBr_3$ and $CsSnI_3$.[49,156] Future improvements in process control and alternative growth strategies could enhance the efficiency and scalability of this technique, broadening its applications in next-generation optoelectronic and sensing technologies.

3.1.2 Inverse temperature crystallization method. The inverse temperature crystallization (ITC) method exploits the unusual retrograde solubility of certain metal-halide perovskites in specific organic solvents, where solubility decreases as temperature rises. This counterintuitive behavior, first reported by Bakr *et al.*, enabled the development of ITC as a technique for growing high-quality SC perovskites (Fig. 4B).[61] By leveraging this solubility trend, ITC allows for controlled nucleation and crystal growth, making it a widely adopted approach in optoelectronic applications. The choice of solvent is crucial, as it directly influences crystallization efficiency and crystal quality. For instance, $MAPbBr_3$ exhibits retrograde solubility in dimethylformamide (DMF), $MAPbCl_3$ in dimethyl sulfoxide (DMSO), and $MAPbI_3$ in γ-butyrolactone (GBL), facilitating the formation of large single crystals rather than multiple smaller ones.[61,96,157] ITC offers a scalable approach for halide perovskite crystallization, enabling rapid crystallization, simple processing. However, challenges like mass-transport limitations, uncontrolled nucleation, and thermal management remain. Ongoing research is needed to refine nucleation control, optimize precursor compositions, and develop scalable methods for industrial applications. Despite these challenges, ITC-based techniques show promise for enabling next-generation optoelectronic devices, including solar cells, photodetectors, and LEDs.

3.1.3 Antisolvent vapor-assisted method. Antisolvent vapor-assisted crystallization (AVC) is an advanced technique for growing high-quality bulk SC perovskites formation by precisely controlling the crystallization kinetics through solvent diffusion. The method exploits the differential solubility of perovskite precursors in two miscible solvents: a primary solvent in which the perovskite precursors dissolve and an antisolvent that reduces solubility upon diffusion, triggering controlled nucleation and growth (Fig. 4C). This process enables the formation of high-purity, defect-minimized perovskite crystal with enhanced optoelectronic properties.[47] While AVC offers a scalable and highly controlled route for bulk SC perovskite growth, certain limitations persist. The technique remains substrate- and material-specific, with challenges in extending its applicability to diverse halide perovskite compositions. Moreover, precise control over diffusion kinetics and solvent compatibility is crucial for reproducibility and consistency. Even so, it holds great promise for advancing perovskite optoelectronics, particularly in photovoltaics, photodetectors, and X-ray imaging.

3.1.4 Solution temperature-lowering method. The solution temperature-lowering (STL) technique exploits the temperature-dependent solubility of perovskite precursors in hydrohalic acid solutions to enable controlled crystallization. By gradually lowering the temperature, precursor solubility decreases, prompting nucleation and directional crystal growth.[149] This process involves three key stages: (I) dissolving precursors at an elevated temperature, (II) initiating seed crystal formation through

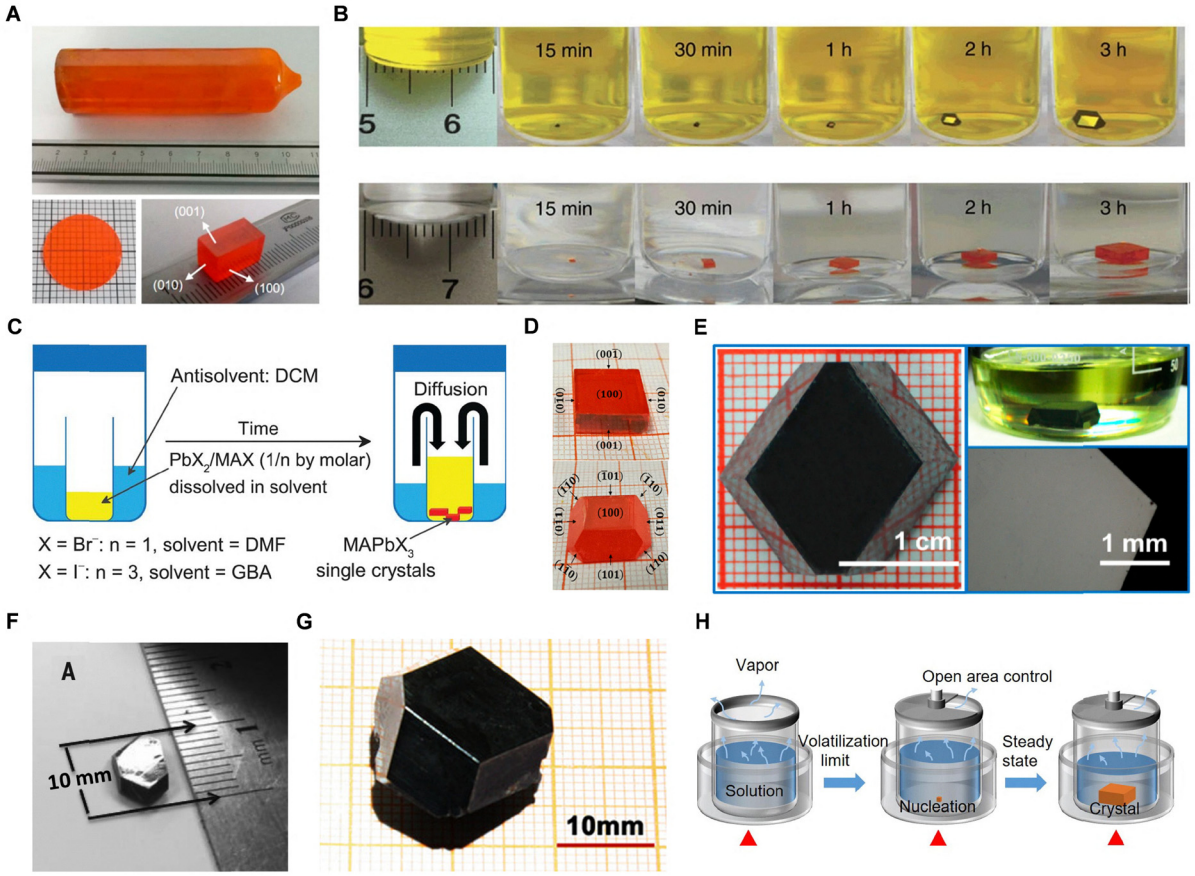

Fig. 4 (A) Photographs of an as-grown SC $CsPbBr_3$ (top), a polished wafer (bottom left), and an oriented cuboid SC $CsPbBr_3$ (bottom right) grown *via* the Bridgman method. Reproduced with permission from ref. 147, Copyright 2018, American Chemical Society. (B) Time-sequenced images of $MAPbI_3$ and $MAPbBr_3$ crystal growth synthesized using the inverse temperature crystallization (ITC) method. Reproduced with permission from ref. 61, Copyright 2015, Springer Nature. (C) Schematic representation of the crystallization process in the antisolvent vapor-assisted method. Reproduced with permission from ref. 47, Copyright 2015, The American Association for the Advancement of Science. (D) Photograph of as-grown cubic and polyhedral $MAPbBr_3$ crystals synthesized using a mixed antisolvent system (DCM/DMF = 1 : 2), and facets identified *via* SC X-ray diffraction (XRD). Reproduced with permission from ref. 148, Copyright 2018, American Chemical Society. (E) Photograph of a seed-induced $MAPbI_3$ (Cl) bulk single crystal (20 mm × 18 mm × 6 mm) grown using the solution temperature-lowering (STL) method (left), alongside an image of an $MAPbI_3$ (Cl) bulk single crystal incubated in solution at room temperature (top right) and a microscopic image of its (100) facet (bottom right). Reproduced with permission from ref. 149, Copyright 2016, American Chemical Society. (F) Photograph of the SC $MAPbI_3$ obtained *via* bottom-seeded solution growth (BSSG). Reproduced with permission from ref. 48, Copyright 2015, The American Association for the Advancement of Science. (G) Photograph of the SC $MAPbI_3$ obtained *via* top-seeded solution growth (TSSG). Reproduced with permission from ref. 150, Copyright 2016, Wiley-VCH Verlag GmbH & Co. KGaA, Weinheim. (H) Schematic illustration of the solvent volatilization-limited growth (SVG) strategy for halide perovskites, where a perovskite precursor solution is uniformly heated in an oil bath, and solvent volatilization is controlled using a fine-control valve on top of a sealed beaker. Reproduced with permission from ref. 151, Copyright 2021, Elsevier Inc.

cooling, and (III) further reducing the temperature to drive SC growth. The STL method offers notable advantages, including precise growth rate control, the ability to produce high-quality large-area single crystals, and broad applicability across various perovskite families (Fig. 4E). Unlike inverse temperature crystallization, STL is particularly useful for 2D and inorganic perovskite systems.[158] Furthermore, the method can be refined through techniques like bottom-seeded solution growth (BSSG) and top-seeded solution growth (TSSG), where the positioning of the seed crystals promotes controlled crystallization and enhances the quality of the resulting crystals. In the TSSG method, a seed crystal is positioned at the top of the solution, with the solution's temperature gradient inducing material growth from the bottom of the solution (Fig. 4F). This method benefits from continuous material supply facilitated by convection between regions of higher and lower temperature, leading to faster crystal growth. In contrast, the BSSG method positions the seed crystal at the bottom of the solution, typically suspended within a saturated precursor solution. The temperature is gradually reduced from a high initial temperature to room temperature, allowing crystal growth from the bottom upwards. A key advantage of this method is its ability to yield larger single crystals, particularly when precise temperature control and high-quality seed crystals are used. BSSG has also been applied to the growth of other perovskites, including Pb-free variants such as $NH(CH_3)_3SnBr_3$ and $NH(CH_3)_3SnCl_3$, expanding its utility beyond conventional lead-based perovskites.[159]

Both TSSG and BSSG are effective techniques for growing high-quality perovskite single crystals through controlled temperature reduction. However, both methods require careful optimization of cooling rates, precursor selection, and seed quality for reproducible results. Despite their advantages, these methods face limitations. The slow cooling process can be time-consuming, and they may not be suitable for materials with low solubility at high temperatures. Furthermore, the reliance on hydrohalic acids for precursor solubility may lead to stability issues. Alternative solvents, such as deionized water, have shown potential to stabilize all-inorganic perovskite growth. To fully realize the potential of these techniques, further research is required to address these challenges and enhance scalability for practical applications.

3.1.5 Slow evaporation method. Slow evaporation is a widely used method for SC growth, where solvent evaporation increases solute concentration, driving nucleation. It is crucial for hybrid perovskites and organic–inorganic frameworks, with solvent composition and temperature shaping crystallization kinetics. Despite its simplicity and broad material compatibility, slow evaporation is hindered by long processing times and sensitivity to environmental fluctuations, limiting its scalability.

3.1.6 Solvent volatilization limited growth (SVG) method. The solvent volatilization limited growth (SVG) method has emerged as an effective technique for growing high-quality halide perovskite single crystals. By regulating solvent evaporation through a fine-control valve, SVG stabilizes the crystal growth process, ensuring a constant growth rate and improved crystal quality. Unlike traditional temperature-induced growth methods, SVG overcomes issues of rapid solute integration and varying growth rates, which can result in suboptimal crystals (Fig. 4H).

3.1.7 Flux-regulated crystallization method. The flux-regulated crystallization method uses a feedback loop to directly monitor and control the linear growth rate of SC perovskite, overcoming the complexity associated with multiple growth parameters in solution-grown single crystals. This approach enables a stable and precise growth rate, producing centimeter-scale SC perovskites with exceptional crystallinity and presenting a reliable platform for scalable production of high-quality crystals.[160]

3.2 Fabrication methods of SC perovskite thin films

Bulk SC perovskites, known for their exceptional photoelectronic properties, have been widely used in high-energy radiation detection. However, the millimeter-scale thickness of bulk SC perovskites is incompatible with the micrometer-scale vertical architecture required for photovoltaics and other scenarios. Therefore, the development of high-quality, micrometer-scale SC perovskite thin films with vertical orientation is essential to meet the fabrication requirements of various photoelectronic devices. In addition, achieving high-quality SC perovskite films with controlled morphology and composition remains a considerable challenge. In this section, we explore the various strategies developed to produce SC perovskite films, addressing key advancements and remaining obstacles in the field.

3.2.1 Slicing. Slicing large, bulk perovskite crystals into thin wafers is a key top-down method for fabricating perovskite-based optoelectronic devices. Diamond-wire sawing has proven effective, producing SC wafers of $FAPbI_3$ and $MAPbI_3$ with dimensions greater than 20 mm and thicknesses as thin as 100 μm (Fig. 5A).[161] To further reduce the thickness, wet etching techniques, such as the use of γ-butyrolactone, can achieve thicknesses of approximately 15 μm.[162] However, the mechanical slicing of these brittle crystals often results in fractures, leading to charge trap formation that impairs both the electrical and mechanical properties of the resulting thin films. Additionally, the solubility differences between the organic and inorganic components during etching can increase surface trap density, further degrading the film quality. Despite these advances, the top-down slicing method faces limitations, primarily due to the complexity of the process and the lack of specialized equipment. Ongoing improvements in mechanical polishing, etching, and cooling techniques are needed to reduce material loss, minimize surface defects, and enable scalable production of perovskite wafers for integrated semiconductor applications.

3.2.2 Roll-to-roll. The roll-printing or roll-to-roll (R2R) technique has emerged as a promising method for fabricating large-area, continuous SC perovskite thin films, overcoming the limitations of traditional spatially confined solution processes that yield smaller, discrete crystals. This technique has been successfully applied to produce inch-scale SC $MAPbI_3$ thin films (Fig. 5B).[163] The process uses a specially designed channel-patterned rolling mold to transfer a perovskite ink solution onto a preheated substrate. The solvent evaporates almost instantly, triggering perovskite crystallization. The mold's geometric confinement limits crystal growth in the thickness direction to a submicrometer scale. By controlling the temperature, the process favors the growth of existing seed crystals rather than forming new ones, resulting in uniform SC films rather than random polycrystalline structures. However, challenges remain in ensuring uniform film quality, controlling the crystallization process, and achieving long-term stability. Addressing these challenges is essential for advancing R2R technology in perovskite photovoltaics and improving its commercial viability.

3.2.3 Space-confined growth method. The space-confined growth method has become a widely recognized approach for producing high-quality SC thin films, particularly for conventional perovskite materials such as $MAPbBr_3$, $MAPbI_3$, and $FAPbI_3$. The method relies on a geometrically confined space between two substrates, which directs lateral crystal growth, reducing film defects and enabling precise control over thickness. The process begins by introducing a perovskite precursor solution between the substrates. Capillary forces drive the solution's movement, while a temperature gradient induces convection, facilitating controlled deposition (Fig. 5C and D). The confined environment influences crystallization dynamics, leading to the formation of high-quality thin films with uniform properties. Central to the technique is the precise control over the gap between the substrates. This gap can be adjusted to regulate film thickness with remarkable accuracy, typically on the order of a few micrometers. Moreover, the space-confined

method integrates seamlessly with traditional perovskite crystal growth techniques, such as ITC, AVC, and cooling-induced crystallization. Combining these established methods with the geometric confinement of the space allows the transition from bulk SC perovskites to thin films without compromising material quality. It makes the space-confined method an attractive approach for large-scale industrial fabrication of perovskite-based devices.[164] With ongoing advancements in surface

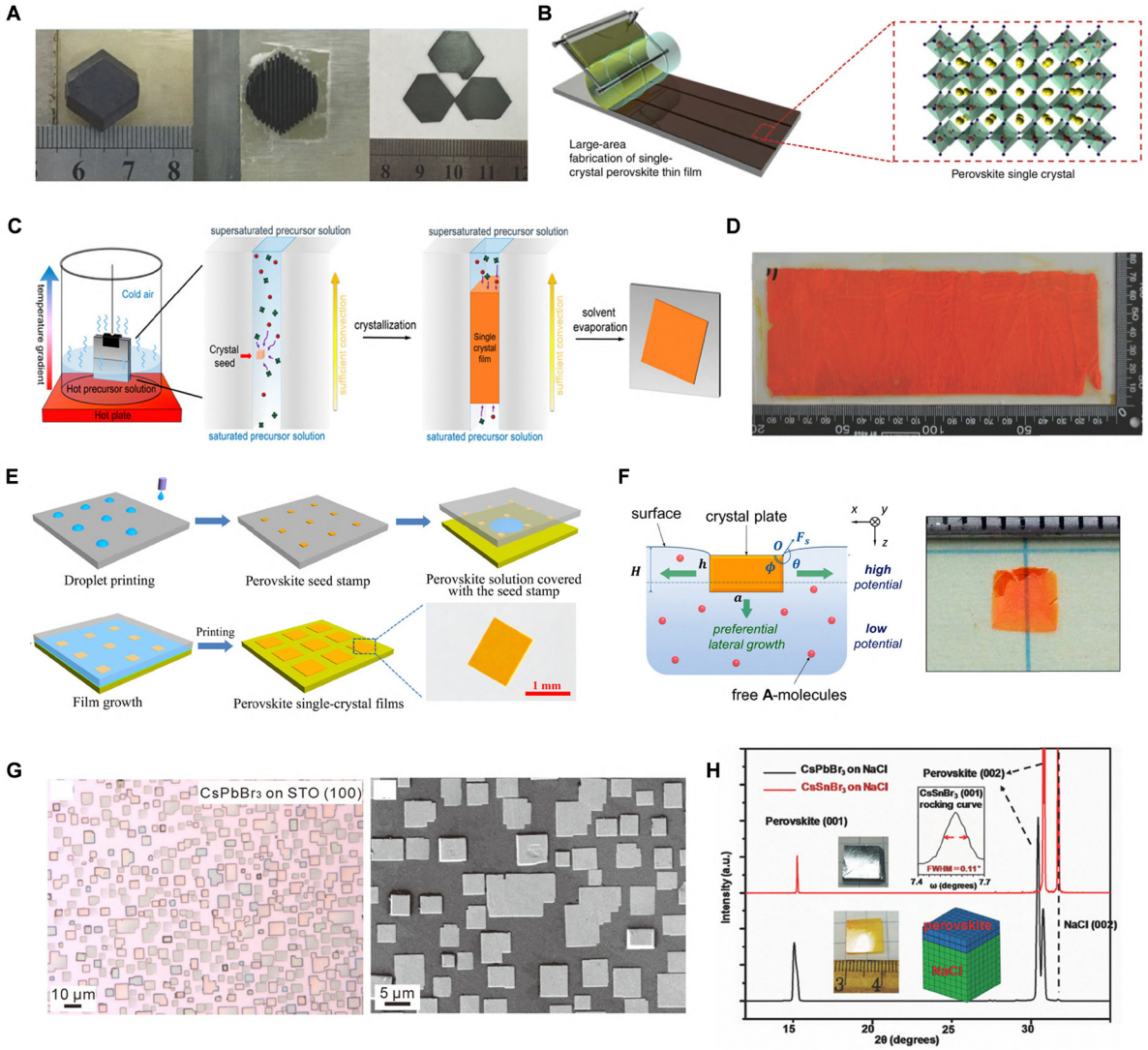

Fig. 5 (A) Photograph of a $FAPbI_3$ single crystal, along with SC $FAPbI_3$ wafers sliced along natural parallelogram-shaped crystallographic facets. Cross-sectional and panoramic views of the wafers obtained *via* the slicing method are shown. Reproduced with permission from ref. 161, Copyright 2016, Wiley-VCH Verlag GmbH & Co. KGaA, Weinheim. (B) Schematic of SC perovskite thin film fabrication *via* geometrically confined lateral crystal growth using a rolling mold. The perovskite ink is confined between the mold and substrate, directing crystal growth in one direction. As the mold rolls and ink is continuously supplied, large-area patterned SC films form along the rolling direction. Reproduced with permission from ref. 163, Copyright 2017, Springer Nature. (C) Schematic of perovskite SC thin film growth using the space-confined growth method. Reproduced with permission from ref. 170, Copyright 2016, American Chemical Society. (D) Photograph of $CH_3NH_3PbBr_3$ crystal films with a thickness of 0.4 mm and an area of $\sim$120 cm^2 synthesized *via* the same method. Reproduced with permission from ref. 53, Copyright 2017, Wiley-VCH Verlag GmbH & Co. KGaA, Weinheim. (E) Schematic of the scalable growth of perovskite SC films using a stamping method. The process involves fabricating a perovskite seed stamp *via* inkjet printing, followed by transferring it onto a target substrate with perovskite solution, where *in situ* crystal growth occurs as the solvent evaporates. Reproduced with permission from ref. 165, Copyright 2018, The American Association for the Advancement of Science. (F) Schematic of crystal growth *via* inverse temperature crystallization (ITC). Free precursor molecules predominantly attach to the nucleus sides due to higher free energy gain, leading to lateral crystal plate growth. Surface tension supports the floating crystal, forming a free-standing $MAPbBr_3$ crystal, as shown in the accompanying photograph. Reproduced with permission from ref. 166, Copyright 2017, American Chemical Society. (G) Optical microscopy and SEM images of $CsPbBr_3$ nanoplates grown on $SrTiO_3$ *via* vapor-phase epitaxy. Reproduced with permission from ref. 171, Copyright 2017, American Chemical Society. (H) Structural and morphological characterization of halide perovskite growth *via* high-temperature vapor-phase epitaxy on NaCl. (i) $\theta - 2\theta$ XRD patterns of $CsSnBr_3$/NaCl (red) and $CsPbBr_3$/NaCl (black), showing only (100) and higher-order peaks parallel to NaCl (002). Reproduced with permission from ref. 169, Copyright 2017, Wiley-VCH Verlag GmbH & Co. KGaA, Weinheim.

modification and substrate engineering, the space-confined method is expected to further enhance the quality and scalability of SC perovskite thin films.

3.2.4 Stamping method. The stamping method integrates seeded growth with space confinement, offering a scalable approach for fabricating SC perovskite thin films. This technique relies on printing an ordered array of perovskite seeds onto a temporary substrate, followed by a space-confined solvent evaporation-induced crystallization process.[165]

A key advantage of this approach is the ability to achieve precise control over film thickness, which depends on the size of the initial seed crystals. The thickness can be tuned from hundreds of nanometers to over 10 μm, making the method adaptable for various applications. Furthermore, the nucleation density can be optimized by adjusting the printing parameters, ensuring high-quality films with smooth morphology. This method has been successfully demonstrated for multiple perovskite compositions, including $MAPbBr_3$, $MAPbCl_3$, $MAPbI_3$, $CsPbBr_3$, and BA_2PbBr_4.[165] By combining precise spatial control with scalable processing, the stamping method provides a robust pathway for the industrial-scale fabrication of high-performance perovskite-based devices.

3.2.5 Surface-tension method. The surface tension-assisted inverse temperature crystallization (ITC) method has emerged as a promising strategy for achieving lateral growth at the solution–air interface. This approach exploits the increased intermolecular spacing in the surface layer, which reduces interaction energies and lowers the nucleation barrier, thereby promoting preferential in-plane growth over vertical crystallization.[157,166]

Bakr *et al.* demonstrated that solvents with high surface tension, such as DMSO, enhance nucleation at the solution surface, enabling the formation of high-quality SC $MAPbBr_3$, $MAPbI_3$, and $MASnBr_3$ thin films with areas up to 1 cm^2 and thicknesses ranging from 5 to 20 μm.[166] Wang *et al.* further expanded this strategy by synthesizing quasi-two-dimensional perovskite SCTFs, where alkyl ammonium cations induced ordered molecular alignment at the interface. This facilitated rapid lateral growth, resulting in photodetectors with high switching ratios, low dark currents, and fast response times.[167] Despite the benefits of this method, an increase in surface trap densities was observed due to the large solution-film contact area, which slightly impacted the optoelectronic properties. However, this technique holds significant potential for 2D hybrid perovskites, which have demonstrated superior photodetector performance compared to their 3D counterparts.[168]

3.2.6 Vapor-phase epitaxial growth. Vapor-phase epitaxy (VPE) has emerged as a highly effective method for the growth of high-quality SC perovskite thin films. This technique, however, requires that the lattice constant and thermal expansion coefficient of the halide perovskite match those of the substrate due to the high temperatures involved, which narrows the range of viable substrates and perovskite materials. Monocrystalline alkali halides, such as $CsPbBr_3$ and $CsSnBr_3$, are commonly used as substrates for the epitaxial growth of inorganic perovskite thin films due to their similar lattice constants and chemical compositions (Fig. 5H).[169] The VPE holds potential for producing high-quality perovskite thin films, yet further developments are required to enhance film quality and larger-scale integration.

3.2.7 Engineered epitaxial growth strategies. Solution-based epitaxy offers a unique approach for achieving uniform and controlled epitaxial growth by forming stable interfacial chemical bonds. This method provides a significant advantage over vapor-phase epitaxy, as it allows for much broader growth coverage, thanks to the consistent and uniform contact between the substrate and the precursor. Bulk SC perovskites can be utilized as substrates in this process, with their composition being tailored to enable different epitaxial techniques. These include homoepitaxy,[172,173] heteroepitaxy,[174] as well as specialized methods like remote epitaxy,[175] van der Waals epitaxy,[175] and pinhole epitaxy,[176] each offering unique ways to refine the properties of SC perovskite thin films.

(a) Homoepitaxy and lift-off

The initial chemical epitaxial growth of SC $CH_3NH_3PbBr_3$ was reported by combining advanced microfabrication, homoepitaxy, and low-temperature solution methods. This approach enabled precise control over the crystal's thickness, morphology (such as thin films, rods, and cubes), orientation (*e.g.*, ⟨001⟩, ⟨110⟩, and ⟨111⟩), and composition, including the alloying of different cations and anions as shown in (Fig. 6A).

The resulting SC structures, when integrated into a light-emitting diode (LED) array, demonstrated significantly enhanced quantum efficiencies compared to their polycrystalline counterparts. These findings underscore the potential of SC perovskites for optoelectronic applications, highlighting their promising use in advanced devices.[173] Building on this, a similar solution-based lithography-assisted epitaxial-growth-and-transfer method has been developed to fabricate a continuous SC thin films of halide perovskites with high precision in terms of thickness (ranging from 600 nm to 100 μm), area (with continuous films up to 5.5 cm × 5.5 cm), and composition gradient (for example, transitioning from methylammonium lead iodide, $MAPbI_3$, to a lead-tin alloy $MAPb_{0.5}Sn_{0.5}I_3$). This technique uses a general halide perovskite bulk crystal as the substrate, which is sealed with a parylene-C polymer layer to prevent decomposition from etchants and developers (Fig. 6B). The transferred films exhibited mechanical flexibility and demonstrated excellent electronic properties, including enhanced carrier mobility due to the gradient bandgap formed by the lead-tin alloying. Devices based on these SC perovskite films, such as solar cells, achieved impressive efficiencies of up to 18.77%, along with superior stability against degradation, further emphasizing the potential of this approach in fabricating high-performance perovskite-based devices.[172]

(b) Hetero epitaxy

Heteroepitaxial growth enables precise control over film thickness, preferential growth sites, and crystal orientations, while offering compatibility with existing fabrication infrastructures and scalability for large-area device applications. Chen *et al.* reported the strained epitaxial growth of α-formamidinium lead iodide (α-$FAPbI_3$) on lattice-mismatched perovskite substrates, achieving compressive strain of up to 2.4% (Fig. 6C). This strain modifies the crystal structure, reduces the bandgap, and enhances

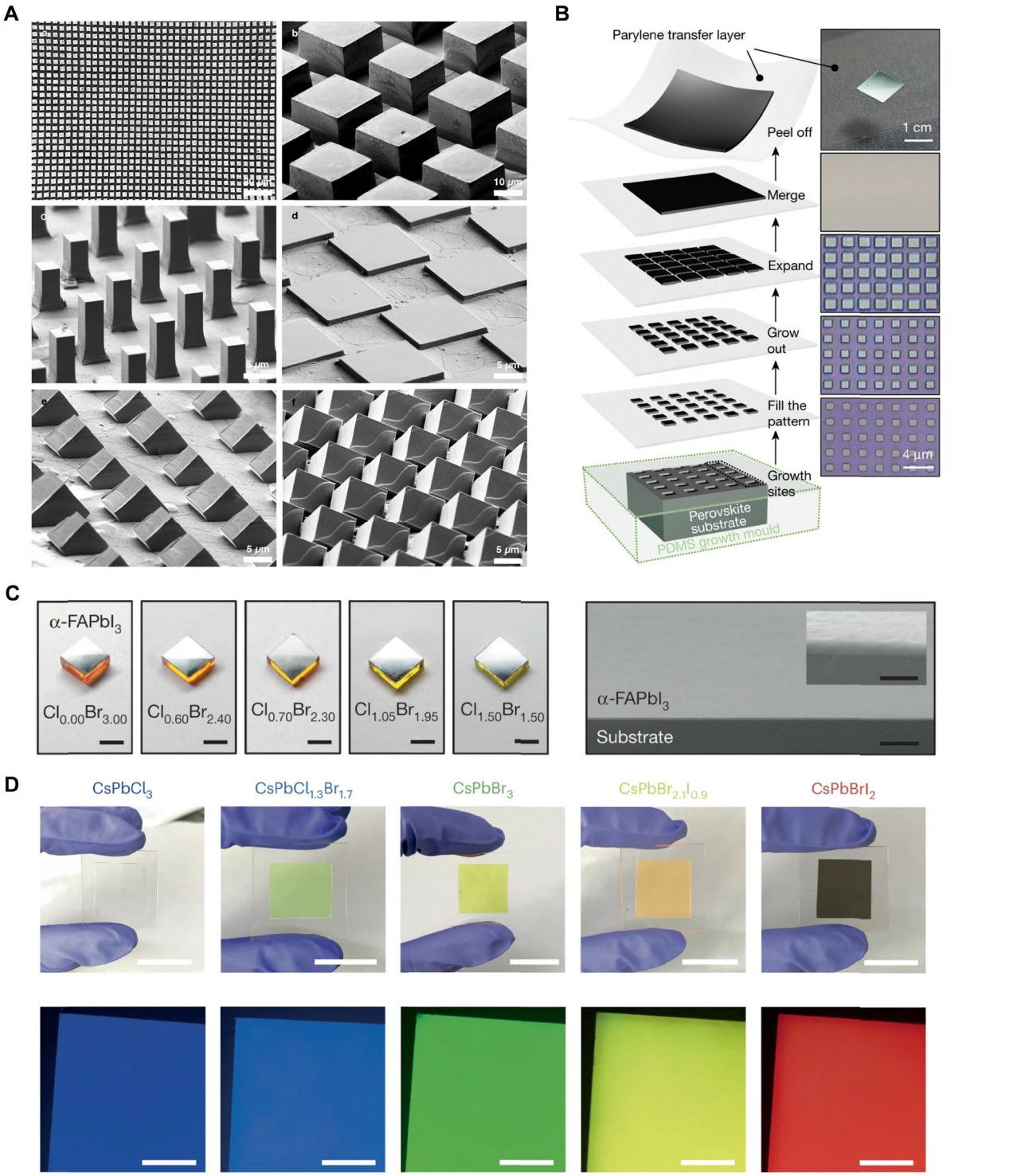

Fig. 6 (A) Scanning electron microscopy (SEM) images illustrating the controlled homoepitaxial growth of SC $MAPbBr_3$. Reproduced with permission from ref. 173, Copyright 2018, Wiley-VCH Verlag GmbH & Co. KGaA, Weinheim. (B) Schematic representations (left) and corresponding optical images (right) depicting the solution-based homoepitaxial growth, merging, and transfer processes of SC perovskite thin films. Reproduced with permission from ref. 172, Copyright 2020, Springer Nature. (C) Optical images of as-grown epitaxial α-$FAPbI_3$ thin films on Cl_xBr_y substrates, highlighting their high transparency and smooth surfaces, indicative of superior film quality. Scale bars: 4 mm (left). Cross-sectional SEM image of the epitaxial thin film showing a uniform thickness. Scale bar: 2 μm. Inset: Magnified SEM image of the heterostructure, revealing a well-defined interface. Scale bar: 200 nm (right). Reproduced with permission from ref. 174, Copyright 2020, Springer Nature. (D) Optical images of $CsPbCl_3$, $CsPbCl_{1.3}Br_{1.7}$, $CsPbBr_3$, $CsPbBr_{2.1}I_{0.9}$, and $CsPbBrI_2$ perovskite films deposited on sapphire with a monolayer graphene interlayer (top). Scale bar: 2 cm. Corresponding fluorescence microscopy images of the perovskite films on sapphire with graphene insertion (bottom). Scale bar: 500 μm. Reproduced with permission from ref. 175, Copyright 2025, Springer Nature.

hole mobility. Additionally, the strained growth stabilizes the α-$FAPbI_3$ phase through epitaxial stabilization and strain neutralization.[174]

(c) Remote epitaxy

Remote epitaxy involves the process of growing an epilayer on a substrate surface that is covered by a two-dimensional (2D) material, using the electrostatic potential of the substrate to indirectly interact with the adatoms during the growth of the epilayer.[177,178] This method does not require direct chemical bonds between the epilayer and the substrate but instead utilizes the screened electrostatic field to guide the alignment of the epilayer, causing it to adopt the substrate's orientation. The weak interaction between the substrate and the epilayer reduces the likelihood of new crystal nucleation, promoting the expansion of existing crystal domains. This results in lower dislocation densities and enhanced carrier lifetimes. In this approach, $CsPbBr_3$ was grown on a graphene/CaF_2 substrate, with nucleation potentially occurring through pinholes in the graphene layer, though this is less frequent compared to traditional ionic epitaxy.[179] Jang *et al.* investigate the impact of dislocations on carrier dynamics in halide perovskites using remote epitaxy on graphene-coated polar substrates. Their approach enables precise control over dislocation density, revealing a weak film-substrate interaction.[180] Recently, Yuan *et al.* demonstrated the remote epitaxial growth of crystalline perovskite films, which enabled their smooth integration into micro-LEDs with a pixel size as small as 4 μm (Fig. 6D).[175] By introducing a sub-nanometer graphene interlayer, they achieved remote epitaxy and successfully transferred perovskite films with relaxed strain. These micro-LEDs exhibited electroluminescence efficiency of 16.7% and a brightness of 4.0×10^5 cd m^{-2}. This exceptional performance is attributed to the reduced defects and efficient carrier transport within the epitaxial perovskites, which possess high crystallinity, relaxed strain, and thicknesses in the hundreds of nanometers. The free-standing perovskite films can be integrated into commercial electronic devices, allowing for independent pixel control, making them suitable for static and video displays.

3.3 Evaluation of SC perovskite growth methods

Recent advances in SC perovskite growth techniques are poised to revolutionize next-generation optoelectronic devices, yet complex challenges remain for industrial-scale applications. On the one hand, methods—such as inverse temperature crystallization (ITC), antisolvent vapor-assisted crystallization (AVC), solution temperature-lowering (STL), and flux-regulated crystallization—have enabled the synthesis of high-quality SC perovskites. These techniques offer significant flexibility in tuning crystal composition and dimensions but remain sensitive to nucleation dynamics and thermal management.

Conversely, solid-state approaches, exemplified by the Bridgman method, yield crystals of exceptional purity that are vital for applications in radiation detection and scintillation. However, the inherent slow cooling rates and the rigorous control required to maintain stable thermal gradients limit their throughput and practical applicability on an industrial scale.

In parallel, innovations in fabricating SC perovskite thin films are critical for integrating these materials into vertical device architectures. Traditional top-down methods like slicing, combined with emerging techniques such as roll-to-roll processing, space-confined growth, stamping, and surface-tension-assisted crystallization, provide new routes to produce films with precisely controlled thickness and excellent uniformity. While these methods show promise for photovoltaic and photodetector applications, achieving defect-free films with long-term stability and optimal interface characteristics remains a key priority.

Furthermore, epitaxial growth strategies—including both vapor-phase epitaxy and solution-based epitaxy (*via* homoepitaxy and heteroepitaxy)—offer a compelling pathway to engineer films with unparalleled crystallographic alignment and controlled interfacial properties. By fine-tuning lattice matching and minimizing dislocation densities, these approaches may effectively mitigate thermal and mechanical constraints, thus laying the groundwork for devices that combine superior performance with enhanced durability.

In summary, the field is advancing toward a holistic integration of growth optimization, precise crystallization control, and the synergistic use of established and emerging techniques. For instance, integrating machine learning (ML) and generative AI (GenAI) into SC perovskite growth can enhance control over crystallization dynamics, reproducibility, and identify key growth parameters that are often overlooked by conventional approaches. This multidisciplinary approach is essential for transitioning SC perovskite technologies from the laboratory to industrial production. With continued innovation in both bulk crystal synthesis and thin-film fabrication, the prospect of developing robust, high-performance optoelectronic devices based on SC perovskites is brighter than ever, heralding a new era in materials science and device engineering.

4. SC perovskites in photovoltaic technology

PSCs are an emerging photovoltaic technology that uses metal halide perovskites as light absorbers to enable highly efficient photo-to-electron conversion. In principle, the basic architecture of a PSC consists of a transparent conductive electrode, a hole transport layer, the perovskite absorber, an electron transport layer, and a metal electrode. The transparent conductive electrodes (*e.g.*, indium tin oxide (ITO),[181,182] fluorine-doped tin oxide (FTO), and indium zinc oxide (IZO)) provide structural support and allow sunlight to pass through to the active layers. When the photon energy ($h\nu$) exceeds the bandgap (E_g) of the perovskites, the photons are absorbed, exciting electrons from the valence band to the conduction band.

Subsequently, the excited electrons in the conduction band are rapidly transferred to the electron transport layer (*e.g.* TiO_2, C_{60}, or SnO_2),[213–216] due to the built-in electric field within the perovskite and the applied external voltage. Meanwhile, holes in the valence band are transferred to the hole transport layer (*e.g.* Spiro-OMeTAD, PTAA, or self-assemble monolayers

(SAMs)).[217–220] In each electron and hole transport layer, charge carriers (electrons and holes) are efficiently transported, extracted, and collected through the respective electrodes (cathode or anode), forming an external circuit current and completing the photo-to-electron conversion process. The representative SC perovskite photovoltaic devices are summarized in Table 2.

In general, single-junction PSCs are based on the n–i–p (conventional) (Fig. 7A) and p–i–n (inverted) (Fig. 7B) architectures, which are classified by the direction of incident light relative to the transparent conductive electrode. The inverted architecture has become the mainstream structure in perovskite photovoltaics due to its excellent stability and compatibility with tandem applications. The efficiency of single-junction PSCs based on polycrystalline films has reached 27% (Fig. 7C),[221] with significant advances in large-area fabrication and tandem cell development.[222–225] However, stability issues remain the primary barriers to the industrialization and commercialization of perovskite-based devices. SC perovskites, with their superior optoelectronic properties, hold great promise for achieving long-term and reliable optoelectronic devices.

SC PSCs, which employ SC perovskite as the light absorption layer, were first reported in 2016, and by 2025, their efficiency has surpassed 25%,[185] demonstrating an efficiency evolution comparable to that of polycrystalline PSCs (Fig. 7C). The minimal grain boundaries in SC perovskites lead to a lower defect density, longer charge carrier lifetimes, and enhanced mobility—all of which are beneficial for improving the efficiency and stability of perovskite-based photovoltaics. Hence, SC perovskites are regarded as an essential step towards achieving long-term stability in perovskite photovoltaics. This section provides a detailed overview of the advances in SC PSCs, focusing on the impact of SC perovskite composition on photovoltaic performance, as well as the main strategies for improving the efficiency of SC PSCs.

4.1 SC $MAPbBr_3$-based PSCs

$MAPbBr_3$ is one of the earliest studied organic–inorganic hybrid perovskite materials. In 2009, $MAPbBr_3$ and $MAPbI_3$ were first introduced into the field of solar cells.[45] In 2015, Shi *et al.* reported the growth of SC $MAPbBr_3$, exceeding 100 cubic meters, using an antisolvent vapor-assisted crystallization method. The SC $MAPbBr_3$, with an optical bandgap of 2.21 eV, a low defect density of 5.8×10^9 cm^{-3}, and a long carrier diffusion length of over 3 μm, highlights its promising potential for high-performance solar cells.[47] Due to the wide bandgap and narrow absorption range of $MAPbBr_3$ perovskites, solar cells based on SC $MAPbBr_3$ represent the early stage of SC perovskite solar cell development. The highest efficiency to date was achieved by Wu *et al.*, who reported SC $MAPbBr_3$ perovskite microarray devices using an Ostwald ripening assisted photolithography (ORAP) patterning method, reaching a power conversion efficiency of 7.84%.

4.2 SC $MAPbI_3$-based PSCs

4.2.1 Overview of key developments. Since $MAPbI_3$ perovskite was first introduced as a sensitizer in dye-sensitized solar cells, achieving a power conversion efficiency (PCE) of 3.8% in 2009,[45] the first solid-state PSCs were reported in 2012,[46] $MAPbI_3$ perovskite has played an essential role in each milestone of PSC development. The SC $MAPbI_3$, first reported in 2015, exhibited a carrier diffusion length of exceeding 175 μm and a carrier lifetime of 262 μs,[48] highlighting the excellent photoelectronic properties and potential of $MAPbI_3$ perovskite for photovoltaic applications.

However, how to directly integrate the bulk single crystals with photovoltaic technology has been challenging. Therefore, numerous studies have been conducted to achieve the conversion of SC perovskites to SC devices. Ye *et al.* introduced a droplet-pinned crystallization (DPC) method to grow SC $MAPbI_3$ arrays with a thickness of 3 μm on ITO/PEDOT: PSS substrates, achieving the first SC $MAPbI_3$ PSC with a PCE of 1.73%.[203] Yue *et al.* developed a seeded space-limited inverse-temperature crystallization (SSLITC) method for SC perovskite plate growth, where $MAPbI_3$ seed crystals were introduced into a confined space to promote lateral growth, yielding SC flakes with maximum lateral dimensions of 2 mm and a flexible SC PSC with a PCE of over 4% and a J_{sc} value of 22 mA cm^{-2}.[198] Chen *et al.* applied a diffusion-facilitated space-confined method to prepare SC $MAPbI_3$ films with controllable thickness (Fig. 8A), which could be reduced to the micron level. It was found that the optical bandgap of the SC $MAPbI_3$ perovskite was narrower, and its optical absorption extended to 820 nm, which is 20 nm broader than the polycrystalline perovskite. The champion SC PSCs, based on micron-thick $MAPbI_3$, achieved an impressive efficiency of 17.8%, marking a breakthrough in SC PSCs.[67] Besides, Chen *et al.* proposed a solution space-limited inverse-temperature crystal growth strategy on ITO/PTAA substrates, achieving 21% efficiency and an impressive fill factor of 84.3% in 20-μm thick $MAPbI_3$ SC PSCs, with their photovoltaic performance competitive with that of $MAPbI_3$ polycrystalline PSCs from the same period.[193]

4.2.2 Strategies for achieving high-performance SC $MAPbI_3$-based PSCs. The crystallization dynamics affect the quality and surface defect density of SC $MAPbI_3$ perovskites, which has a significant impact on the efficiency and stability of the corresponding photovoltaic devices. The mainstream method for growing SC $MAPbI_3$ typically involves growth temperatures above 120 °C. However, due to the inferior thermal stability of $MAPbI_3$, it often leads to the generation of bulk and surface defects, which makes $MAPbI_3$ prone to decomposition. Alsalloum *et al.* reported a solvent engineering approach for the low-temperature growth of SC $MAPbI_3$, yielding high-quality SC films with longer carrier lifetimes and achieving efficiencies of up to 21.9% for SC $MAPbI_3$ devices.[192] To further reduce the defect density on the surface of SC $MAPbI_3$ and improve the performance of SC PSCs, surface passivation is another key approach. Younas *et al.* introduced long-chain ammonium compounds, *n*-butylammonium iodide (BAI) and *n*-propylammonium iodide (PAI), into the SC $MAPbI_3$ and first reported the 2D/3D-blended perovskite single crystals *via* the inverse temperature crystallization process, along with the corresponding SC devices. Long-chain ammonium salts reduced

Table 2 Summary of reported SC perovskite photovoltaic devices

SC perovskite composition	Preparation methods	PCE (%)	Device structure
$Cs_{0.05}FA_{0.95}PbI_3$	SLITC	23.1,[183] 23.8,[184] 24.29,[52] 25.82[185]	p–i–n
$GA_{0.015}FA_{0.985}PbI_3$	SLITC	9.1[186]	Lateral
$FA_{0.6}MA_{0.4}PbI_3$	SLITC	23.1,[187] 22.8[188]	p–i–n
$FA_{0.55}MA_{0.45}PbI_3$	SLITC	19.4[145]	p–i–n
$FA_{0.2}MA_{0.8}PbI_3$	SLITC	23.4[189]	p–i–n
$(FAPbI_3)_{0.85}(MAPbBr_3)_{0.15}$	PASV	12.18[190]	p–i–n
$MAPbI_3$	SLITC	16.9,[191] 21.93,[192] 21.09,[193] 24.12,[194] 22.1,[195] 22.2,[196] 6.37[197]	p–i–n
$MAPbI_3$	SSLITC	4.4(flexible)[198]	p–i–n
$MAPbI_3$	DSLC	15.65[199]	p–i–n
$MAPbI_3$	BU	5.9%[200]	Lateral
$MAPbI_3$	SPSCD	1.88[201]	Lateral
$MAPbI_3$	GCLCG	4.83,[163] 7.43[202]	Lateral
$MAPbI_3$	DPC	1.73[203]	p–i–n
$MAPbI_3$	DFSC	17.8[67]	p–i–n
$MAPbI_3$	SLPC	<4[204]	n–i–p
$MAPbI_3$	DFSC	11.15[205]	Lateral
$MAPbI_3$	SC	8.78[206]	n–i–p
$MAPbI_3$	SC	15.67[207]	p–i–n
BAI: $MAPbI_3$	SLITC	5.37[197]	p–i–n
$MAPbBr_3$	DTAC	6.5%[208]	n–i–p
$MAPbBr_3$	SLITC	4.31,[209] 7.11[210]	n–i–p
$MAPbBr_3$	ORAP	7.84(microarray)[211]	n–i–p
$MAPb_{0.5+x}Sn_{0.5-x}I_3$	LEGT	20.4(graded)[172]	p–i–n
$CsSnI_3$	PSE	11.7[212]	Lateral

Note: SLITC (space limited inverse temperature crystallization method); PASV (polydimethylsiloxane-assisted solvent evaporation method); SSLITC (seeded space-limited inverse-temperature crystallization method); DSLC (differential space-limited crystallization); SPSCD (supersaturated precursor solution cooling down method); GCLCG (geometrically confined lateral crystal growth method); DCP (droplet-pinned crystallization method); DFSC (diffusion facilitated space-confined method); SLPC (slice the large perovskite crystals); DTAC (cavitation-triggered asymmetrical crystallization method); ORAP (Ostwald ripening assisted photolithography patterning process); LEGT (lithography-assisted epitaxial-growth-and-transfer method); TD (top-down approaches); PSE (precursor solution evaporation); BU (bottom-up technique); SC (space confine method).

surface defect density and suppressed non-radiative recombination, resulting in only a 3.3% efficiency loss in 2D/3D-blended devices after four weeks, compared to 22.3% losses in control devices.[197] Guo *et al.* modified the surface defects of SC $MAPbI_3$ with the bifunctional molecule 3-mercaptopropyl(dimethoxy)methylsilane (MDMS) and enhance its surface hydrophobicity, resulting in SC PSCs with an efficiency of 22.2% and improved humidity stability (Fig. 8B). The MDMS-modified devices retained over 90% of their initial efficiency after 950 hours of aging at temperature of 25 ± 2 °C and relative humidity of $26 \pm 2\%$.[196]

Defects at the buried interface of SC $MAPbI_3$ PSCs is another major factor affecting their stability. In general, poly(triarylamine) (PTAA), as a popular hole transport layer (HTL) in SC PSC architecture, exhibits weak interaction due to its large steric hindrance. To enhance the HTL/perovskite interaction and passivate deep-level defects at the bottom interface, Li *et al.* introduced hydrophobic poly(3-hexylthiophene) (P3HT) into PTAA (Fig. 8C), forming coordination bonds between the sulfur atoms in P3HT and Pb^{2+}, which improved the HTL/perovskite interface, reduced interface and bulk defects, suppressed carrier recombination, enhanced charge transport/extraction. The $MAPbI_3$ SC PSCs based on the PTAA/P3HT blend HTL achieved a PCE of 22.1% under standard 1-sun illumination and an indoor efficiency of 39.2% under 1000 lux irradiation.[195] Moreover, Zhao *et al.* reported a synergistic interfacial engineering and solvent engineering strategy to simultaneously suppress nonradiative recombination in both the bulk and at the interface of SC PSCs. The introduced organic small molecule MeO-2PACz into PTAA regulated the nucleation of single crystals through interfacial engineering, while the formation of PbI^{3-}/PbI_4^{2-}-γ-butyrolactone complex controlled the crystallization rate and suppressed organic decomposition through solvent engineering. The champion SC $MAPbI_3$ PSC achieved a PCE of 24.12%, surpassing the efficiency records of polycrystalline PSCs (23.1%) and SC-PSCs (22.1%) based on $MAPbI_3$, while the unencapsulated SC-PSC device exhibited only a 10% degradation after 1400 hours of storage under a nitrogen atmosphere.[194]

4.3 Mixed cation SC PSCs

4.3.1 Overview of key developments. SC $MAPbI_3$ has an optical bandgap of ~1.51 eV, while the ideal optimal bandgap for maximizing solar spectrum absorption lies between 1.3 eV and 1.4 eV, which theoretically contributes to a higher PCE. Thus, it is essential to develop mixed cation SC perovskites to achieve a narrower optical bandgap and an extended spectral absorption range. Huang *et al.* employed a polydimethylsiloxane-assisted solvent evaporation method (Fig. 9A) to produce SC $(FAPbI_3)_{0.85}(MAPbBr_3)_{0.15}$ thin films, achieving an efficiency of 12.18% in an inverted SC PSC with the architecture of ITO/NiO_x/$(FAPbI_3)_{0.85}(MAPbBr_3)_{0.15}$/$TiO_2$/Ag.[190] It has also been demonstrated that the ideal bandgap for light-absorbing materials ranges between 1.1 eV and 1.4 eV, corresponding to the theoretical maximum photon-to-electron conversion efficiency limit. However, most state-of-the-art high performance thin-film PSCs are based on $FAPbI_3$, which has a bandgap of 1.48 eV, falling

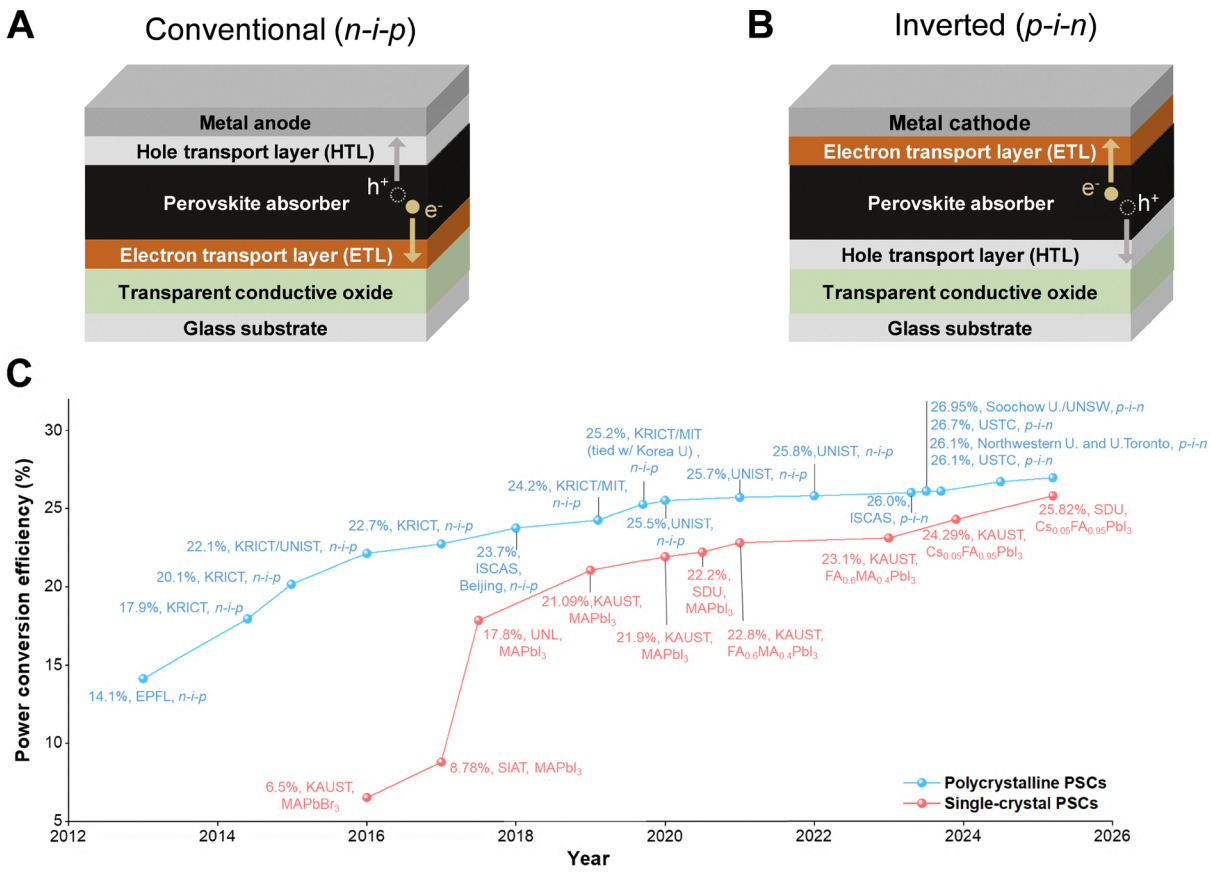

Fig. 7 (A) and (B) Typical architectures of n–i–p and p–i–n PSCs. (C) Timeline of single-junction PSC efficiency for polycrystalline (certified) and SC (non-certified) perovskites. Certified data were extracted from the NREL best research-cell efficiency chart (ref. 221), while the efficiency data of SC perovskite solar cells is obtained from ref. 52, 67, 185, 187, 188, 192, 193, 196, 206 and 208.

short of the ideal limit. Alsalloum *et al.* found that the mixed cation $FA_{0.55}MA_{0.45}PbI_3$ single crystal exhibits a 50 meV red shift in the external quantum efficiency band edge compared to its polycrystalline film. The $FA_{0.55}MA_{0.45}PbI_3$ SC PSCs also achieved a J_{sc} value of 26 mA cm^{-2} with a PCE of 22.8%, providing a pathway for lead halide PSCs to approach the Shockley–Queisser limit in efficiency.[188]

4.3.2 Strategies for achieving high-performance mixed cation SC PSCs. Although SC perovskites have fewer grain boundaries than the polycrystalline perovskites, a large number of surface impurities still remain during the solution-based growth process, limiting the overall performance of SC PSCs. Xie *et al.* optimized the growth of $FA_{0.55}MA_{0.45}PbI_3$ single crystals by controlling the ion diffusion velocity in confined spaces, which reduced trap density, increased ion migration activation energy, and improved the light stability of the as-growth single crystals. The developed SC PSCs showed no efficiency degradation after 330 hours of continuous 1-sun operation under maximum power point tracking.[145] Wu *et al.* synthesized SC $FA_{0.75}MA_{0.25}PbI_3$ perovskite *via* the space-limited inverse temperature crystallization method and improved crystal quality through trioctylphosphine oxide (TOPO) surface passivation. The TOPO-modified SC devices exhibited an increase in efficiency from 11.9% to 15.65%, with enhanced ambient stability (room temperature, 50% ± 10% relative humidity), retaining over 76% of their initial efficiencies after 9 days.[199] Liu *et al.*, inspired by the self-cleaning effect of lotus leaf, introduced amphiphilic long-chain cetyltrimethylammonium chloride molecules into the perovskite solution (Fig. 9B), imparting hydrophobic properties to the crystals, which facilitated the spontaneous removal of residual perovskite solution and resulted in a PCE of 23.4% in the SC $FA_{0.2}MA_{0.8}PbI_3$ PSC device.[189] Almasabi *et al.* successfully fabricated SC $FA_{0.6}MA_{0.4}PbI_3$ on a hydrophilic self-assembled monolayer [2-(3,6-dimethoxy-9*H*-carbazol-9-yl)ethyl]phosphonic acid (MeO-2PACz) and the corresponding SC PSCs. Due to the stronger mechanical adhesion between the perovskite and MeO-2PACz, the as-prepared MeO-2PACz-based devices (Fig. 9C) exhibited an efficiency of up to 23.1%, with enhanced operational stability, retaining 75% of their initial efficiencies after 730 hours of maximum power point tracking, while the PTAA-based devices experienced 40% efficiency loss within a few hours.[51]

Methylammonium iodide has a low decomposition temperature and tends to decompose during prolonged high-temperature crystallization, leading to the formation of defects on the surface of SC perovskites. To address this, Lintangpradipto *et al.* developed an MA-free SC perovskite, $Cs_{0.05}FA_{0.95}PbI_3$, achieving a 24.29% efficiency for the as-prepared SC PSCs and exhibiting

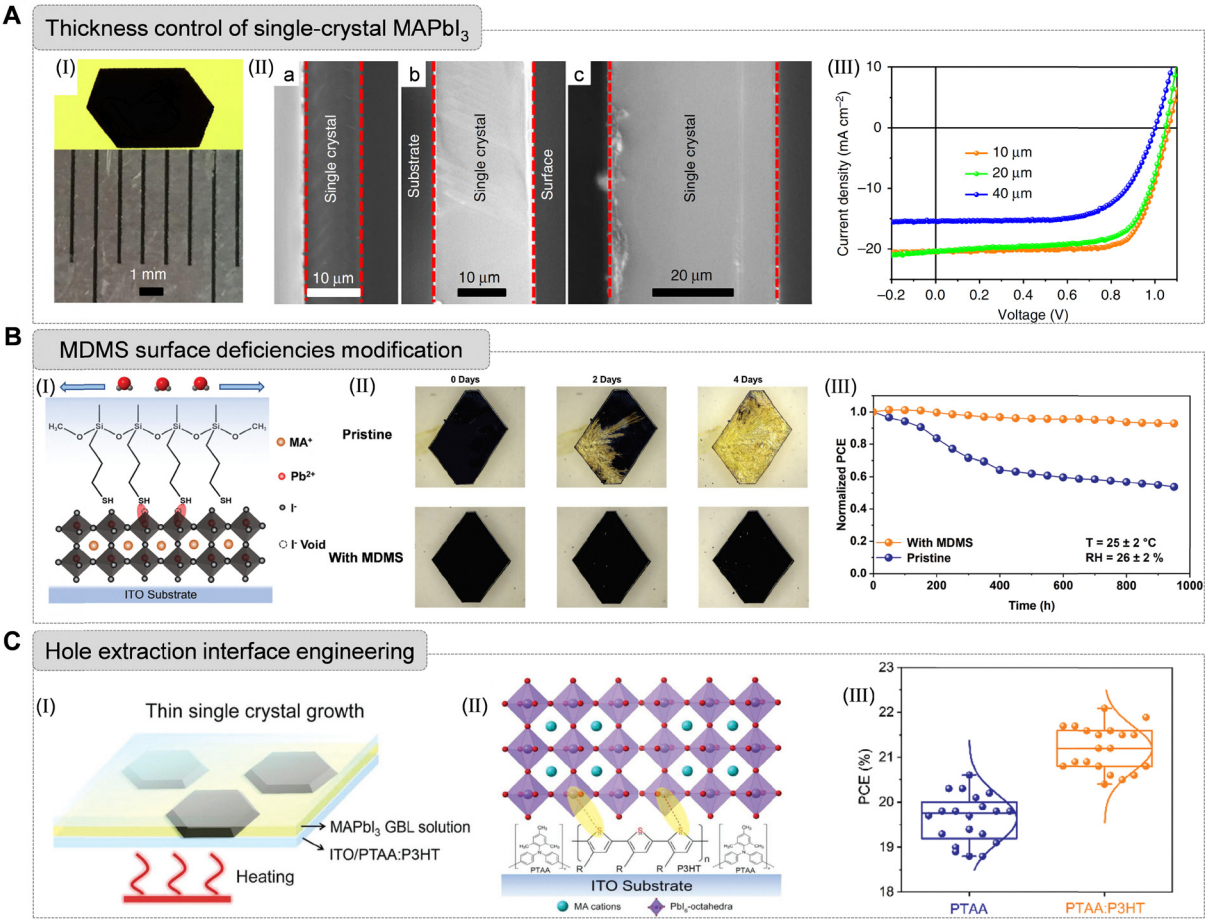

Fig. 8 (A) Characterization of a SC $MAPbI_3$ perovskite. (I) Photograph of a $MAPbI_3$ thin single crystal using a hydrophobic interface confined lateral growth method. (II) Cross-sectional SEM images of the $MAPbI_3$ thin single crystals with different thickness: (a) ~10 μm, (b) ~20 μm, (c) ~ 40 μm, (III) current density–voltage of the optimal SC solar cells using the corresponding $MAPbI_3$ thin single crystals. Reproduced with permission from ref. 67, Copyright 2017, Springer Nature. (B) Schematic representation of (I) the interaction between MDMS molecules and the $MAPbI_3$ crystal surface, (II) optical images of the pristine and MDMS-modified $MAPbI_3$ single crystals after aging in high-humidity conditions for 4 days (T = 25 ± 2 °C, RH = 85 ± 5%), (III) normalized PCE evolution of non-encapsulated SC $MAPbI_3$ PSCs after 950 hours of storage in ambient air. Reproduced with permission from ref. 196, Copyright 2023, Wiley-VCH GmbH. (C) (I) Schematic illustration of the space-confined growth method for $MAPbI_3$ single crystals, (II) schematic diagram of the interaction between P3HT molecules and the perovskite single crystal, (III) statistical distribution of PCE among 20 devices based on PTAA and blended PTAA: P3HT HTLs. Reproduced with permission from ref. 195, Copyright 2022, Wiley-VCH GmbH.

superior thermal and humidity stability compared to the polycrystalline $FA_{0.6}MA_{0.4}PbI_3$-based PSCs.[52] The MA-free SC perovskite ($Cs_{0.05}FA_{0.95}PbI_3$) has become one of the most widely studied compositions, with its optoelectronic performance further improved through systematic optimization. Jiang *et al.* proposed an *in situ* growth strategy for a 1D $MDAPb_2I_6$ perovskite layer on the surface of $Cs_{0.05}FA_{0.95}PbI_3$, constructing a SC PSC device with the architecture of ITO/PTAA/$Cs_{0.05}FA_{0.95}PbI_3$/$MDAPb_2I_6$ (1D)/C_{60}/BCP/Cu. The introduction of the 1D perovskite contributed to reduced iodine vacancy defects on the surface of $Cs_{0.05}FA_{0.95}PbI_3$ crystal and suppressed non-radiative recombination at the perovskite/transport layer interface. Consequently, the T_{90} stability of the as-prepared SC PSCs was improved, increasing from 260 hours in the control group to 1000 hours.[184] In addition, Liu *et al.* introduced 2,6-difluoro-3-nitrobenzonitrile ($FCNO_2$) molecules into the hole transport layer to regulate the nucleation process of SC $Cs_{0.05}FA_{0.95}PbI_3$, modulating the residual solution, voids, and small-sized crystals at the substrate surface, yielding a record efficiency of 25.82% and negligible efficiency loss after 500 h of thermal aging.[185]

Currently, $Cs_{0.05}FA_{0.95}PbI_3$ is the mainstream perovskite composition used in SC PSCs, offering a balanced compromise between device efficiency and phase stability. This formulation also closely resembles that of high-efficiency polycrystalline perovskites. However, its photovoltaic bandgap—or more precisely, its light absorption range—remain inferior to that of $FAPbI_3$. Recently, Lv *et al.*[186] successfully fabricated SC $GA_{0.015}FA_{0.985}PbI_3$ perovskite thin films, which are compositionally close to $FAPbI_3$ and exhibit excellent stability, although the resulting device showed lower efficiency. Therefore, developing high-quality SC $FAPbI_3$ thin films and translating them into high-performance SC devices will be a key research focus in the future.

4.4 Tin-based SC PSCs

Although Pb-based perovskites are the mainstream perovskite materials for photovoltaic devices, the toxicity and potential

environmental concerns associated with Pb have led to increased investigation on Sn-based perovskites. Dai *et al.* systematically reported the crystal, optical, and electrical properties of $CsSnI_3$ perovskite in SC nanowires (NWs) and designed a frontal electrode structure for photovoltaic application based on the unique characteristics of the nanowire structure. The low defect density, broad absorption spectrum, and high mobility of SC $CsSnI_3$ NWs enabled the achievement of a PCE of 11.7%, marking the first application of the front-surface-field mechanism in photovoltaic devices.[212] Besides, Wu *et al.* found that the bulk carrier lifetimes of the SC $CsSnI_3$ can reach up to 6.6 ns, with a doping concentration of 4.5×10^{17} cm^{-3}, and a minority-carrier diffusion length of approximately 1 μm. More importantly, the SC $CsSnI_3$ exhibited a relative low surface recombination velocity of 2×10^3 $cm{\cdot}s^{-1}$, similar to the Pb-based perovskites, with a theoretical efficiency of 23% in optimized SC $CsSnI_3$ PSCs.[226] Lei *et al.* demonstrated a solution-based lithography-assisted epitaxial-growth-and-transfer method for fabricating SC perovskites with precise control over thickness (from ~600 nm to 100 μm), area (continuous films up to 5.5 × 5.5 cm^2), and composition gradient ($MAPbI_3$ to $MAPb_{0.5}Sn_{0.5}I_3$ for bandgap engineering), with the average efficiency of SC PSCs based on Pb–Sn gradient structure reaching 18.77%. This method overcomes existing limitations in SC perovskite fabrication process and introduces a scalable, transferable, and compositionally tunable approach for achieving high-performance and stable SC perovskite optoelectronic devices.[172]

Tin-based SC perovskites exhibit several advantages over lead-based perovskites in photon utilization, environmental friendliness, and biocompatibility. However, their photovoltaic performance remains inferior due to inherent poor stability and limitations in controlling crystallization kinetics. Therefore, the introduction of oxidation inhibitors and precisely regulating the crystallization kinetics of tin-based perovskites to acquire stable SC thin films will be a key direction for future research.

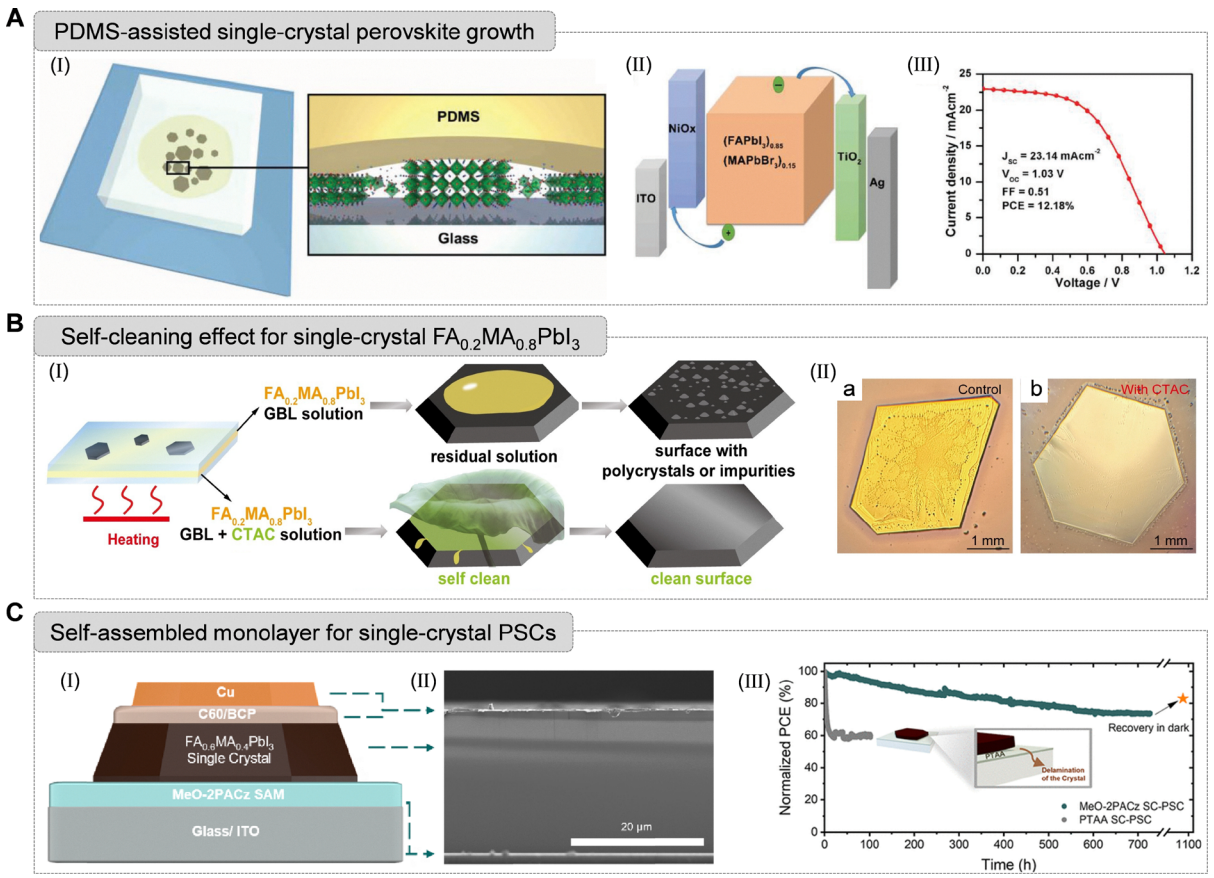

Fig. 9 (A) PDMS-assisted solvent evaporation crystallization method for single-crystal $(FAPbI_3)_{0.85}(MAPbBr_3)_{0.15}$ perovskite growth. (I) Schematic of the growth mechanism of single-crystal $(FAPbI_3)_{0.85}(MAPbBr_3)_{0.15}$ *via* the PDMS-assisted solvent evaporation crystallization method, (II) energy level band alignment, and (III) the *J*–*V* curve of the best-performance single-crystal $(FAPbI_3)_{0.85}(MAPbBr_3)_{0.15}$ PSC device. Reproduced with permission from ref. 190, Copyright 2018, Wiley-VCH Verlag GmbH & Co. KGaA, Weinheim. (B) Self-cleaning effect for single-crystal $FA_{0.2}MA_{0.8}PbI_3$ growth. (I) Schematic presentation of $FA_{0.2}MA_{0.8}PbI_3$ single crystals grown *via* the space-confined method with and without CTAC molecule. (II) Optical microscope images single-crystal $FA_{0.2}MA_{0.8}PbI_3$ perovskites grown with and without CTAC. Reproduced with permission from ref. 189, Copyright 2024, Wiley-VCH GmbH. (C) (I) Schematic of the single-crystal $FA_{0.6}MA_{0.4}PbI_3$ PSC architecture; (II) cross-sectional SEM image of the device; (III) long-term operational stability under continuous output at the maximum power point under 1-sun illumination, showing the normalized power conversion efficiency of single-crystal $FA_{0.6}MA_{0.4}PbI_3$ PSCs fabricated with PTAA or MeO-2PACz SAM as the HTL. Reproduced with permission from ref. 51, Copyright 2023, American Chemical Society.

4.5 Challenges of SC-PSCs

As discussed in Section 3 on SC perovskite growth methods, high-quality SC perovskite bulks and large-area SC thin films can be achieved *via* various approaches. Although SC-PSCs have demonstrated impressive efficiencies exceeding 25%, they still lag behind their polycrystalline counterparts in several key aspects, including efficiency, device architecture versatility, scalability, and long-term stability. This discrepancy primarily arises from the absence of well-developed methodologies for integrating high-quality and low-defect SC perovskites into device architectures that simultaneously achieve high efficiency and long-term stability.

Due to the limited carrier lifetime and diffusion length, the thickness of SC perovskites should be less than 20 micrometers, which directly hinders the application of SC perovskite bulks in SC-PSCs. To date, high-performance SC PSCs are typically fabricated using SC perovskite thin films grown *via* the space-confined inverse temperature crystallization method. However, this technique still suffers from unresolved issues, including residual solvents trapped between the crystal and the substrate, mechanical damage during crystal delamination, and inferior interfacial contacts. These issues, combined with the intrinsic trade-off between sufficient absorption and minimal voltage loss in SC thin layers, have prevented SC PSCs from realizing their theoretical efficiency and stability. Therefore, a key priority for advancing SC perovskite photovoltaic technology is to establish effective strategies for integrating high-quality SCs into device architectures that simultaneously enable efficient light harvesting, low recombination losses, and long-term stability.

5. SC perovskites for high-energy radiation detection

High-energy ionizing radiation, including X-rays (wavelengths: 0.01–10 nm) and gamma rays (wavelengths <0.01 nm), has strong penetrating power, making it suitable for the non-destructive examination of dense materials. The interaction of these rays with atomic electrons leads to the ionization of the detected material, while variations in photon intensity (dose rate), direction, phase, and energy provide detailed structural information. X-rays are widely used in medical imaging, security screening, container inspection, defect detection, quality control within the materials industry, food safety assessment, and monitoring of industrial pollution. Similarly, gamma rays play an essential role in cancer radiotherapy, sterilization of medical equipment, food irradiation for preservation, and industrial radiography for the inspection of welds and metal structures.

5.1 Working mechanism

(a) Radiation absorption

High-energy radiation photons interact with matter through four main mechanisms, including the photoelectric effect, Rayleigh scattering, Compton scattering, and electron–positron pair generation. In the photoelectric effect, a photon is absorbed by an atom, transferring its energy to an electron, which is subsequently ejected as a photoelectron. Rayleigh scattering involves the elastic interaction between a photon and a bound electron, resulting in minimal energy transfer and a slight deflection of the photon. Compton scattering occurs when a photon collides with an electron, transferring a portion of of its energy to the electron, which is then ejected, while the photon changes direction. Electron–hole pair generation takes place when a photon, influenced by the Coulomb field of a nucleus or orbiting electrons, produces an electron–hole pair.[227] The fundamental characteristics of these interactions are shown in Fig. 10. In both the photoelectric effect and Compton scattering, photons interacting with semiconductors generate high-energy secondary electrons, including photoelectrons, Auger electrons, and recoil electrons.

(b) Carrier generation and separation

These energetic electrons further ionize the material, generating numerous low-energy free electrons. The free electrons are excited to the conduction band, while holes remain in the valence band. As holes migrate to the top of the valence band, electrons gradually relax to lower energy states within the conduction band. Through successive collisions and collective motion, free electrons eventually settle at the bottom of the conduction band, leading to the formation of electron–hole pairs in the semiconductor under X-ray irradiation.[228]

(c) Charge drift and collection

The generated electron–hole pairs can either be collected or undergo recombination under the electric field, resulting in the emission of scintillation light or the release of energy.[92] The collected light or energy is then measured by an external circuit to obtain the detection result.

5.2 Operational mode of high-energy radiation (X-ray) detectors

For SC perovskites, electron–hole pairs can be efficiently collected by external circuits due to their excellent charge transport properties, which lead to direct energy release. This process is referred to as direct detection, and the working modes can be classified into two types.[89,229–232]

(a) Current mode

X-ray detectors used in dosimeters and medical imaging operate in current mode, where a high photon flux ensures a sufficient SNR, smooth imaging, and fast frame rates. When multiple photons simultaneously reach the detector, each X-ray photon is directly converted into free charge carriers *via* the photoelectric effect. These carriers are then collected by electrodes under an external electric field. During Compton scattering, an incident photon interacts with an electron, resulting in the photon being deflected at a scattering angle relative to its original trajectory. A portion of the photon's energy is transferred to the electron, with the exact amount depending on the photon's initial energy and the scattering angle. In both the photoelectric effect and Compton scattering, a substantial number of charge carriers are generated, leading to X-ray photon attenuation. These energized carriers are collected by electrodes under an external bias, producing a current signal. The total attenuated X-ray photons contribute to the average

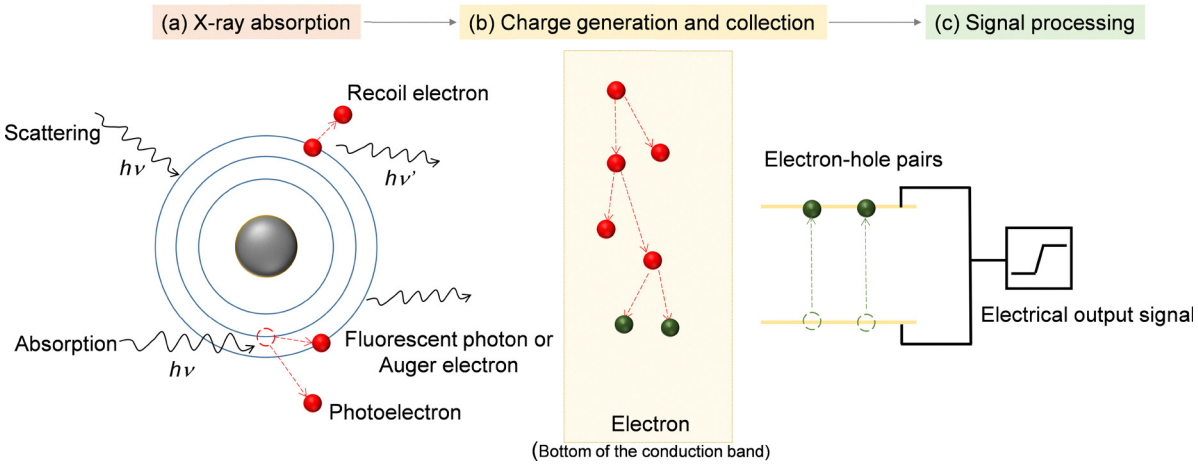

Fig. 10 Schematic diagram of the working mechanism of high-energy radiation detection, illustrating (a) X-ray absorption, (b) charge generation and collection, and (c) signal processing.

signal current over time. The intensity of the transmitted photon flux can be expressed by the equation:

$$I = I_0 \times e^{-\alpha p l}$$

where I_0 is the initial photon flux intensity, α is the mass attenuation coefficient, p is the material density, and l is the length of the photon-material interaction. The product $\alpha\rho$, commonly expressed as μ_0, is known as the linear attenuation coefficient and is frequently used to characterize the capacity of a material to attenuate radiation energy.

(b) Pulse mode

Radiation detectors used in photon counting, spectroscopy, and nuclear reaction monitoring typically operate in voltage mode. Unlike current mode, which has high photon flux, voltage mode operates at relatively low photon flux, where high-energy photons arrive at the detector individually. Each photon generates a specific number of electron–hole pairs, and the resulting charge is measured as a pulse signal, whose intensity is directly proportional to the photon energy. By counting individual photon energies, an X-ray photon energy spectrum can be constructed. To enhance the detection of weak signals, a charge-sensitive preamplifier is commonly used to collect the charges generated within the detector, converting them into a voltage signal. This signal is then processed by a shaping amplifier, which outputs a quasi-Gaussian waveform, optimizing it for transmission through communication channels while maintaining proportionality to photon energy. A multi-channel analyzer subsequently records individual photon events, enabling the determination of radiation quantum and energy, thereby producing a complete X-ray energy spectrum.[233,234]

Typically, radiation detectors operating in current mode include silicon (Si), amorphous selenium (α-Se), mercury iodide (HgI_2), and cadmium zinc telluride ($Cd_{1-x}Zn_xTe$), while those operating in voltage mode include high-purity germanium (HP–Ge), cadmium zinc telluride ($Cd_{1-x}Zn_xTe$), and thallium bromide (TlBr).[235,236]

5.3 Architecture of single-crystal high-energy radiation (X-ray) detectors

The planar structure device consists of two parallel electrodes (*e.g.*, Au, Ag, Pt, C, *etc.*) deposited on the surface of the single crystal, as shown in Fig. 11A, with the electric field direction perpendicular to the incident radiation. This method makes planar devices suitable for preliminary performance characterization and intrinsic property studies of SC perovskites. Planar devices provide several advantages, including faster response times due to the minimized electrode spacing, making them ideal for real-time imaging. In addition, they are well-suited for low X-ray dose detection (low detection limit), low-voltage operation, and ease of fabrication and integration.[121,235,242]

A vertical structure device, which has high sensitivity and a broad dynamic range, includes a single crystal positioned between two electrodes, as illustrated in Fig. 11B, with the electric field oriented parallel to the incident radiation. The introduction of passivation or interface layer on the electrode surface enhances the collection rate of photogenerated carriers, while simultaneously, the absorption of X-rays theoretically increases with crystal thickness, approaching the absorption limit of materials. Besides, optimized crystal quality and reduced defects are beneficial for efficient charge transport, leading to improved device sensitivity.[238]

A Schottky junction is formed between the single crystal and the metal electrode, as depicted in Fig. 11C, enhancing carrier separation through the built-in electric field. Schottky photodiodes can be fabricated using an asymmetric electrode configuration to create an internal electric field that facilitates the extraction of photogenerated electrons and holes.[243] Moreover, the asymmetric electrode configuration, with various Schottky barrier potentials, suppresses undesirable carriers, thereby minimizing leakage current under reverse bias.[238] This design benefits from reduced dark current and improved SNR, making it suitable for weak signal detection, such as high-resolution gamma-ray detection.

A p–n junction or heterojunction is formed on the surface of a perovskite single crystal by integrating other materials such

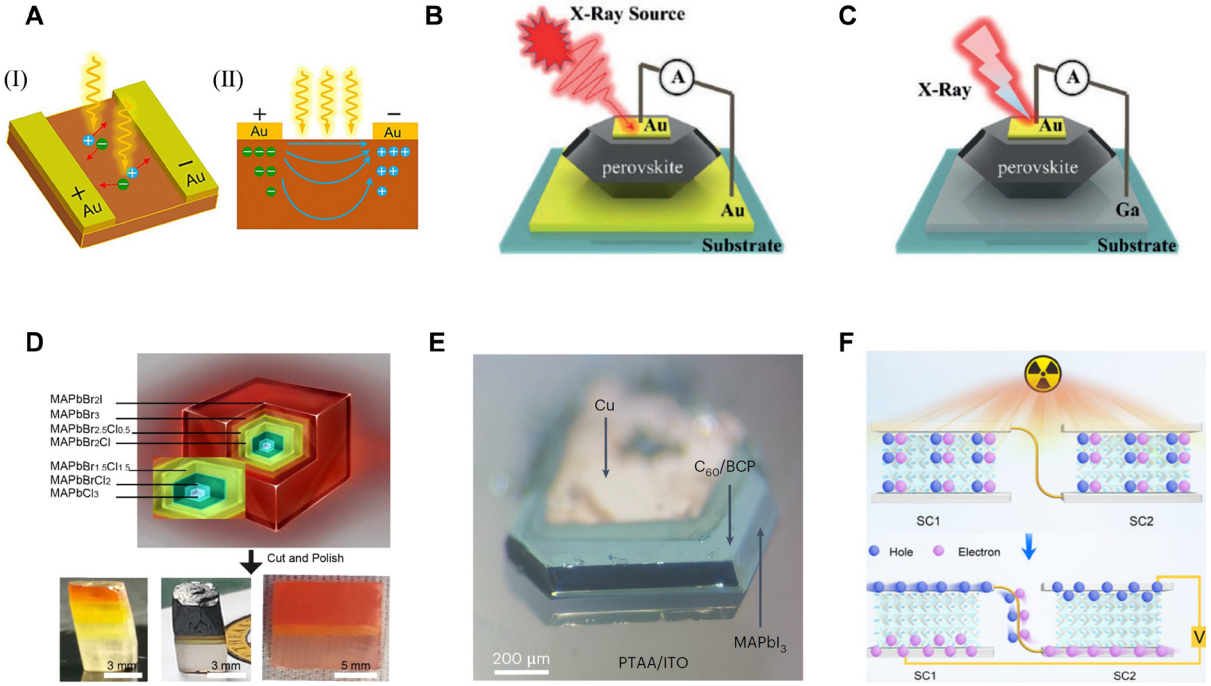

Fig. 11 (A) Planar structure of perovskite-based X-ray detector (I) and schematic diagram of the electric field configuration (II). Reproduced with permission from ref. 237, Copyright 2020, Wiley-VCH Verlag GmbH & Co. KGaA, Weinheim. (B) Vertical structure: symmetrical electrode design and (C) Schottky photodiode structure: asymmetric electrode design. Reproduced with permission from ref. 238, Copyright 2019, Wiley-VCH Verlag GmbH & Co. KGaA, Weinheim. (D) Heterojunction structure and the optical photos of the SC perovskites. Reproduced with permission from ref. 239, Copyright 2020, American Chemical Society. (E) Photodiode structure of a SC $MAPbI_3$ grown directly on a PTAA/ITO substrate. Reproduced with permission from ref. 240, Copyright 2023, Springer Nature. (F) Cascade-connected structure and its corresponding working diagram. Reproduced with permission from ref. 241, Copyright 2024, American Chemical Society.

as Si, CdTe, or low-dimensional perovskites, as depicted in Fig. 11D. Optimization of the interface energy level alignment is essential for enhancing carrier separation, which leads to improved collection of photogenerated carrier, reduced recombination losses, and suppressed ion migration in three-dimensional SC perovskites, enabling high-resolution imaging.[239] Furthermore, it has been shown that devices fabricated from single crystals with varying densities can distinguish X-rays of different energy levels, which is beneficial for high-energy radiation detection. This approach addresses the intrinsic absorption limitations of single-component materials that restrict imaging resolution. By combining materials with different densities, the superposition effect enhances energy resolution and overcomes the radiation absorption limitations of a single-component system.[244]

SC materials are used to fabricate photodiodes with transparent electrodes, such as ITO, and metal back electrodes, as shown in Fig. 11E. The incorporation of a hole transport layer (HTL) and an electron transport layer (ETL) optimizes charge separation, enhancing device sensitivity and responsivity for detection applications.[240] The photodiode structure could enable efficient electron/hole separation and transport. However, limitations in SC size and reproducibility continue to pose challenges, hindering the feasibility of large-scale fabrication and compromising the reliability of device performance.

A typical cascade device consists of several single crystals connected in series, designed to increase dark current, which can lower the detection limit and enable highly sensitive monitoring of low-dose X-ray leakage, as shown in Fig. 11F. Compared to conventional structures, the cascade configuration maintains the same signal current generated by electron–hole pairs during X-ray irradiation while exhibiting lower and more stable dark current, thereby achieving a higher SNR and an improved detection limit. Moreover, the cascade structure presents an effective strategy for noise reduction in lead-based perovskites, which are prone to ion migration and unsuitable for high-bias operation.[241]

The low-temperature growth of SC perovskites makes them compatible with complementary metal-oxide-semiconductor (CMOS) readout circuits, offering potential for integration into sensitive 2D X-ray detector arrays. Although the first 2D X-ray detector arrays were made from polycrystalline perovskite films.[245] SC $MAPbBr_3$ can be grown from solution at low temperatures (below 120 °C), making it compatible with CMOS readout circuits. Wei *et al.*[246] introduced a small-molecule interfacial layer of (3-aminopropyl)triethoxysilane, which possesses NH_3Br terminal groups on one end and Si–O bonding functionalities. This dual functionality facilitates both mechanical and electrical integration of SC $MAPbBr_3$ with substrates. Moreover, the molecular dipole formed at the perovskite/Si interface serves to suppress noise current without compromising signal current, thereby enabling device operation under a higher optimal bias of −7 V. Consequently, the resulting devices exhibit large photoconductive gains, yielding a high sensitivity

of 2.1 × 104 μC Gy^{-1} cm^{-2} at 8 keV soft X-rays, which outperforms conventional amorphous selenium (α-Se) detectors.

5.4 Ionizing radiation detectors

Ionizing radiation detectors have specific performance requirements, limiting the range of suitable materials. An ideal detector is typically expected to meet the following standards:[91,232,247,248] (1) high resistivity (10^9 Ω cm) and low leakage current are essential for minimizing noise under an applied electric field, requiring the high-resistivity materials (bandgap >1.5 eV) or materials with a low intrinsic carrier concentration. (2) The optimal concentration of electrons and holes is crucial for facilitating efficient charge transport and collection, which contributes to a high SNR. (3) To enhance device sensitivity, the material is required a high-*Z* composition or a large interaction volume, maximizing interactions between incident photons and the detector medium. (4) Charge collection efficiency is determined by carrier mobility and lifetime (the $\mu\tau$ product), which are essential for allowing enough generated charge carriers to reach the electrodes for effective collection. (5) High-purity, uniform, and defect-free materials are important to achieve superior charge transport performance, maintain low leakage current, and prevent short circuits between the detector and integrated electrodes. In addition, materials should be selected to minimize polarization effects. (6) It is also essential for the materials to maintain high resistance over time to prevent surface leakage current degradation that could reduce device performance throughout its operational process.

Because no single-component material can fulfill all the requirements for an ideal ionizing radiation detector, numerous studies have investigated alternative materials that more closely approach these standards. Currently, most commercial X-ray detectors are based on cadmium telluride (CdTe), cadmium zinc telluride ($Cd_{1-x}Zn_xTe$, CZT), and amorphous selenium (α-Se). Among them, α-Se exhibits a stopping power more than ten times greater than that of silicon in the hard X-ray range,[249,250] making it the most widely used semiconductor for direct-conversion X-ray imaging and a market leader for decades.[251] Although α-Se itself is inexpensive (0.8 USD per gram), the main cost in fabricating flat-panel detectors arises from the thick-film deposition process, which typically involves vacuum thermal evaporation. CZT, a solid solution with $x < 20\%$, offers high sensitivity and has emerged as a promising candidate for advanced X-ray detectors. However, the growth of high-quality CZT single crystals requires high processing temperatures, and their integration with readout electronics remains technically challenging. Building on their success in photovoltaic applications, halide perovskites have recently attracted significant attention for X-ray detection. Their high X-ray absorption coefficients, tunable bandgap, high charge carrier mobility, and long carrier lifetimes make them promising for efficient radiation detection. A comparative summary of key performance metrics for commercial semiconductors and representative perovskite single crystals is presented in Table S2 (SI).

5.4.1 Lead-based SC perovskite detectors. 3D metal halide perovskites have emerged as promising candidates for high-energy radiation spectrum detectors, particularly MA/FA/$CsPbX_3$ (methylammonium (MA), formamidinium (FA), and cesium (Cs)-based perovskites). Table 3 provides a summary of the X-ray detection sensitivity and detection limit of recently reported lead-based SC perovskite detectors. Huang *et al.*[22] developed highly sensitive SC $MAPbBr_3$ X-ray detectors by reducing bulk defects and passivating surface defects. It achieved a high $\mu\tau$ value of 1.2×10^{-2} cm^{-2} V^{-1} and a low surface charge recombination rate of 64 cm s^{-1}. For 50 keV X-ray radiation, a 2–3 mm thick SC device exhibited a detection efficiency of 16.4% at near-zero bias, with a minimum detection limit of 0.5 μGy_{air} s^{-1} and a sensitivity of 80 μC Gy_{air}^{-1} cm^{-2}, which is four times higher than that of the α-Se detector, enabling the reduced radiation exposure in medical imaging. Liu group[254] introduced MA, Cs, and Br into SC $FAPbI_3$, achieving a remarkable sensitivity of 3.5×10^6 μC Gy_{air}^{-1} cm^{-2} for X-ray detection. Huang *et al.*[238] reported $DMAMAPbI_3$ (DMA = dimethylammonium) single crystal with the lowest detection limit of 16.9 nGy_{air} s^{-1} and a sensitivity of 2.3×10^4 μC Gy_{air}^{-1} cm^{-2}. Chu *et al.*[255] demonstrated a black α-phase SC $FAPbI_3$ through lattice engineering, as illustrated in Fig. 12A, which exhibited a low detection limit of 1.1 nGy_{air} s^{-1} and high spatial resolution of 15.9 lp mm^{-1}. Sakhatskyi *et al.*[240] reported single-photon counting and long-term operational stability in SC $MAPbI_3$ X-ray detectors operating in photovoltaic mode at zero bias voltage, as depicted in Fig. 12B and C, demonstrating over one year of operational stability, a detection efficiency of 88%, and a noise-equivalent dose of 90 pGy_{air} under 18 keV X-rays. Besides, the corresponding array detectors achieved a high spatial resolution of up to 11 lp mm^{-1}. Liu *et al.*[253] developed $Cs_{0.02}FA_{0.2}MA_{0.78}PbI_3$ thin monocrystals, which exhibited a high $\mu\tau$ product of 2.53×10^{-3} cm^2 V^{-1} and a long carrier diffusion length of 82.7 μm, enabling a self-powered detector for X-ray imaging with an impressive sensitivity of 1.74×10^5 μC Gy^{-1} cm^{-2} and an ultra-low detection limit of 11.8 nGy s^{-1} at zero bias (Fig. 12D).

Jiang *et al.*[256] reported a high-performance SC CsFAGA-alloyed (guanidinium (GA)) perovskite X-ray detectors with excellent stability, showing a high sensitivity of $(2.6 \pm 0.1) \times 10^4$ μC Gy_{air}^{-1} cm^{-2} under 1 V cm^{-1} and an ultralow limit of detection of 7.09 nGy_{air} s^{-1} (Fig. 13A and B). In addition, the resulting detectors exhibited long-term operational stability exceeding six months and remarkable thermal stability up to 125 °C. Zhao *et al.*[257] demonstrated centimeter-sized $FACsPbBr_3$ single crystals in Fig. 13C, where the introduction of formamidinium into $CsPbBr_3$ reduced defect density by eliminating phase transitions during the cooling process from growth temperature to room temperature. The as-prepared $FACsPbBr_3$ exhibited a high resistivity of 9.5×10^9 Ω cm, balanced $\mu\tau$ product values of $(2.2–3.2) \times 10^{-3}$ cm^2 V^{-1}, and a low deep trap density of 5.6×10^{10} cm^{-3}, achieving a charge collection efficiency of 84% under gamma-ray exposure. Moreover, SC $FACsPbBr_3$ showed excellent stability under high bias voltages of up to 1000 V, with no degradation in spectrum performance after seven months.

Klepov *et al.*[258] developed spectrometer-grade $CsPbBr_3$ detectors *via* a laser scribing method, exhibiting a low lateral

Table 3 X-ray detection sensitivity and detection limit comparison with the reported lead-based perovskite devices under different electric fields

Materials	Sensitivity ($\mu C\ Gy_{air}^{-1}\ cm^{-2}$)	Detection limit ($nGy\ s^{-1}$)	Peak energy (keV)	Electric field ($V\ mm^{-1}$)	Ref.
$MAPbI_3/MAPbBr_3$	8×10^3	50	60	5	244
$(BA)_2MAPb_2Br_7/MAPbBr_3$	1×10^4	40	40	0	54
$EPZPbBr_4$	1.24×10^3	5.3	50	10	261
$MAPbBr_3$	1.37×10^2	100	40	2	241
$Cs_{0.02}FA_{0.2}MA_{0.78}PbI_3$	1.74×10^4	11.8	8	0	253
$MAPbBr_3$	2.45×10^4	54	100	20	76
$CsPbBr_3$	4.61×10^4	10.81	120	500	259
$MhyPbBr_3$	220	203	50	0	268
$(S\text{-}BPEA)_2FAPb_2I_7$	87.8	161	50	0	269
$(DGA)PbI_4$	4.87×10^3	95.4	40	200	260
$[Cu(O_2C\text{-}(CH_2)_3\text{-}NH_3)_2]PbBr_4$	1.14×10^5	56	120	175	270
$MAPbBr_3$	114.4	2.52×10^4	40	−5	271
$FAPbI_3$	4.15×10^5	1.1	40	10	255
$MAPbBr_3/MAPbCl_3$	868	15.5	50	0	272
$(3AP)PbX_4$	791.8	1.54×10^3	40	50	273
$MAPbBr_{3-n}Cl_n/CsPbBr_3$	2×10^5	96	120	−125	274
$CsPbBr_3$	9.08×10^3	103.6	50	—	275
$Cs_{0.15}FA_{0.85}PbI_3/Cs_{0.15}FA_{0.85}Pb(I_{0.15}Br_{0.85})_3$	1.98×10^3	32.2	40	−25	276
$MAPbBr_3/Bi^{3+}$ doped $MAPbCl_3$	1.72×10^3	—	50	31.5	277
$FA_{0.85}MA_{0.1}Cs_{0.05}PbI_{2.55}Br_{0.45}$	3.5×10^6	42	40	−75	254
$MAPbI_3$	—	0.09	60	—	278
$FPEA_2PbBr_4/FAPbBr_3$	—	55	120	10	266
$MAPbBr_3$	632	—	50	−5	279
$MAPbBr_3$	259.9	—	39	0.83	280
$MAPbI_3$	7×10^5	—	50	100	100
$BDAPbI_4$	242	430	40	3.1	237
$(F\text{-}PEA)_2PbI_4$	3.40×10^3	23	120	200	179
$MAPbBr_3$	3.93×10^3	8.8×10^3	120	—	78
$MA_xCs_{1-x}PbBr_3$	2.01×10^3	1.2×10^3	50	1	281

Note: (EPZ, 1-ethylpiperazine), (Mhy, methylhydrazine), (S-BPEA, (*S*)-1-4-bromophenylethylammonium), (DGA, dimethylbiguanide), (3AP, 3-amidinopyridine), (FPEA, 4-fluorophenethylammonium), (BDA, $NH_3C_4H_8NH_3$), and (F-PEA, fluorophenethylammonium).

leakage current of 60 nA at 10 V and a high $\mu\tau$ product of $9.7(3) \times 10^{-4}\ cm^2\ V^{-1}$ between the pixel and the guard ring. The 122 keV and 136 keV photopeaks in the ^{57}Co (cobalt-57) gamma-ray spectrum were also well resolved with an energy resolution of up to 6.1% at 122 keV (Fig. 13D and E). Hua *et al.*[259] reported an atmosphere-controlled edge-defined film-fed growth (EFG) method to produce high-quality and shape-controlled SC $CsPbBr_3$ in an Ar (Argon) and HBr (hydrogen bromide) mixed atmosphere. The as-synthesized SC $CsPbBr_3$ exhibited a low trap density, a high resistivity of $1.61 \times 10^{10}\ \Omega$ cm, and a large ion migration activation energy of 0.378 eV, with reduced leakage current and baseline drift. As shown in Fig. 13F and G, the SC $CsPbBr_3$ X-ray detector demonstrated outstanding balanced performance, including a negligible dark-current drift of $1.68 \times 10^{-9}\ \mu A\ cm^{-1}\ s^{-1}\ V^{-1}$, a low detection limit of 10.81 $nGy_{air}\ s^{-1}$, and a sensitivity of 46 180 $\mu C\ Gy_{air}^{-1}\ cm^{-2}$ under an applied electric field of 5000 $V\ cm^{-1}$.

Replacing MA^+, FA^+, Cs^+ in 3D metal halide perovskites with larger organic cations has resulted in the development of low-dimensional perovskites, where inorganic metal halide octahedra are arranged in 2D layers, 1D chains, or 0D isolated clusters. These low-dimensional perovskites exhibit different optoelectronic properties compared to their 3D counterparts, due to quantum confinement effects and large exciton binding energies.[262] Wei *et al.*[179] reported a fluorine-containing phenylethylamine lead iodide ($(F\text{-}PEA)_2PbI_4$) SC detector, which demonstrated exceptional sensitivity to hard X-rays in the 80–120 keV range in Fig. 14A and B.

The SC $(F\text{-}PEA)_2PbI_4$ detector showed a high bulk resistivity of $1.36 \times 10^{12}\ \Omega$ cm with reduced device noise, and under a high voltage of 200 V, it maintained low ion migration, achieving a sensitivity of 3402 $\mu C\ Gy_{air}^{-1}\ cm^{-2}$, and a detectable X-ray dose rate of 23 $nGy_{air}\ s^{-1}$, with excellent stability under high-flux X-ray irradiation. Shen *et al.*[237] developed a centimeter-sized SC $BDAPbI_4$ ($NH_3C_4H_8NH_3$, BDA) perovskite, as shown in Fig. 14C and D, which exhibited a staggered configuration of $[PbI_6]_4^-$ layers, a bandgap of 2.37 eV, and a low trap density of $3.1 \times 10^9\ cm^{-3}$. The SC $BDAPbI_4$ X-ray detector demonstrated high charge transport performance with a sensitivity of 242 $\mu C\ Gy_{air}^{-1}\ cm^{-2}$, a low detection limit of 430 $nGy_{air}\ s^{-1}$, rapid response times of τ_{rise} = 7.3 ms and τ_{fall} = 22.5 ms, and a low dark current drift of $6.06 \times 10^{-9}\ nA\ cm^{-1}\ s^{-1}\ V^{-1}$. Zhang *et al.*[260] further developed 2D Dion–Jacobson (DJ) perovskite single crystals, $(DGA)PbI_4$ (dimethylbiguanide, DGA) in Fig. 14E and F, where atomic-scale analysis revealed that minimal lattice distortion and enhanced hydrogen bonding strengthened lattice rigidity, reduced electron–phonon coupling, and suppressed carrier scattering.

These improvements enhanced carrier transport and stability, resulting in a high carrier mobility of 78.1 $cm^2\ V^{-1}\ s^{-1}$ and an improved sensitivity of 4869.0 $\mu C\ Gy_{air}^{-1}\ cm^{-2}$, the highest reported for 2D Pb-based perovskite X-ray detectors. In addition, the $(DGA)PbI_4$-based detectors exhibited high spatial resolution for X-ray imaging and excellent long-term stability, making them as promising candidates for medical diagnostics and nondestructive testing. Xia *et al.*[261] reported a ⟨110⟩-

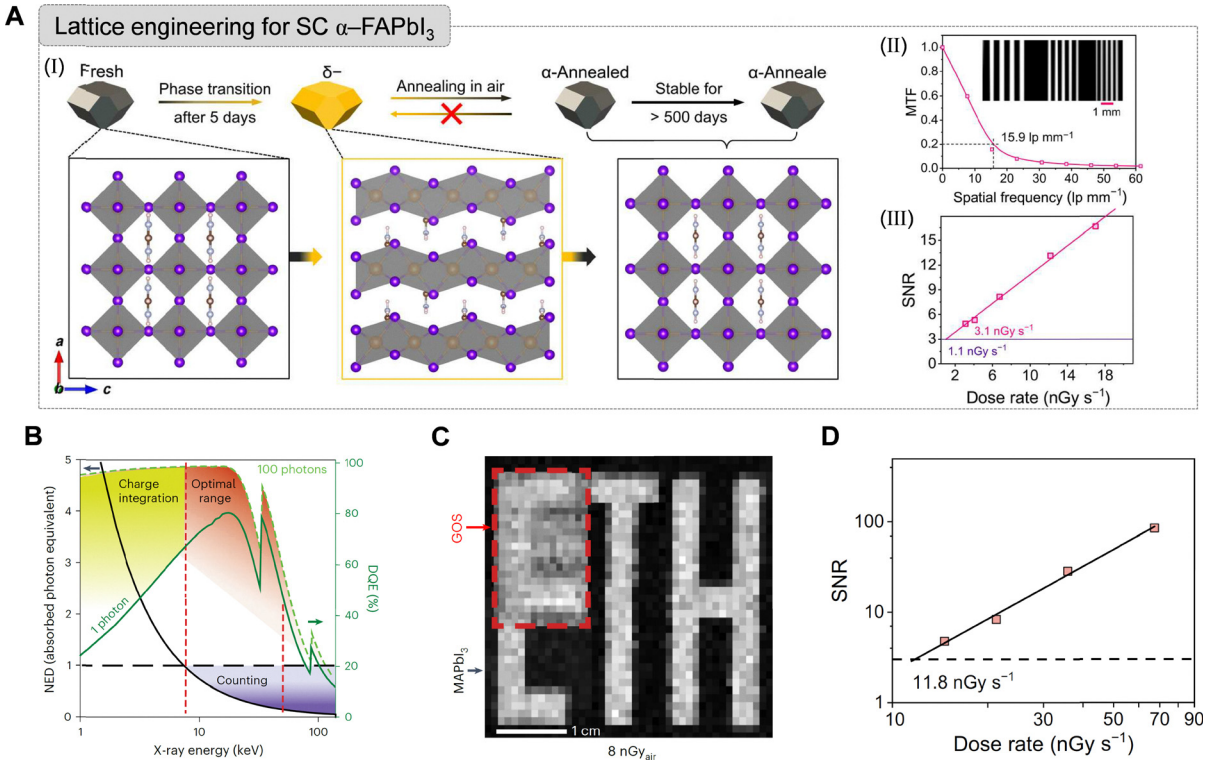

Fig. 12 (A) Lattice engineering for SC α-$FAPbI_3$. (I) Crystal structure transition of SC $FAPbI_3$ from α phase to δ phase and then to α phase. (II) Spatial frequency-dependent modulation transfer function of the annealed SC $FAPbI_3$ detector. Inset: Response current image obtained from the detector for a standard line pair card. (III) SNR of the annealed SC $FAPbI_3$ detector as a function of dose rate. The horizontal line indicates the SNR of 3. Reproduced with permission from ref. 252, Copyright 2023, The American Association for the Advancement of Science. (B) Noise-equivalent dose) (black line) and detective quantum efficiency (green lines) *versus* photon energy of $MAPbI_3$ detector. (C) X-ray imaging of a stencil mask at doses of 8 nGy_{air} of $MAPbI_3$ detector. Reproduced with permission from ref. 240, Copyright 2023, Springer Nature. (D) SNR dependence on X-ray dose rate for the self-driven high-flux-grown thin monocrystal device. Reproduced with permission from ref. 253, Copyright 2024, Springer Nature.

oriented 2D perovskite $EPZPbBr_4$ (1-ethylpiperazine, EPZ), which facilitated carrier transport by reducing the effective interlayer distance to 2.22 Å. The as-prepared SC $EPZPbBr_4$ has a high $\mu\tau$ product of 1.8×10^{-3} cm^2 V^{-1} and a large resistivity of 2.17×10^{10} Ω cm, while the assembled X-ray detector exhibited a high sensitivity of 1240 μC Gy^{-1} cm^{-2} (Fig. 14G and H).

However, most low-dimensional materials require a high supply voltage for efficient charge collection, whereas 3D SC perovskite detectors suffer from undesired ion migration and unstable current values. To overcome these challenges, recent advancements in hybrid perovskites have focused on integrating 2D layered perovskites with 3D perovskites, forming 2D/3D hetero-dimensional structures. This approach combines the superior stability of 2D perovskites with the excellent optoelectronic properties of 3D bulk perovskites, resulting in highly sensitive X-ray detectors capable of operating under low voltage bias.[263–265]

He *et al.*[266] designed novel 3D/2D $FAPbBr_3/(FPEA)_2PbBr_4$ perovskite heterojunctions (4-fluorophenethylammonium, FPEA) *via* a solution epitaxial method, which exhibited a higher $\mu\tau$ product and a lower detectable X-ray dose rate of 55 nGy_{air} s^{-1} (Fig. 15A and B), demonstrating great potential for low-dose hard X-ray detection and imaging. As shown in Fig. 15C and D, Zhang *et al.*[267] reported self-powered X-ray detectors based on well-oriented 2D/3D 4-AMPY)$(MA)_3Pb_4I_{13}/MAPbBr_3$ perovskite crystals (4-(aminomethyl)pyridinium, 4-AMPY), using a halide diffusion-promoted welding approach to construct two distinct configurations: a lateral orientation with perpendicular inorganic frameworks and a vertical orientation with parallel inorganic slabs. The anisotropic X-ray detection performance, characterized by an anisotropic ratio of 4, resulted from the different crystalline orientations of the self-powered X-ray detector featuring a vertical structure, which exhibited a suppressed dark current density of 0.17 nA cm^{-2}, a high sensitivity of 1850 μC Gy_{air}^{-1} cm^{-2}, and an ultra-low detection limit of 77 nGy_{air} s^{-1} at zero bias. Zhang *et al.*[54] further developed 2D/3D $(BA)_2MAPb_2Br_7/MAPbBr_3$ (*n*-butylammonium, BA) core–shell heterocrystals with well-defined interfaces and controlled shell thickness. The core–shell heterocrystal X-ray detectors showed excellent high-resolution X-ray imaging, an ultra-low dark current drift of 1.1×10^{-7} nA cm^{-1} s^{-1} V^{-1}—five orders of magnitude lower than that of 3D perovskite devices—along with a high sensitivity of 1×10^4 μC Gy_{air}^{-1} cm^{-2} and a low detection limit of 40 nGy_{air} s^{-1} (Fig. 15E and F).

5.4.2 Lead-free SC perovskite detectors. (a) SC bismuth (Bi)-based detector

Bismuth (Bi), due to its high atomic number and strong X-ray absorption, presents great potential for direct X-ray detection.

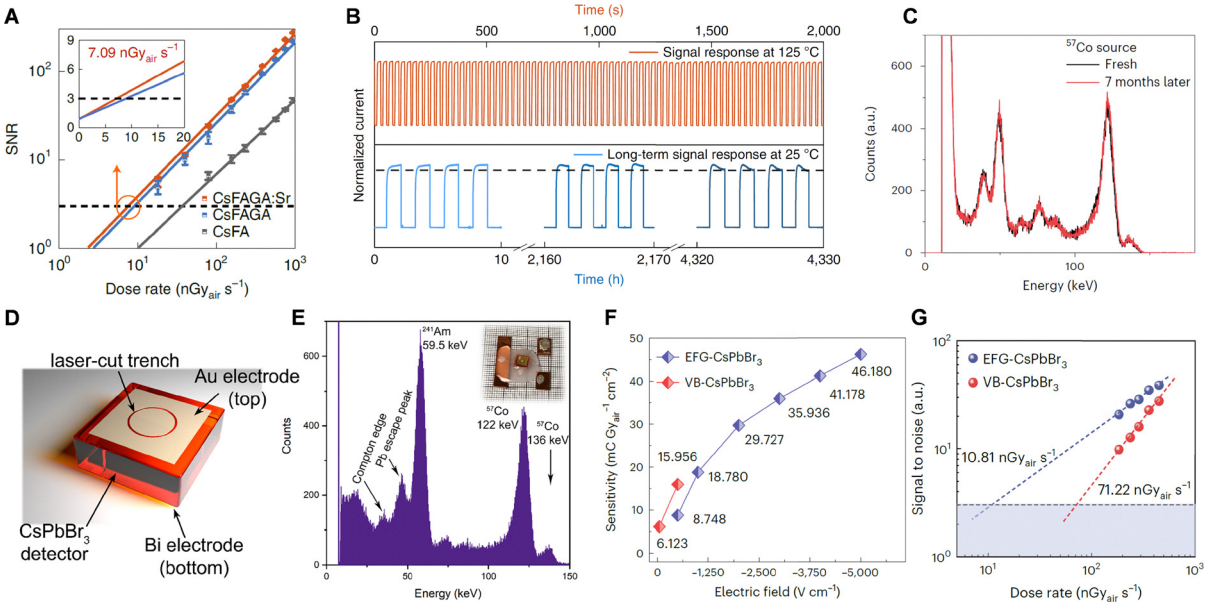

Fig. 13 (A) SNR dependent on the X-ray dose rate for the CsFA, CsFAGA and CsFAGA: Sr detectors. (B) Long-term operational and thermal stability of an unencapsulated CsFAGA: Sr detector. All the tests were carried out at 1 V cm^{-1}. Reproduced with permission from ref. 256, Copyright 2022, Springer Nature. (C) Spectrum collected from the fresh and aged (after seven months of storage) FACsPbBr$_3$ device. Reproduced with permission from ref. 257, Copyright 2023, Springer Nature. (D) Schematic view of laser-cut single-pixel CsPbBr$_3$ detector device. (E) ^{241}Am and ^{57}Co combined spectrum measured from the CsPbBr$_3$ device at −300 V bias voltage, 10 μs shaping time, and 300 s collection time (inset shows the measured wired device). The energy resolution is 11.4% and 6.1% for the 59.5 keV and 122 keV peaks, respectively. Reproduced with permission from ref. 258, Copyright 2023, American Chemical Society. (F) Sensitivities of atmosphere-controlled edge-defined film-fed growth (EFG-) and vertical Bridgman (VB-) SC CsPbBr$_3$ detectors measured for bias voltages ranging from 50 to −5000 V cm^{-1} for 120-keV hard X-rays. (G) Detection limits were extracted from the fitting line at an SNR of 3. Reproduced with permission from ref. 259, Copyright 2024, Springer Nature.

Among Bi-based materials, double halide perovskites, including $Cs_2AgBiBr_6$ and low-dimensional Bi-based perovskite are the two representative material families for this application.[242] In 2017, Pan *et al.*[112] reported the synthesis of SC $Cs_2AgBiBr_6$ by substituting Pb with Ag and Bi for direct X-ray detection. Theoretical calculations indicated that the high atomic number of these elements could enhance detection performance, while experimental results confirmed a low ion migration ability.

The SC $Cs_2AgBiBr_6$ exhibited an indirect bandgap, a long carrier diffusion length, and suppressed surface defects, while the as-prepared device demonstrated a sensitivity of 105 μC Gy_{air}^{-1} cm^{-2} at an electric field of 25 V mm^{-1}, a detection limit of 59.7 nGy$_{air}$ s^{-1} (Fig. 16A), and excellent stability under high temperature and radiation exposure. After that, the Bi^{3+}–Ag^{+} system has been widely investigated for X-ray detection applications. Xu *et al.*[282] introduced a 2D multilayered $(BA)_2CsAgBiBr_7$ (Fig. 16B), which has a high $\mu\tau$ product of 1.21×10^{-3} cm^2 V^{-1}, a high bulk resistivity of 1.5×10^{11} Ω cm, and a low defect density of 4.2×10^{10} cm^{-3}. However, due to less efficient charge transport in the out-of-plane direction compared to 3D halide perovskites, the device achieved a sensitivity of 4.2 μC Gy_{air}^{-1} cm^{-2}. Zhang *et al.*[283] reported a solution-processed *in situ* heteroepitaxial approach for constructing the lead-free halide perovskite $(BA)_2CsAgBiBr_7/Cs_2AgBiBr_6$ heterojunction (Fig. 16C), which exhibited near-atomically sharp interfaces and enabled self-powered operation due to its built-in electric potential. The resulting device demonstrated a dark current (3.2×10^{-2} pA) (Fig. 16D), a photocurrent of 240 pA, and an on/off switching ratio of 10^4, achieving a sensitivity of 206 μC Gy_{air}^{-1} cm^{-2} under zero bias.

Low-dimensional Bi-based single crystals hold significant research value due to their low ion migration energy, which can enhance detection stability. Zhuang *et al.*[74] reported a high-density and wide-bandgap 2D layered $(NH_4)_3Bi_2I_9$ perovskite exhibiting notable anisotropic X-ray responses with the parallel-oriented device achieving a sensitivity of 8.2×103 μC Gy_{air}^{-1} cm^{-2} and the perpendicular-oriented device showing a low detection limit of 55 nGy$_{air}$ s^{-1}, as illustrated in Fig. 16E and F. These results suggest that 2D layered perovskite-like semiconductors could serve as non-toxic alternatives to traditional 3D perovskites, enabling highly sensitive X-ray detection with a low detection limit. Liu *et al.*[119] synthesized inch-sized and high-quality 0D SC $MA_3Bi_2I_9$ with minimal ion migration by slowly elevating the temperature of the precursor solution from 65 °C to 105 °C, achieving a sensitivity of 1947 μC Gy_{air}^{-1} cm^{-2} and a detection limit of 83 nGy$_{air}$ s^{-1} under 60 V mm^{-1}. Zhang *et al.*[284] further introduced a nucleation-controlled method to grow centimeter-sized $Cs_3Bi_2I_9$ perovskite single crystals, which exhibited low trap-state densities, high $\mu\tau$ products, and low dark current noise, resulting in a X-ray sensitivity of 1652.3 μC Gy_{air}^{-1} cm^{-2} and a detectable dose rate 130 nGy$_{air}$ s^{-1} (Fig. 16G). In addition, the suppressed ion migration contributed to exceptional device stability, with over 13 hours of continuous operation and superior X-ray imaging capabilities. The remarkable thermal stability of low-dimensional Bi-based

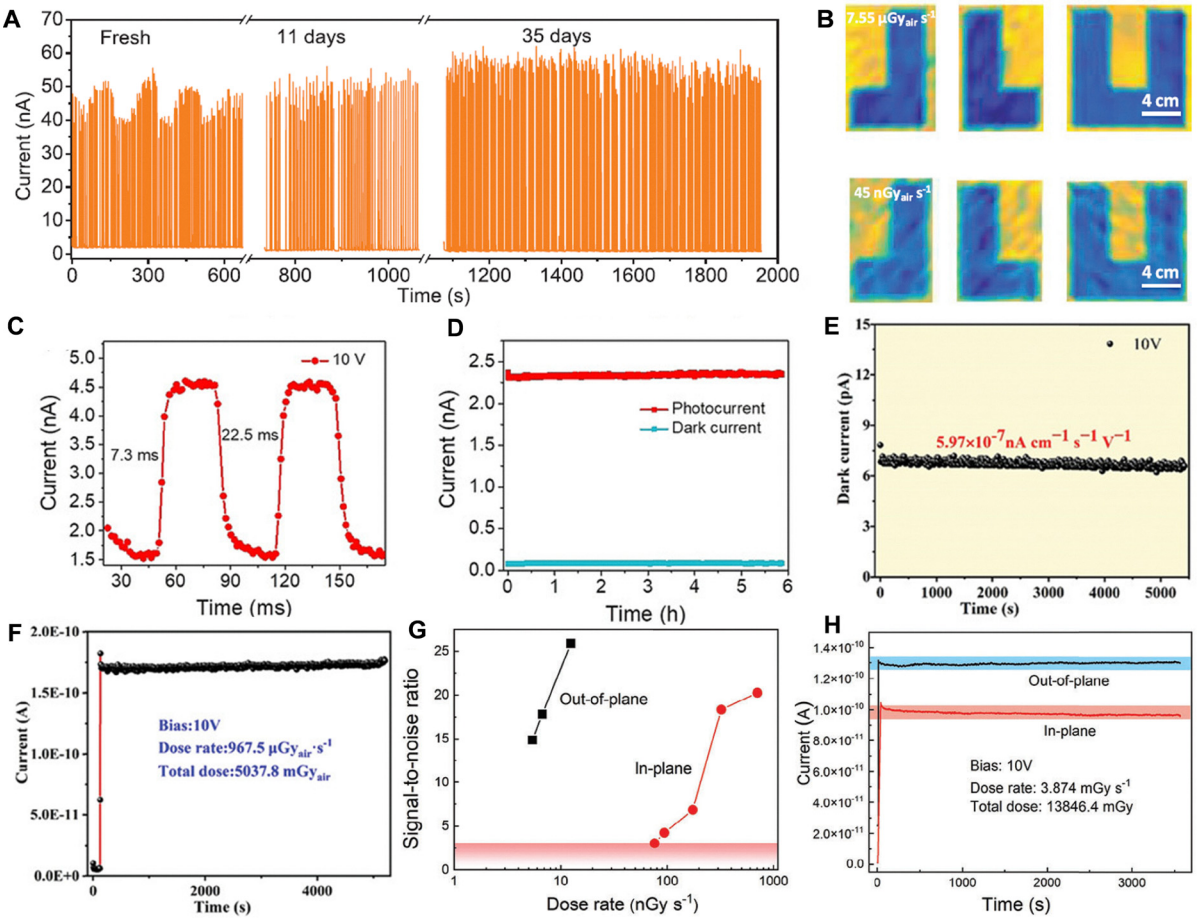

Fig. 14 (A) Long-term operation stability tests of (F-PEA)$_2$PbI$_4$ detector in response to X-ray pulses, and the devices are stored for 0 day, 11 days, and 35 days before testing. (B) The X-ray images of "JLU" metal plates obtained by the (F-PEA)$_2$PbI$_4$ single crystal X-ray detector under after 3 mm thick Pb plate attenuation, under radiation levels of 7.55 nGy$_{air}$ s^{-1} and 45 nGy$_{air}$ s^{-1}, respectively. Reproduced with permission from ref. 179, Copyright 2020, Wiley-VCH GmbH. (C) Temporal response of the (BDA)PbI$_4$ X-ray detector to X-rays. (D) Photocurrent and dark current stability measurement of a (BDA)PbI$_4$ X-ray detector (photocurrent was collected under continuous X-ray irradiation with a constant 10 V bias). Reproduced with permission from ref. 237, Copyright 2020, Wiley-VCH Verlag GmbH & Co. KGaA, Weinheim. (E) Dark current measurement for (DGA)PbI$_4$ detector current drift (200 V mm^{-1}, 967.5 μGy$_{air}$ s^{-1}). (F) Irradiation stability measured for the (DGA)PbI$_4$ detector exposed to X-rays (967.5 μGy$_{air}$ s^{-1}) at 200 V mm^{-1} electric field. Reproduced with permission from ref. 260, Copyright 2023, Wiley-VCH GmbH. (G) SNR of the EPZPbBr$_4$ devices. (H) Photocurrent stability of EPZPbBr$_4$ detector exposed to X-rays (3.874 mGy s^{-1}) for 1 h. Reproduced with permission from ref. 261, Copyright 2024, Wiley-VCH GmbH.

perovskites makes them promising candidates for high-temperature X-ray detection, as their stable response reach temperatures up to 100 °C. Moreover, various A-site (MA^+, FA^+, Ag^+, GA^+) and X-site (Cl^-, Br^-, I^-) substitutions have been investigated to develop high-quality single crystals with improved imaging performance, as depicted in Fig. 16H.[285,286] Table 4 provides a summary of the X-ray detection sensitivity and detection limit of recently reported lead-free perovskite detectors.

(b) SC metal-free perovskite detector

Large divalent organic molecules, such as $DABCO^{2+}$ (*N*-*N*′-diazabicyclo[2.2.2]octonium) and MDBACO (methyl-*N*′-diazabicyclo[2.2.2]octonium), have been introduced into perovskites to replace Pb^{2+}, forming a hydrogen-bonded and intermolecularly connected structural framework known as molecular perovskites or metal-free perovskites.[121,122,287–289] Song *et al.*[121] reported the large-sized DABCO-NH_4Br_3 single crystals and developed an X-ray detector that had a sensitivity of 173 μC Gy$_{air}^{-1}$ cm^{-2} at 50 V bias and a detection limit of 4.96 μGy$_{air}$ s^{-1} at10 V bias. Then, Cui *et al.*[122] synthesized $DABCONH_4X_3$ (X = Cl, Br, I) single crystals and observed that, under the same voltage, the DABCO-NH_4I_3 SC detector achieved a high sensitivity of 567 μC Gy$_{air}^{-1}$ cm^{-2} along with high-quality imaging results, as illustrated in Fig. 17A–D. Structural tuning at the A-site and B-site led to the development of MDABCO-NH_4I_3 single crystals in 2021, where $DABCO^{2+}$ was replaced with $MDABCO^{2+}$, improving device performance and yielding a sensitivity of 1997 μC Gy$_{air}^{-1}$ cm^{-2} (Fig. 17E).[288] Additionally, SC DABCO-$N_2H_5Br_3$ was synthesized by replacing NH_4^+ with $N_2H_5^+$, achieving dimensional regulation and enhancing device stability, with a sensitivity of 1143 μC Gy$_{air}^{-1}$ cm^{-2} and an ultra-low detection limit of 2.68 μGy s^{-1} at 10 V bias. The reduced-dimensionality structure further contributed to enhanced current stability (Fig. 17F), making the metal-free perovskites highly promising for next-generation X-ray detectors.[290]

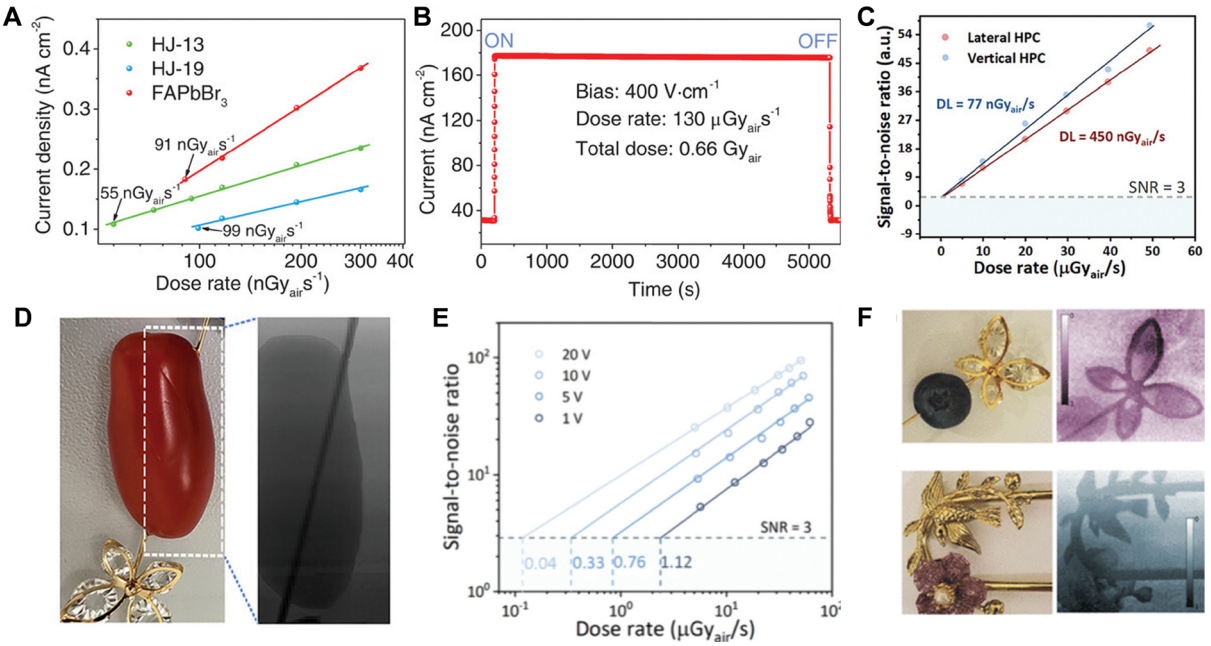

Fig. 15 (A) Current density of HJ-13, HJ-19, and $FAPbBr_3$ single crystal devices at different X-ray dose rates, respectively. (B) The long-term operation stability tests of $FAPbBr_3/(FPEA)_2PbBr_4$ detector in response to X-ray. Reproduced with permission from ref. 266, Copyright 2021, Wiley-VCH GmbH. (C) Detection limit of the lateral and vertical 4-AMPY)$(MA)_3Pb_4I_{13}$/$MAPbBr_3$ devices under self-powered mode. (D) X-ray image of a tomato with a needle stuck in it. Reproduced with permission from ref. 267, Copyright 2023, Wiley-VCH GmbH. (E) Detection limit of the $(BA)_2MAPb_2Br_7/MAPbBr_3$ X-ray detectors at different bias voltages. (F) X-ray image of a blue berry with a needle stuck in it and a metal hairpin. Reproduced with permission from ref. 54, Copyright 2024, American Chemical Society.

Lead-free SC perovskites avoid the use of the toxic lead, which is especially important for biocompatible applications. Moreover, some of lead-free SC perovskites exhibit excellent structural stability, making them suitable for long-term operation in detection systems or extreme environments such as outer space. However, they still lag behind mainstream lead-based perovskites (*e.g.*, $MAPbBr_3$, $MAPbI_3$, and $FAPbI_3$) in key parameters, including carrier mobility-lifetime product ($\mu\tau$), energy resolution, and dark current suppression and remain at an early stage of research. With further advancements in material optimization, device engineering, and structural design, their potential for safe and environmentally friendly applications in medical imaging and space exploration can be achieved.

6. Challenges and perspective

SC perovskites have emerged as promising candidates for advanced optoelectronic applications, including photovoltaics and radiation detection, owing to their superior optoelectronic properties. Despite substantial progress, several challenges remain, particularly in the scalable fabrication of large-area SC thin films, long-term operational stability, and flexible device integration. Therefore, a holistic approach that combines high-quality crystal growth, device architecture optimization, and defect passivation is essential to address these challenges, enhance the performance of SC perovskite-based optoelectronic devices, and accelerate their path toward commercialization.

6.1 Scalable fabrication

The fabrication of large-area SC perovskite thin films presents a major challenge, hindering the progress of SC perovskite-based applications. Despite various bulk SC perovskite growth methods, including slow cooling, inverse-temperature crystallization, anti-solvent approach, and solvent evaporation, enabling the growth of bulk SC perovskites at the centimeter scale, several issues remain in their practical applications: (1) due to the excessive thickness of SC perovskites, they cannot be directly used to fabricate vertical-structure PSCs. (2) The random growth of centimeter-scale bulk SC perovskites fails to meet the demands of lightweight and flexible optoelectronic devices. (3) The growth process for bulk SC perovskites is time-consuming and requires substantial raw materials. (4) Achieving uniform sizes for bulk SC perovskites is also challenging, rendering them unsuitable for large-scale applications. In addition, the space-limited ITC method—commonly used technique for fabricating SC perovskite thin films—suffers from inherent limitations, including residual solvents and inferior mechanical adhesion at the perovskite–substrate interface, which degrade electrical contacts and constrain device performance. It also remains difficult with this approach to grow centimeter scale or larger SC thin films.

Inspired by traditional silicon-based semiconductor slicing technologies, early-stage studies on slicing methods for SC perovskites have been explored but have received insufficient attention due to their suboptimal performance. SC perovskite wafers produced *via* a slicing method provide a promising

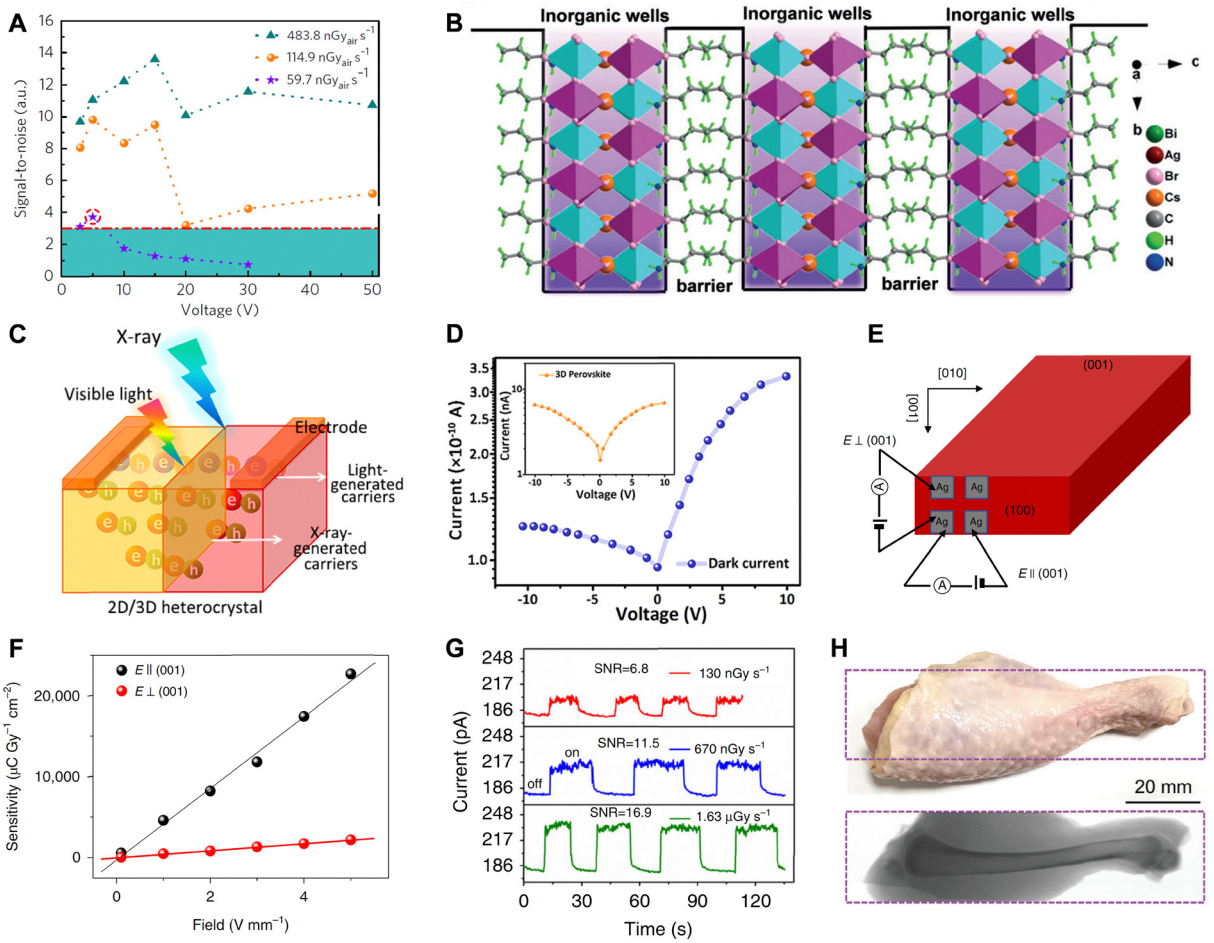

Fig. 16 (A) SNR of the $Cs_2AgBiBr_6$ device derived by calculating the standard deviation of the X-ray photocurrent. Reproduced with permission from ref. 112, Copyright 2017, Springer Nature. (B) Structural configuration of $(BA)_2CsAgBiBr_7$ that defines the 2D perovskite quantum-confined motif. Reproduced with permission from ref. 282, Copyright 2019, Wiley-VCH Verlag GmbH & Co. KGaA, Weinheim. (C) Schematic planar structure of the $(BA)_2CsAgBiBr_7$/$Cs_2AgBiBr_6$ detector. (D) *I*–*V* curves of the $(BA)_2CsAgBiBr_7$/$Cs_2AgBiBr_6$ detector measured in the dark. Reproduced with permission from ref. 283, Copyright 2021, American Chemical Society. (E) A planar-type photodetector device made on the (100) surface of $(NH_4)_3Bi_2I_9$ single crystal. (F) X-ray sensitivities of the $(NH_4)_3Bi_2I_9$ devices in directions parallel and perpendicular to the (001) surface. Reproduced with permission from ref. 74, Copyright 2019, Springer Nature. (G) X-ray photocurrent response of the $Cs_3Bi_2I_9$ PSC device under electric field of 50 V mm^{-1} when exposed to different X-ray dose rates. Reproduced with permission from ref. 284, Copyright 2020, Springer Nature. (H) Photograph of a chicken drumstick and the corresponding X-ray image measured by the 2D $MABiI_6Br_3$ SC linear array detector. Reproduced with permission from ref. 285, Copyright 2024, Wiley-VCH GmbH.

approach to address the existing issues associated with bulk SC perovskite and thin films prepared by the aforementioned methods. Therefore, it is worth investigating the fabrication methods for high-quality SC perovskite wafers, as they are crucial for developing the large-scale application of SC perovskites. The key challenges in optimizing the performance of optoelectronic devices based on SC perovskite thin films derived from bulk crystal slicing can be classified into three main aspects: (1) the mechanism of sliced defects in SC perovskites, including variations in surface energy states, the types of sliced surface defects, and the depth distribution of these defects. (2) Efficient passivation approaches tailored to the specific characteristics of the crystal-cut interfaces. (3) Suitable techniques for integrating SC perovskite wafers onto conductive glass substrates for vertical device fabrication. Addressing these challenges holds great potential for achieving significant breakthroughs in the performance of SC perovskite-based optoelectronic devices.

6.2 Long-term operational stability

Although SC perovskites exhibit lower bulk defect densities and longer charge carrier lifetimes due to their minimal grain boundaries, their stability in practical applications often falls short of expectations. The stability issues of SC perovskite-based devices primarily result from the presence of surface defects. Due to limitations related to the size and geometry morphology, traditional defect passivation techniques are less effective in addressing surface defects in SC perovskites. Therefore, developing *in situ* passivation strategies will be crucial for effective surface defect passivation. This approach requires the introduction of specific additives into SC perovskite precursors. For instance, the additive molecules should have multifunctional

Table 4 X-ray detection sensitivity and detection limit comparison with the reported lead-free perovskite devices under different electric fields

Materials	Sensitivity ($\mu C\ Gy_{air}^{-1}\ cm^{-2}$)	Detection limit ($nGy\ s^{-1}$)	Peak energy (keV)	Electric field ($V\ mm^{-1}$)	Ref.
$MA_3Bi_2I_9$	1.95×10^3	83	40	60	119
$(MA_{0.7}Cs_{0.3})_3Bi_2I_9$	130	12.8	40	128.6	291
$Cs_3Bi_2I_9$	1.65×10^3	130	40	50	284
Cs_2TeI_6	19.5	170	40	400	292
$(Cs_{0.98}Na_{0.02})_2AgBiBr_6$	1	—	70	10	293
$(Cs_{0.98}Na_{0.02})_2AgBiBr_6$	8	—	70	10	293
$((Cs_{0.98}Rb_{0.02})_2AgBiBr_6$	32	—	70	10	293
$Cs_3Bi_2Br_9$	1.71×10^3	0.58	120	1×10^3	294
$(BA)_2CsAgBiBr_7$	206	6.40×10^3	40	10	283
HMTA-NH_4Br_3	150	4.18×10^3	40	50	289
DABCO-NH_4Br_3	173	4.96×10^3	29	50	121
(DMEDA)BiI_5	72.5	7.85×10^5	50	300	295
$(4,4\text{-DFPD})_4AgSbI_8$	704.8	360	40	100	296
$(CPA)_4AgBiBr_8$	0.8	—	70	10	297
$(NH_4)_3Bi_2I_9$	8×10^3	55	22	2.2	74
$Rb_3Bi_2I_9$	159.7	8.32	50	300	298
$FA_3Bi_2I_9$	598.1	200	45	200	116
PAZE-$NH_4I_3{\cdot}H_2O$	2.13×10^3	248	20	200	299
PAZE-$NH_4Cl_3{\cdot}H_2O$	2.83×10^3	341	20	200	299
PAZE-$NH_4Br_3{\cdot}H_2O$	3.71×10^3	192	20	200	299
$MA_3Bi_2I_9$	563	9.3	35.5	210	118
$Cs_3Bi_2I_9$	4.38×10^3	7.93	35	20	300
$AG_3Bi_2I_9$	5.79×10^3	2.6	70	100	286
BTA_2MnBr_4	5.56×10^3	8.7	20	200	301
$Cs_2AgBiBr_6$ + BiOBr	250	95.3	50	500	302
$Cs_2AgBiBr_6$	105	59.7	30	25	112
$MA_3Bi_2I_9$	1.31×10^4	10.6	70	100	285
$MA_3Bi_2I_6Br_3$	2.45×10^4	4.3	70	100	285
$MA_3Bi_2I_3Br_6$	1.05×10^4	15.8	70	100	285
$((2\text{-Habch})_3Cl(PtI_6)$	1×10^5	2.4	40	−100	303
$(R\text{-MPA})_4AgBiI_8$	46.3	85	50	0	304
MPAZE-$NH_4I_3{\cdot}H_2O$	740.8	0.14	40	20	305
MDABCO-$NH_4(PF_6)_3$	2.08×10^3	16.3	40	10	306
$Cs_3Bi_2I_{9-n}Br_n$	1.33×10^4	28.64	100	1×10^3	307
$Cs_3Bi_2I_9$	2.94×10^4	0.36	40	40	131
$CsAg_2I_3$	515.49	1.47×10^4	35	15	308
$[(CH_3)_3NH]MnCl_3{\cdot}2H_2O$	295	900	40	50	309

Note: (HMTA, hexamethylenetetramine), (DABCO, *N*-*N*′-diazabicyclo[2.2.2]octonium), (DMEDA, *N*,*N*′-dimethylethanediamine), (4,4-DFPD, 4,4-difluoropiperidinium), (CPA, chloropropylammonium), (PAZE, piperazinium), (AG, aminoguanidinium) manganese bromide (BTA, benzyltrimethylammonium), (BiOBr, bismuth oxybromide), (2-Habch, *R*-2-azabicyclo[2.2.1]heptan-2-ium), (R-MPA, *R*-β-methylphenethylammonium), (MPAZE, methyl-piperazine), (MDBACO, methyl-*N*′-diazabicyclo[2.2.2]octonium).

groups that can interact with perovskite lattice to passivate vacancy, interstitial, and anti-site defects. Besides, these additive molecules do not incorporate into the perovskite lattice interior but instead bond to the crystal surface during SC perovskite growth. The *in situ* passivation approach using multifunctional additives not only promotes defect passivation but also forms a protective encapsulation layer on the perovskite surface, effectively shielding the crystals from external stressors while maintaining their structural integrity.

In addition, ion migration under operational conditions is another factor that affects the stability of SC perovskite devices, resulting from the relatively weak bonding energy between A, B, and X-site atoms in the perovskite lattice. Enhancing the bonding energy through a heteroatom doping strategy is beneficial, as it contributes to suppressed ion migration and improved structural stability of SC perovskites. In this approach density functional theory (DFT) calculation plays an important role in simulating the effects of various dopant atoms on the structural stability of the perovskite lattice, thereby optimizing the selection of dopants.

6.3 Flexible applications

Flexible devices have gained significant attention as next-generation applications in various fields, including foldable displays, biomedical imaging systems, and wearable technology.[310] Perovskite-based flexible photoelectronic devices have been developed based on polycrystalline film.[311,312] However, the inherent rigidity and fragility of SC perovskites pose challenges for their integration into flexible applications.[313] To the best of current knowledge and technologies, the development of flexible optoelectronic devices using large-area SC perovskite films remains a major challenge. Therefore, the investigation of SC perovskite array configurations presents a practical approach to enable the flexible applications. There are two mainstream strategies for references: one, as previously reported, directly grows SC perovskite arrays on a substrate, but it faces limitations in controlling crystal size, spacing, and batch-to-batch reproducibility. The other is a method that assembles as-prepared SC perovskite thin films onto flexible substrates, enabling the fabrication of large-area devices (Fig. 18). The second approach involves the preparation of SC perovskite bulk or thin films, as discussed in Section 3 of

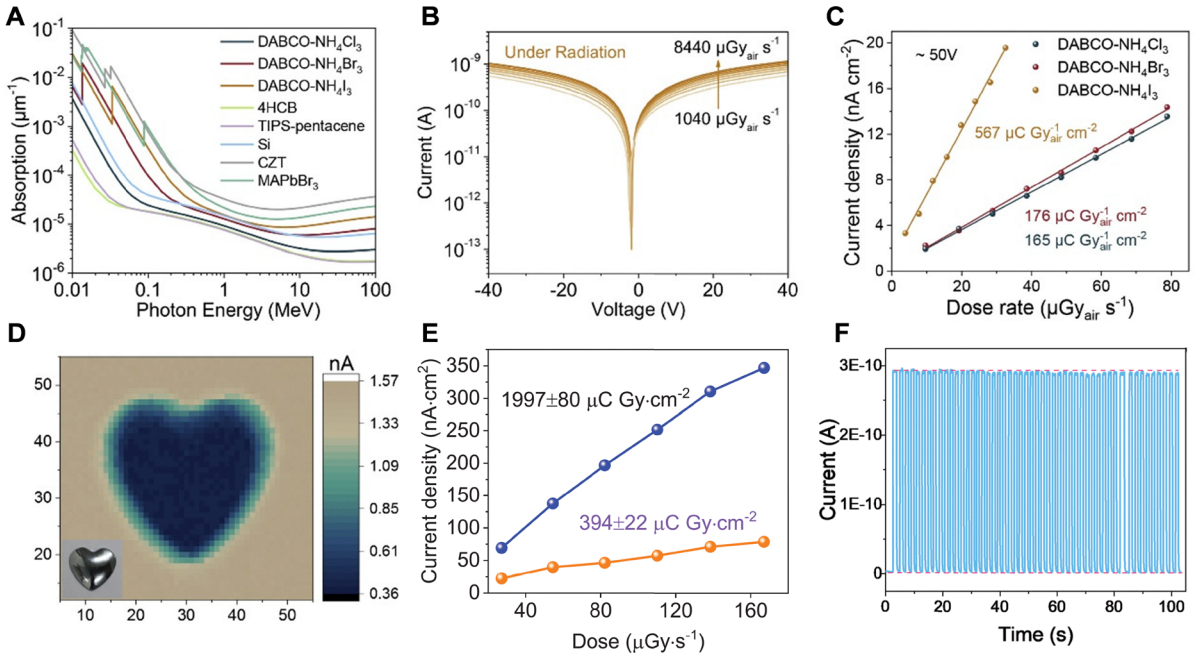

Fig. 17 (A) Absorption coefficients of DABCO-NH_4X_3, several metal-free and metal-containing materials as a function of photon energy, from soft X-rays to gamma radiation. (B) Current–voltage curves of DABCO-NH_4I_3 crystal device under different irradiation conditions. (C) X-ray photocurrents of DABCO-NH_4X_3 crystal devices under 50 V bias as a function of dose rate. (D) X-ray images realized with DABCO-NH_4I_3 SC detector. Reproduced with permission from ref. 122, Copyright 2021, Elsevier Inc. Wiley-VCH GmbH. (E) X-ray sensitivity of the MDABCO-NH_4I_3 SC detector at 50 V (upper curve) and 5 V (lower curve) bias at dose rates from 26.3 μGy s^{-1} to 167 μGy s^{-1}. (F) On–off response of the $DABCON_2H_5Br_3$ device at 5 V bias voltage for 100 s. Reproduced with permission from ref. 290, Copyright 2023, Wiley-VCH GmbH.

this review. High-quality SC perovskite thin films with uniform dimensions can be achieved through techniques such as physical slicing or chemical etching, which can be assembled into SC perovskite arrays, showing technical feasibility for practical implementation.

6.4 Emerging SC perovskite applications

While SC perovskites have achieved significant progress in photovoltaics and high-energy radiation detection due to their superior optoelectronic properties, recent advances have also highlighted their potential in ultraviolet-to-infrared photodetection,[314–316] single-photon counting,[240] and light-emitting diodes.[240,317] Beyond the scope of this review, the structural diversity and compositional tunability of SC perovskite materials offer broad potential across next-generation optoelectronic platforms. Several emerging applications are outlined as follows:

(a) Nonlinear optics and integrated photonic applications

SC perovskites possess high optical transparency across a broad spectral range and exhibit pronounced third-order optical nonlinear properties,[318,319] making them suitable for

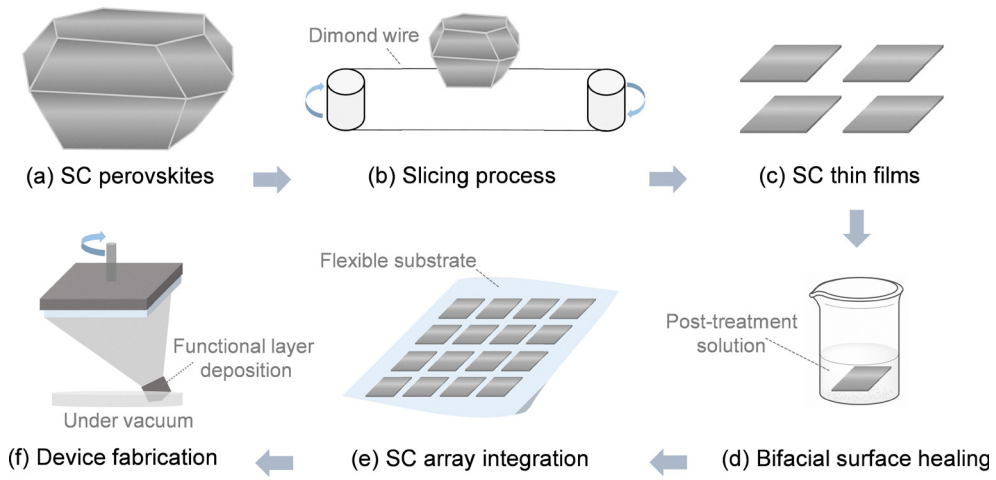

Fig. 18 Schematic illustration of the fabrication process for flexible SC perovskite devices, including (a) SC perovskite growth, (b) slicing, (c) preparation of SC thin films, (d) bifacial surface healing, (e) array integration, and (f) device fabrication.

nonlinear optical devices such as electro-optic modulators, deflectors, switches, and other components in integrated photonic systems. The large nonlinear coefficients of SC perovskites enable efficient frequency conversion and all-optical signal processing, while their ultrafast optical response and low optical losses are beneficial for high-speed modulation and signal transmission in photonic circuits. These unique properties further highlight the potential of SC perovskites for high-speed optical communication, signal processing, on-chip quantum photonics, and nonlinear optical computing platforms.[320]

(b) Artificial synaptic devices and neuromorphic applications

Synaptic devices simulate the signal transmission, collection, and processing behaviors of biological synapses by integrating photosensitive components with synaptic transistors, enabling dynamic modulation of synaptic weights in response to optical inputs. SC perovskites, with their high carrier mobility and broadband spectral (ultraviolet to infrared) photoresponse, are suitable for artificial optoelectronic synaptic devices. These intrinsic material properties fulfill essential neuromorphic requirements such as optical sensing, synaptic plasticity, and device integration, indicating that the SC perovskite-based synaptic devices hold great promise for next-generation technologies in visual pattern recognition, intelligent driving, and neuromorphic computing systems.[321]

7. Summary

In this review, we summarized the advantages of SC perovskites over their polycrystalline counterparts and investigated various methods for synthesizing and fabricating bulk crystals and thin films. We then discussed their applications in solar cells and high-energy radiation detection, highlighting the field's development trajectory, latest advancements, and existing challenges. To address these challenges, we proposed potential avenues and perspectives for improving SC perovskite fabrication and applications. Given their superior optoelectronic properties, overcoming the current limitations—particularly those related to large-area growth, thickness control, integration with device architectures, and operational stability—will be critical for enabling performance breakthroughs in SC perovskite-based optoelectronic devices and advancing the future of perovskite technologies.

Author contributions

O. M. B. and O. F. M. supervised and guided this work and the content planning. B. S. contributed to the introduction and conclusion sections. H. Z. contributed to the application sections of single-crystal perovskite solar cells and abstract. X. S. contributed to the section on high-energy detection applications of single-crystal perovskites. X. S. and H. Z. wrote the section on cutting-edge advancements. Y. A. B. prepared the single-crystal perovskite synthesis section. B. S., X. S., and W. W. wrote the challenges and perspective section. M. A. coordinated the content planning, edited the draft, and guided draft progress. H. S., S. A., and I. G. assisted with reference formatting and contributed to the discussion. All authors participated in discussions and manuscript review.

Conflicts of interest

The authors declare the following competing financial interest(s): O. M. B. is the founder of Quantum Solutions, a company that develops optoelectronic devices. The other authors declare no conflicts of interest.

Data availability

Supplementary information and summarizes the properties and key parameters of representative single-crystal perovskites and X-ray detectors used in medical imaging. See DOI: **https://doi.org/10.1039/d5cs00625b**.

No primary research results, software or code have been included and no new data were generated or analysed as part of this review.

Acknowledgements

This review article has received funding from King Abdullah University of Science and Technology (KAUST) and Saudi Aramco. B. S. acknowledges financial support from the China Scholarship Council (No. 202006070004).

References

1 Z. Yang, Q. Xu, X. Wang, J. Lu, F. Li, L. Zhang, G. Hu, C. Pan, Z. Yang, Q. Xu, X. Wang, J. Lu, G. Hu, C. Pan and H. Wang, *Adv. Mater.*, 2018, **30**, 1802110.
2 H. Zhu, F. Zhang, Y. Xiao, S. Wang and X. Li, *J. Mater. Chem. A*, 2018, **6**, 4971–4980.
3 X. Ling, H. Zhu, W. Xu, C. Liu, L. Pan, D. Ren, J. Yuan, B. W. Larson, C. Gratzel, A. R. Kirmani, O. Ouellette, A. Krishna, J. Sun, C. Zhang, Y. Li, S. M. Zakeeruddin, J. Gao, Y. Liu, J. R. Durrant, J. M. Luther, W. Ma and M. Gratzel, *Angew. Chem., Int. Ed.*, 2021, **60**, 27299–27306.
4 X. Liu, K. Yan, D. Tan, X. Liang, H. Zhang and W. Huang, *ACS Energy Lett.*, 2018, **3**, 2701–2707.
5 R. L. Milot, M. T. Klug, C. L. Davies, Z. Wang, H. J. Snaith, M. B. Johnston, L. M. Herz, R. L. Milot and H. Kraus, *Adv. Mater.*, 2018, **30**, 1804506.
6 M. Jung, S.-G. Ji, G. Kim and S. I. Seok, *Chem. Soc. Rev.*, 2019, **48**, 2011–2038.
7 H. Zhu, L. Pan, F. T. Eickemeyer, M. A. Hope, O. Ouellette, A. Q. M. Alanazi, J. Gao, T. P. Baumeler, X. Li, S. Wang, S. M. Zakeeruddin, Y. Liu, L. Emsley and M. Gratzel, *ACS Energy Lett.*, 2022, **7**, 1112–1119.
8 Y. Zhao and K. Zhu, *Chem. Soc. Rev.*, 2016, **45**, 655–689.
9 H. Li, N. Shen, S. Chen, F. Guo and B. Xu, *Adv. Funct. Mater.*, 2023, **33**, 2214339.

10 L. Mao, C. C. Stoumpos and M. G. Kanatzidis, *J. Am. Chem. Soc.*, 2018, **2019**, 1171–1190.
11 L. Zhao, Y. L. Lin, H. Kim, N. C. Giebink and B. P. Rand, *ACS Energy Lett.*, 2018, **3**, 2708–2712.
12 Y. Chen, B. Liu, Q. Zhou, D. Ma, X. Han, D. He, S. Chen, Y. Li, S. Lu, Z.-X. Xu, C. Chen, H. Yu and J. Chen, *J. Mater. Chem. A*, 2023, **11**, 18592–18604.
13 S. Yu, H. Liu, S. Wang, H. Zhu, X. Dong and X. Li, *Chem. Eng. J.*, 2020, **403**, 125724.
14 N. Li, X. Niu, Q. Chen and H. Zhou, *Chem. Soc. Rev.*, 2020, **49**, 8235–8286.
15 Y. An, J. Hidalgo, C. A. R. Perini, A.-F. Castro-Mendez, J. N. Vagott, K. Bairley, S. Wang, X. Li and J.-P. Correa-Baena, *ACS Energy Lett.*, 2021, **6**, 1942–1969.
16 S. Peng, Z. Yang, M. Sun, L. Yu and Y. Li, *Adv. Mater.*, 2023, **35**, 2304711.
17 M.-H. Park, J. S. Kim, J.-M. Heo, S. Ahn, S.-H. Jeong and T.-W. Lee, *ACS Energy Lett.*, 2019, **4**, 1134–1149.
18 Y. Shi, W. Wu, H. Dong, C. Ran, F. Yuan, M. Zhang, B. Jiao, X. Hou, Z. Wu, G. Li, K. Xi, G. Divitini and Z. Wu, *Adv. Mater.*, 2018, **30**, 1800251.
19 F. Chun, B. Zhang, Y. Gao, X. Wei, Q. Zhang, W. Zheng, J. Zhou, Y. Guo, X. Zhang, Z. Xing, X. Yu and F. Wang, *Nat. Photonics*, 2024, **18**, 856–863.
20 M. Kędziora, A. Opala, R. Mastria, L. De Marco, M. Król, K. Łempicka-Mirek, K. Tyszka, M. Ekielski, M. Guziewicz, K. Bogdanowicz, A. Szerling, H. Sigurðsson, T. Czyszanowski, J. Szczytko, M. Matuszewski, D. Sanvitto and B. Piętka, *Nat. Mater.*, 2024, **23**, 1515–1522.
21 Q. Zhang, Q. Shang, R. Su, T. T. H. Do and Q. Xiong, *Nano Lett.*, 2021, **21**, 1903–1914.
22 H. Wei, Y. Fang, P. Mulligan, W. Chuirazzi, H.-H. Fang, C. Wang, B. R. Ecker, Y. Gao, M. A. Loi, L. Cao and J. Huang, *Nat. Photonics*, 2016, **10**, 333–339.
23 Y. Song, L. Li, M. Hao, W. Bi, A. Wang, Y. Kang, H. Li, X. Li, Y. Fang, D. Yang and Q. Dong, *Adv. Mater.*, 2021, **33**, 2103078.
24 Y. Wang, L. Song, Y. Chen and W. Huang, *ACS Photonics*, 2020, **7**, 10–28.
25 A. Anand, M. L. Zaffalon, A. Erroi, F. Cova, F. Carulli and S. Brovelli, *ACS Energy Lett.*, 2024, **9**, 1261–1287.
26 M. L. Zaffalon, F. Cova, M. Liu, A. Cemmi, I. Di Sarcina, F. Rossi, F. Carulli, A. Erroi, C. Roda, J. Perego, A. Comotti, M. Fasoli, F. Meinardi, L. Li, A. Vedda and S. Brovelli, *Nat. Photonics*, 2022, **16**, 860–868.
27 Q. He, S. Pan, T. Zhang, X. Chen, A. Chen, G. Xu, K. Zhou, J. Li, H. Zhu, O. M. Bakr and J. Pan, *Small*, 2025, **21**, 2410481.
28 C. Zhang, S. Liang, W. Liu, F. T. Eickemeyer, X. Cai, K. Zhou, J. Bian, H. Zhu, C. Zhu, N. Wang, Z. Wang, J. Zhang, Y. Wang, J. Hu, H. Ma, C. Xin, S. M. Zakeeruddin, M. Gratzel and Y. Shi, *Nat. Energy*, 2021, **6**, 1154–1163.
29 Q. Zhou, X. Liu, Z. Liu, Y. Zhu, J. Lu, Z. Chen, C. Li, J. Wang, Q. Xue, F. He, J. Liang, H. Li, S. Wang, Q. Tai, Y. Zhang, J. Liu, C. Zuo, L. Ding, Z. Xiong, R. Zheng, H. Zhang, P. Zhao, X. Jin, P. Wu, F. Zhang, Y. Jiang, H. Zhou, J. Hu, Y. Wang, Y. Song, Y. Mai, B. Xu, S. Liu, L. Han and W. Chen, *Mater. Futures*, 2024, **3**, 022102.
30 B. Chen, P. N. Rudd, S. Yang, J. Huang and Y. Yuan, *Chem. Soc. Rev.*, 2019, **48**, 3842–3867.
31 C. Ma, M.-C. Kang, S.-H. Lee, Y. Zhang, D.-H. Kang, W. Yang, P. Zhao, S.-W. Kim, S. J. Kwon, C.-W. Yang, Y. Yang and N.-G. Park, *J. Am. Chem. Soc.*, 2023, **145**, 24349–24357.
32 Q. He, A. Chen, T. Zhang, X. Chen, X. Bian, G. Xu, S. Pan, T. Chen, J. Yu, Z. Zhang, H. Zhu, G. Lu, O. M. Bakr and J. Pan, *Cell Rep. Phys. Sci.*, 2024, **5**, 102030.
33 Y. Chen and H. Zhou, *J. Appl. Phys.*, 2020, **128**, 060903.
34 H. Zhu, Y. Ren, L. Pan, O. Ouellette, F. T. Eickemeyer, Y. Wu, X. Li, S. Wang, H. Liu, X. Dong, S. M. Zakeeruddin, Y. Liu, A. Hagfeldt and M. Gratzel, *J. Am. Chem. Soc.*, 2021, **143**, 3231–3237.
35 Y. Wu, H. Zhu, D. Wang, S. Akin, F. T. Eickemeyer, D. Ren, H. Cai and L.-B. Huang, *Sol. RRL*, 2022, **6**, 2200115.
36 J. Wang, G. Jin, Q. Zhen, C. He and Y. Duan, *Adv. Mater. Interfaces*, 2021, **8**, 2002078.
37 Q. Fu, X. Tang, B. Huang, T. Hu, L. Tan, L. Chen and Y. Chen, *Adv. Sci.*, 2018, **5**, 1700387.
38 C. C. Boyd, R. Cheacharoen, T. Leijtens and M. D. McGehee, *Chem. Rev.*, 2018, **119**, 3418–3451.
39 A. Singh, F. Matteocci, H. Zhu, D. Rossi, S. Mejaouri, S. Cacovich, M. Auf Der Maur, F. Sauvage, A. Gagliardi, M. Grätzel and A. Di Carlo, *Sol. RRL*, 2021, **5**, 2100277.
40 S. M. Park and E. H. Sargent, *Matter*, 2023, **6**, 2488–2490.
41 C. Liu, Y. Yang, H. Chen, J. Xu, A. Liu, A. S. R. Bati, H. Zhu, L. Grater, S. S. Hadke, C. Huang, V. K. Sangwan, T. Cai, D. Shin, L. X. Chen, M. C. Hersam, C. A. Mirkin, B. Chen, M. G. Kanatzidis and E. H. Sargent, *Science*, 2023, **382**, 810–815.
42 H. Zhu, B. Shao, Z. Shen, S. You, J. Yin, N. Wehbe, L. Wang, X. Song, M. Abulikemu, A. Basaheeh, A. Jamal, I. Gereige, M. Freitag, O. F. Mohammed, K. Zhu and O. M. Bakr, *Nat. Photonics*, 2025, **19**, 28–35.
43 Y. Wu, Q. Liang, H. Zhu, X. Dai, B.-B. Yu, Y. Hu, M. Chen, L.-B. Huang, S. M. Zakeeruddin, Z. Shen, J. Wang and M. Grätzel, *Adv. Funct. Mater.*, 2023, **33**, 2302404.
44 M. Era, S. Morimoto, T. Tsutsui and S. Saito, *Appl. Phys. Lett.*, 1994, **65**, 676–678.
45 A. Kojima, K. Teshima, Y. Shirai and T. Miyasaka, *J. Am. Chem. Soc.*, 2009, **131**, 6050–6051.
46 H.-S. Kim, C.-R. Lee, J.-H. Im, K.-B. Lee, T. Moehl, A. Marchioro, S.-J. Moon, R. Humphry-Baker, J.-H. Yum, J. E. Moser, M. Grätzel and N.-G. Park, *Sci. Rep.*, 2012, **2**, 591.
47 D. Shi, V. Adinolfi, R. Comin, M. Yuan, E. Alarousu, A. Buin, Y. Chen, S. Hoogland, A. Rothenberger, K. Katsiev, Y. Losovyj, X. Zhang, P. A. Dowben, O. F. Mohammed, E. H. Sargent and O. M. Bakr, *Science*, 2015, **347**, 519–522.
48 Q. Dong, Y. Fang, Y. Shao, P. Mulligan, J. Qiu, L. Cao and J. Huang, *Science*, 2015, **347**, 967–970.
49 C. C. Stoumpos, C. D. Malliakas, J. A. Peters, Z. Liu, M. Sebastian, J. Im, T. C. Chasapis, A. C. Wibowo,

D. Y. Chung, A. J. Freeman, B. W. Wessels and M. G. Kanatzidis, *Cryst. Growth Des.*, 2013, **13**, 2722–2727.
50 A. A. Zhumekenov, M. I. Saidaminov, M. A. Haque, E. Alarousu, S. P. Sarmah, B. Murali, I. Dursun, X.-H. Miao, A. L. Abdelhady, T. Wu, O. F. Mohammed and O. M. Bakr, *ACS Energy Lett.*, 2016, **1**, 32–37.
51 K. Almasabi, X. Zheng, B. Turedi, A. Y. Alsalloum, M. N. Lintangpradipto, J. Yin, L. Gutiérrez-Arzaluz, K. Kotsovos, A. Jamal, I. Gereige, O. F. Mohammed and O. M. Bakr, *ACS Energy Lett.*, 2023, **8**, 950–956.
52 M. N. Lintangpradipto, H. Zhu, B. Shao, W. J. Mir, L. Gutiérrez-Arzaluz, B. Turedi, M. Abulikemu, O. F. Mohammed and O. M. Bakr, *ACS Energy Lett.*, 2023, **8**, 4915–4922.
53 H.-S. Rao, W.-G. Li, B.-X. Chen, D.-B. Kuang and C.-Y. Su, *Adv. Mater.*, 2017, **29**, 1602639.
54 X. Zhang, M. Abulikemu, X. Song, B. Shao, R. Zhou, W. Wu, T. Ahmad, O. F. Mohammed and O. M. Bakr, *ACS Mater. Lett.*, 2024, **6**, 3034–3042.
55 X. Zhang, X. Song, M. Abulikemu, B. Shao, S. Chen, L. Gutierrez-Arzaluz, G. Si, T. Ahmad, W. Wu, O. F. Mohammed and O. M. Bakr, *Adv. Funct. Mater.*, 2024, **34**, 2312871.
56 M. Li, S. Wang, A. Wood, J. D. Yeager, S. P. Stepanoff, J. C. Adler, Z. Shi, J. Wang, Z. Li, D. E. Wolfe and J. Huang, *Nat. Mater.*, 2025, DOI: **10.1038/s41563-025-02310-x**.
57 D. Weber, *Z. Naturforsch. B*, 1978, **33**, 1443–1445.
58 R. K. Battula, C. Sudakar, P. Bhyrappa, G. Veerappan and E. Ramasamy, *Cryst. Growth Des.*, 2022, **22**, 6338–6362.
59 M. M. Lee, J. Teuscher, T. Miyasaka, T. N. Murakami and H. J. Snaith, *Science*, 2012, **338**, 643–647.
60 Q. Jiang and K. Zhu, *Nat. Rev. Mater.*, 2024, **9**, 399–419.
61 M. I. Saidaminov, A. L. Abdelhady, B. Murali, E. Alarousu, V. M. Burlakov, W. Peng, I. Dursun, L. Wang, Y. He, G. Maculan, A. Goriely, T. Wu, O. F. Mohammed and O. M. Bakr, *Nat. Commun.*, 2015, **6**, 7586.
62 Q. Chen, J. Wu, X. Ou, B. Huang, J. Almutlaq, A. A. Zhumekenov, X. Guan, S. Han, L. Liang, Z. Yi, J. Li, X. Xie, Y. Wang, Y. Li, D. Fan, D. B. L. Teh, A. H. All, O. F. Mohammed, O. M. Bakr, T. Wu, M. Bettinelli, H. Yang, W. Huang and X. Liu, *Nature*, 2018, **561**, 88–93.
63 H. Chen, C. Liu, J. Xu, A. Maxwell, W. Zhou, Y. Yang, Q. Zhou, A. S. R. Bati, H. Wan, Z. Wang, L. Zeng, J. Wang, P. Serles, Y. Liu, S. Teale, Y. Liu, M. I. Saidaminov, M. Li, N. Rolston, S. Hoogland, T. Filleter, M. G. Kanatzidis, B. Chen, Z. Ning and E. H. Sargent, *Science*, 2024, **384**, 189–193.
64 T. Wang, B. Daiber, J. M. Frost, S. A. Mann, E. C. Garnett, A. Walsh and B. Ehrler, *Energy Environ. Sci.*, 2017, **10**, 509–515.
65 E. M. Hutter, M. C. Gelvez-Rueda, A. Osherov, V. Bulovic, F. C. Grozema, S. D. Stranks and T. J. Savenije, *Nat. Mater.*, 2017, **16**, 115–120.
66 P. Azarhoosh, S. McKechnie, J. M. Frost, A. Walsh and M. van Schilfgaarde, *APL Mater.*, 2016, **4**, 091501.
67 Z. Chen, Q. Dong, Y. Liu, C. Bao, Y. Fang, Y. Lin, S. Tang, Q. Wang, X. Xiao, Y. Bai, Y. Deng and J. Huang, *Nat. Commun.*, 2017, **8**, 1890.
68 Y. Liu, Z. Yang, D. Cui, X. Ren, J. Sun, X. Liu, J. Zhang, Q. Wei, H. Fan, F. Yu, X. Zhang, C. Zhao and S. F. Liu, *Adv. Mater.*, 2015, **27**, 5176–5183.
69 Y. Zhao, S. Wang, H. Ran, Y. Zhang and Y. Tang, *J. Alloys Compd.*, 2023, **965**, 171317.
70 Y. C. Liu, Z. Yang and S. Z. Liu, *Adv. Sci.*, 2018, **5**, 1700471.
71 S.-S. Rong, M. B. Faheem and Y.-B. Li, *J. Electron. Sci. Technol.*, 2021, **19**, 100081.
72 D. Kim, J.-H. Yun, M. Lyu, J. Kim, S. Lim, J. S. Yun, L. Wang and J. Seidel, *J. Phys. Chem. C*, 2019, **123**, 14144–14151.
73 H.-Y. Hou, S. Tian, H.-R. Ge, J.-D. Chen, Y.-Q. Li and J.-X. Tang, *Adv. Funct. Mater.*, 2022, **32**, 2209324.
74 R. Zhuang, X. Wang, W. Ma, Y. Wu, X. Chen, L. Tang, H. Zhu, J. Liu, L. Wu, W. Zhou, X. Liu and Y. Yang, *Nat. Photonics*, 2019, **13**, 602–608.
75 Y. Liu, Z. Yang, D. Cui, X. Ren, J. Sun, X. Liu, J. Zhang, Q. Wei, H. Fan, F. Yu, X. Zhang, C. Zhao and S. Liu, *Adv. Mater.*, 2015, **27**, 5176–5183.
76 D. Liu, X. Sun, L. Jiang, X. Jiang, H. Chen, F. Cui, G. Zhang, Y. Wang, Y.-B. Lu, Z. Wu, Z. Ning and X. Tao, *J. Mater. Chem. A*, 2024, **12**, 12467–12474.
77 S. Meloni, T. Moehl, W. Tress, M. Franckevicius, M. Saliba, Y. H. Lee, P. Gao, M. K. Nazeeruddin, S. M. Zakeeruddin, U. Rothlisberger and M. Graetzel, *Nat. Commun.*, 2016, **7**, 10334.
78 J. Song, X. Feng, H. Li, W. Li, T. Lu, C. Guo, H. Zhang, H. Wei and B. Yang, *J. Phys. Chem. Lett.*, 2020, **11**, 3529–3535.
79 K. Wang, C. Wu, Y. Hou, D. Yang and S. Priya, *J. Mater. Chem. A*, 2019, **7**, 24661–24690.
80 J. Y. Li, Z. Y. Han, Y. Gu, D. J. Yu, J. X. Liu, D. W. Hu, X. B. Xu and H. B. Zeng, *Adv. Funct. Mater.*, 2021, **31**, 2008684.
81 D. Wu, H. Zhang, Z. Wang, Y. Zhang, G. Zhang, K. Wang and C. Z. Ning, *Adv. Opt. Mater.*, 2024, **12**, 2401131.
82 H. Yuan, E. Debroye, K. Janssen, H. Naiki, C. Steuwe, G. Lu, M. Moris, E. Orgiu, I. H. Uji, F. De Schryver, P. Samori, J. Hofkens and M. Roeffaers, *J. Phys. Chem. Lett.*, 2016, **7**, 561–566.
83 X. Cheng, S. Yang, B. Cao, X. Tao and Z. Chen, *Adv. Funct. Mater.*, 2019, **30**, 1905021.
84 J. Huang, Y. Yuan, Y. Shao and Y. Yan, *Nat. Rev. Mater.*, 2017, **2**, 17042.
85 F. Lang, O. Shargaieva, V. V. Brus, H. C. Neitzert, J. Rappich and N. H. Nickel, *Adv. Mater.*, 2018, **30**, 1702905.
86 Z. Zhang and B. Saparov, *Appl. Phys. Lett.*, 2021, **119**, 030502.
87 J. Xing, Q. Wang, Q. Dong, Y. Yuan, Y. Fang and J. Huang, *Phys. Chem. Chem. Phys.*, 2016, **18**, 30484–30490.
88 N. K. Tailor, A. Mahapatra, A. Kalam, M. Pandey, P. Yadav and S. Satapathi, *Phys. Rev. Mater.*, 2022, **6**, 045401.
89 Z. Zhang and G. Yang, *J. Mater. Sci.: Mater. Electron.*, 2020, **32**, 12758–12770.
90 X. Xiao, M. Wu, Z. Ni, S. Xu, S. Chen, J. Hu, P. N. Rudd, W. You and J. Huang, *Adv. Mater.*, 2020, **32**, 2004080.
91 Q. Zhang, X. Liu, X. Zhang, Z. Wang, B. Zhang, Y. Hao, A. Dubois, W. Jie and Y. Xu, *J. Mater. Chem. A*, 2024, **12**, 3304–3310.

92 X. He, Y. Deng, D. Ouyang, N. Zhang, J. Wang, A. A. Murthy, I. Spanopoulos, S. M. Islam, Q. Tu, G. Xing, Y. Li, V. P. Dravid and T. Zhai, *Chem. Rev.*, 2023, **123**, 1207–1261.
93 H. Arandiyan, S. S. Mofarah, C. C. Sorrell, E. Doustkhah, B. Sajjadi, D. Hao, Y. Wang, H. Sun, B.-J. Ni, M. Rezaei, Z. Shao and T. Maschmeyer, *Chem. Soc. Rev.*, 2021, **50**, 10116–10211.
94 Z. Cheng, K. Liu, J. Yang, X. Chen, X. Xie, B. Li, Z. Zhang, L. Liu, C. Shan and D. Shen, *ACS Appl. Mater. Interfaces*, 2019, **11**, 34144–34150.
95 J. Liu, W. Shao, Q. Xu, Y. Liu and X. Ouyang, *IEEE Photonics Technol. Lett.*, 2020, **32**, 635–638.
96 G. Maculan, A. D. Sheikh, A. L. Abdelhady, M. I. Saidaminov, M. A. Haque, B. Murali, E. Alarousu, O. F. Mohammed, T. Wu and O. M. Bakr, *J. Phys. Chem. Lett.*, 2015, **6**, 3781–3786.
97 D. A. Valverde-Chávez, C. S. Ponseca, C. C. Stoumpos, A. Yartsev, M. G. Kanatzidis, V. Sundström and D. G. Cooke, *Energy Environ. Sci.*, 2015, **8**, 3700–3707.
98 S. Yakunin, M. Sytnyk, D. Kriegner, S. Shrestha, M. Richter, G. J. Matt, H. Azimi, C. J. Brabec, J. Stangl, M. V. Kovalenko and W. Heiss, *Nat. Photonics*, 2015, **9**, 444–449.
99 Y. He, W. Ke, G. C. B. Alexander, K. M. McCall, D. G. Chica, Z. Liu, I. Hadar, C. C. Stoumpos, B. W. Wessels and M. G. Kanatzidis, *ACS Photonics*, 2018, **5**, 4132–4138.
100 Y. Song, L. Li, W. Bi, M. Hao, Y. Kang, A. Wang, Z. Wang, H. Li, X. Li, Y. Fang, D. Yang and Q. Dong, *Research*, 2020, **2020**, 5958243.
101 X. Liu, Q. Zhang, D. Zhao, R. Bai, Y. Ruan, B. Zhang, F. Li, M. Zhu, W. Jie and Y. Xu, *ACS Appl. Mater. Interfaces*, 2022, **14**, 51130–51136.
102 E. Alarousu, A. M. El-Zohry, J. Yin, A. A. Zhumekenov, C. Yang, E. Alhabshi, I. Gereige, A. AlSaggaf, A. V. Malko, O. M. Bakr and O. F. Mohammed, *J. Phys. Chem. Lett.*, 2017, **8**, 4386–4390.
103 W.-G. Li, H.-S. Rao, B.-X. Chen, X.-D. Wang and D.-B. Kuang, *J. Mater. Chem. A*, 2017, **5**, 19431–19438.
104 B. B. Zhang, X. Liu, B. Xiao, A. B. Hafsia, K. Gao, Y. Xu, J. Zhou and Y. Chen, *J. Phys. Chem. Lett.*, 2020, **11**, 432–437.
105 A. A. Cheenady and K. Rajan, *J. Appl. Phys.*, 2023, **133**, 205105.
106 Y. Feng, L. Pan, H. Wei, Y. Liu, Z. Ni, J. Zhao, P. N. Rudd, L. R. Cao and J. Huang, *J. Mater. Chem. C*, 2020, **8**, 11360–11368.
107 W. Pan, B. Yang, G. Niu, K. H. Xue, X. Du, L. Yin, M. Zhang, H. Wu, X. S. Miao and J. Tang, *Adv. Mater.*, 2019, **31**, 1904405.
108 G. J. Matt, I. Levchuk, J. Knüttel, J. Dallmann, A. Osvet, M. Sytnyk, X. Tang, J. Elia, R. Hock, W. Heiss and C. J. Brabec, *Adv. Mater. Interfaces*, 2020, **7**, 1901575.
109 Y. He, M. Petryk, Z. Liu, D. G. Chica, I. Hadar, C. Leak, W. Ke, I. Spanopoulos, W. Lin, D. Y. Chung, B. W. Wessels, Z. He and M. G. Kanatzidis, *Nat. Photonics*, 2021, **15**, 36–42.
110 Y. He, C. C. Stoumpos, I. Hadar, Z. Luo, K. M. McCall, Z. Liu, D. Y. Chung, B. W. Wessels and M. G. Kanatzidis, *J. Am. Chem. Soc.*, 2021, **143**, 2068–2077.
111 Z. Zhang, C.-C. Chung, Z. Huang, E. Vetter, D. Seyitliyev, D. Sun, K. Gundogdu, F. N. Castellano, E. O. Danilov and G. Yang, *Mater. Lett.*, 2020, **269**, 127667.
112 W. Pan, H. Wu, J. Luo, Z. Deng, C. Ge, C. Chen, X. Jiang, W.-J. Yin, G. Niu, L. Zhu, L. Yin, Y. Zhou, Q. Xie, X. Ke, M. Sui and J. Tang, *Nat. Photonics*, 2017, **11**, 726–732.
113 J. A. Steele, W. Pan, C. Martin, M. Keshavarz, E. Debroye, H. Yuan, S. Banerjee, E. Fron, D. Jonckheere, C. W. Kim, W. Baekelant, G. Niu, J. Tang, J. Vanacken, M. Van der Auweraer, J. Hofkens and M. B. J. Roeffaers, *Adv. Mater.*, 2018, **30**, 1804450.
114 K. M. McCall, Z. Liu, G. Trimarchi, C. C. Stoumpos, W. Lin, Y. He, I. Hadar, M. G. Kanatzidis and B. W. Wessels, *ACS Photonics*, 2018, **5**, 3748–3762.
115 A. Li, M. Yang, P. Tang, X. Hao, L. Wu, W. Tian, D. Yang and J. Zhang, *ACS Appl. Mater. Interfaces*, 2023, **15**, 23390–23401.
116 W. Li, D. Xin, S. Tie, J. Ren, S. Dong, L. Lei, X. Zheng, Y. Zhao and W. H. Zhang, *J. Phys. Chem. Lett.*, 2021, **12**, 1778–1785.
117 X. J. Zheng, W. Zhao, P. Wang, H. R. Tan, M. I. Saidaminov, S. J. Tie, L. G. Chen, Y. F. Peng, J. D. Long and W. H. Zhang, *J. Energy Chem.*, 2020, **49**, 299–306.
118 S. Tie, W. Zhao, D. Xin, M. Zhang, J. Long, Q. Chen, X. Zheng, J. Zhu and W. H. Zhang, *Adv. Mater.*, 2020, **32**, 2001981.
119 Y. Liu, Z. Xu, Z. Yang, Y. Zhang, J. Cui, Y. He, H. Ye, K. Zhao, H. Sun, R. Lu, M. Liu, M. G. Kanatzidis and S. F. Liu, *Matter*, 2020, **3**, 180–196.
120 Z. Li, X. Wang, P. Zhao, J. Liu and X. Tian, *Inorg. Chem. Front.*, 2024, **11**, 2442–2456.
121 X. Song, Q. Cui, Y. Liu, Z. Xu, H. Cohen, C. Ma, Y. Fan, Y. Zhang, H. Ye, Z. Peng, R. Li, Y. Chen, J. Wang, H. Sun, Z. Yang, Z. Liu, Z. Yang, W. Huang, G. Hodes, S. F. Liu and K. Zhao, *Adv. Mater.*, 2020, **32**, 2003353.
122 Q. Cui, X. Song, Y. Liu, Z. Xu, H. Ye, Z. Yang, K. Zhao and S. Liu, *Matter*, 2021, **4**, 2490–2507.
123 H. Zhu, S. Teale, M. N. Lintangpradipto, S. Mahesh, B. Chen, M. D. McGehee, E. H. Sargent and O. M. Bakr, *Nat. Rev. Mater.*, 2023, **8**, 569–586.
124 A. Rajagopal, A. K. Y. Jen, K. Yao and A. K. Y. Jen, *Adv. Mater.*, 2018, **30**, 1800455.
125 J. Chen and N.-G. Park, *ACS Energy Lett.*, 2020, **5**, 2742–2786.
126 J. Chen, J. Luo, E. Hou, P. Song, Y. Li, C. Sun, W. Feng, S. Cheng, H. Zhang, L. Xie, C. Tian and Z. Wei, *Nat. Photonics*, 2024, **18**, 464–470.
127 B. Xu, H. Zhu, H. Bao, X. Cao, Y. Dong, Y. Zhang, G. Yin, X. Li and S. Wang, *Chem. Eng. J.*, 2022, **431**, 133371.
128 S. G. Motti, D. Meggiolaro, A. J. Barker, E. Mosconi, C. A. R. Perini, J. M. Ball, M. Gandini, M. Kim, F. De Angelis and A. Petrozza, *Nat. Photonics*, 2019, **13**, 532–539.
129 J. Zhao, Z. Su, J. Pascual, H. Wu, H. Wang, M. H. Aldamasy, Z. Zhou, C. Wang, G. Li, Z. Li, X. Gao, C.-S. Hsu and M. Li, *Adv. Mater.*, 2024, **36**, 2406246.
130 Y. Bai, Z. Huang, X. Zhang, J. Lu, X. Niu, Z. He, C. Zhu, M. Xiao, Q. Song, X. Wei, C. Wang, Z. Cui, J. Dou, Y. Chen, F. Pei, H. Zai, W. Wang, T. Song, P. An, J. Zhang, J. Dong,

Y. Li, J. Shi, H. Jin, P. Chen, Y. Sun, Y. Li, H. Chen, Z. Wei, H. Zhou and Q. Chen, *Science*, 2022, **378**, 747–754.
131 M. Ghasemi, B. Guo, K. Darabi, T. Wang, K. Wang, C.-W. Huang, B. M. Lefler, L. Taussig, M. Chauhan, G. Baucom, T. Kim, E. D. Gomez, J. M. Atkin, S. Priya and A. Amassian, *Nat. Mater.*, 2023, **22**, 329–337.
132 J.-N. Yang, J.-J. Wang, Y.-C. Yin and H.-B. Yao, *Chem. Soc. Rev.*, 2023, **52**, 5516–5540.
133 H. Zhu, Y. Liu, F. T. Eickemeyer, L. Pan, D. Ren, M. A. Ruiz-Preciado, B. Carlsen, B. Yang, X. Dong, Z. Wang, H. Liu, S. Wang, S. M. Zakeeruddin, A. Hagfeldt, M. I. Dar, X. Li and M. Grätzel, *Adv. Mater.*, 2020, **32**, 1907757.
134 Y. Wu, H. Zhu, B.-B. Yu, S. Akin, Y. Liu, Z. Shen, L. Pan and H. Cai, *Chem. Eng. J.*, 2022, **433**, 134613.
135 C. Ma and N.-G. Park, *ACS Energy Lett.*, 2020, **5**, 3268–3275.
136 R. Chen, J. Wang, Z. Liu, F. Ren, S. Liu, J. Zhou, H. Wang, X. Meng, Z. Zhang, X. Guan, W. Liang, P. A. Troshin, Y. Qi, L. Han and W. Chen, *Nat. Energy*, 2023, **8**, 839–849.
137 J. S. Yun, J. Kim, T. Young, R. J. Patterson, D. Kim, J. Seidel, S. Lim, M. A. Green, S. Huang and A. Ho-Baillie, *Adv. Funct. Mater.*, 2018, **28**, 1705363.
138 M. M. Byranvand, A. N. Kharat and N. Taghavinia, *Mater. Lett.*, 2019, **237**, 356–360.
139 L. Yadegari, Z. Rastegar Moghadamgohari, N. Zarabinia and R. Rasuli, *Sci. Rep.*, 2023, **13**, 13497.
140 Q. Wang, B. Chen, Y. Liu, Y. Deng, Y. Bai, Q. Dong and J. Huang, *Energy Environ. Sci.*, 2017, **10**, 516–522.
141 E. J. Juarez-Perez, L. K. Ono, M. Maeda, Y. Jiang, Z. Hawash and Y. Qi, *J. Mater. Chem. A*, 2018, **6**, 9604–9612.
142 N. H. Nickel, F. Lang, V. V. Brus, O. Shargaieva and J. Rappich, *Adv. Electron. Mater.*, 2017, **3**, 1700158.
143 G. Divitini, S. Cacovich, F. Matteocci, L. Cina, A. Di Carlo and C. Ducati, *Nat. Energy*, 2016, **1**, 15012.
144 R. Garai, R. K. Gupta and P. K. Iyer, *Acc. Mater. Res.*, 2023, **4**, 560–565.
145 S. Xie, A. Feng, L. Wang, N. Li, X. Cheng, W. Zhang, C. Li, Y. Liu, G. Zhang, X. Du, Y. Fang, Z. Chen and X. Tao, *ACS Mater. Lett.*, 2022, **4**, 1332–1340.
146 H.-H. Sung, C.-C. Kuo, H.-S. Chiang, H.-L. Yue and F.-C. Chen, *Sol. RRL*, 2019, **3**, 1900130.
147 P. Zhang, G. Zhang, L. Liu, D. Ju, L. Zhang, K. Cheng and X. Tao, *J. Phys. Chem. Lett.*, 2018, **9**, 5040–5046.
148 X. Liu, H. Zhang, B. Zhang, J. Dong, W. Jie and Y. Xu, *J. Phys. Chem. C*, 2018, **122**, 14355–14361.
149 Z. Lian, Q. Yan, T. Gao, J. Ding, Q. Lv, C. Ning, Q. Li and J.-L. Sun, *J. Am. Chem. Soc.*, 2016, **138**, 9409–9412.
150 Y. Dang, Y. Zhou, X. Liu, D. Ju, S. Xia, H. Xia and X. Tao, *Angew. Chem., Int. Ed.*, 2016, **55**, 3447–3450.
151 W. Li, H. Li, J. Song, C. Guo, H. Zhang, H. Wei and B. Yang, *Sci. Bull.*, 2021, **66**, 2199–2206.
152 Y. He, L. Matei, H. J. Jung, K. M. McCall, M. Chen, C. C. Stoumpos, Z. Liu, J. A. Peters, D. Y. Chung, B. W. Wessels, M. R. Wasielewski, V. P. Dravid, A. Burger and M. G. Kanatzidis, *Nat. Commun.*, 2018, **9**, 1609.
153 Q. Wang, C. E. Wang, Z. Wang, X. Sun, M. Nikl, X. OuYang and Y. Wu, *J. Phys. Chem. Lett.*, 2022, **13**, 9066–9071.
154 W. Lin, J. He, K. M. McCall, C. C. Stoumpos, Z. Liu, I. Hadar, S. Das, H.-H. Wang, B.-X. Wang, D. Y. Chung, B. W. Wessels and M. G. Kanatzidis, *Adv. Funct. Mater.*, 2021, **31**, 2006635.
155 Y. He, C. C. Stoumpos, I. Hadar, Z. Luo, K. M. McCall, Z. Liu, D. Y. Chung, B. W. Wessels and M. G. Kanatzidis, *J. Am. Chem. Soc.*, 2021, **143**, 2068–2077.
156 I. Chung, B. Lee, J. He, R. P. H. Chang and M. G. Kanatzidis, *Nature*, 2012, **485**, 486–489.
157 M. I. Saidaminov, A. L. Abdelhady, G. Maculan and O. M. Bakr, *Chem. Commun.*, 2015, **51**, 17658–17661.
158 C. C. Stoumpos, D. H. Cao, D. J. Clark, J. Young, J. M. Rondinelli, J. I. Jang, J. T. Hupp and M. G. Kanatzidis, *Chem. Mater.*, 2016, **28**, 2852–2867.
159 Y. Dang, C. Zhong, G. Zhang, D. Ju, L. Wang, S. Xia, H. Xia and X. Tao, *Chem. Mater.*, 2016, **28**, 6968–6974.
160 Y. Haruta, H. Ye, P. Huber, N. Sandor, A. J. Pavesic, S. Dayneko, S. Qiu, V. Yeddu and M. I. Saidaminov, *Nat. Synth.*, 2024, **3**, 1212–1220.
161 Y. Liu, J. Sun, Z. Yang, D. Yang, X. Ren, H. Xu, Z. Yang and S. F. Liu, *Adv. Opt. Mater.*, 2016, **4**, 1829–1837.
162 Q. Lv, Z. Lian, W. He, J.-L. Sun, Q. Li and Q. Yan, *J. Mater. Chem. C*, 2018, **6**, 4464–4470.
163 L. Lee, J. Baek, K. S. Park, Y.-E. Lee, N. K. Shrestha and M. M. Sung, *Nat. Commun.*, 2017, **8**, 15882.
164 L. Li, J. Liu, M. Zeng and L. Fu, *Nano Res.*, 2020, **14**, 1609–1624.
165 Z. Gu, Z. Huang, C. Li, M. Li and Y. Song, *Sci. Adv.*, 2018, **4**, eaat2390.
166 A. A. Zhumekenov, V. M. Burlakov, M. I. Saidaminov, A. Alofi, M. A. Haque, B. Turedi, B. Davaasuren, I. Dursun, N. Cho, A. M. El-Zohry, M. De Bastiani, A. Giugni, B. Torre, E. Di Fabrizio, O. F. Mohammed, A. Rothenberger, T. Wu, A. Goriely and O. M. Bakr, *ACS Energy Lett.*, 2017, **2**, 1782–1788.
167 K. Wang, C. Wu, D. Yang, Y. Jiang and S. Priya, *ACS Nano*, 2018, **12**, 4919–4929.
168 Y. Liu, H. Ye, Y. Zhang, K. Zhao, Z. Yang, Y. Yuan, H. Wu, G. Zhao, Z. Yang, J. Tang, Z. Xu and S. Liu, *Matter*, 2019, **1**, 465–480.
169 Y. Wang, X. Sun, Z. Chen, Y.-Y. Sun, S. Zhang, T.-M. Lu, E. Wertz and J. Shi, *Adv. Mater.*, 2017, **29**, 1702643.
170 Y.-X. Chen, Q.-Q. Ge, Y. Shi, J. Liu, D.-J. Xue, J.-Y. Ma, J. Ding, H.-J. Yan, J.-S. Hu and L.-J. Wan, *J. Am. Chem. Soc.*, 2016, **138**, 16196–16199.
171 J. Chen, D. J. Morrow, Y. Fu, W. Zheng, Y. Zhao, L. Dang, M. J. Stolt, D. D. Kohler, X. Wang, K. J. Czech, M. P. Hautzinger, S. Shen, L. Guo, A. Pan, J. C. Wright and S. Jin, *J. Am. Chem. Soc.*, 2017, **139**, 13525–13532.
172 Y. Lei, Y. Chen, R. Zhang, Y. Li, Q. Yan, S. Lee, Y. Yu, H. Tsai, W. Choi, K. Wang, Y. Luo, Y. Gu, X. Zheng, C. Wang, C. Wang, H. Hu, Y. Li, B. Qi, M. Lin, Z. Zhang, S. A. Dayeh, M. Pharr, D. P. Fenning, Y.-H. Lo, J. Luo, K. Yang, J. Yoo, W. Nie and S. Xu, *Nature*, 2020, **583**, 790–795.
173 Y. Lei, Y. Chen, Y. Gu, C. Wang, Z. Huang, H. Qian, J. Nie, G. Hollett, W. Choi, Y. Yu, N. Kim, C. Wang, T. Zhang,

H. Hu, Y. Zhang, X. Li, Y. Li, W. Shi, Z. Liu, M. J. Sailor, L. Dong, Y.-H. Lo, J. Luo and S. Xu, *Adv. Mater.*, 2018, **30**, 1705992.

174 Y. M. Chen, Y. S. Lei, Y. H. Li, Y. G. Yu, J. Z. Cai, M. H. Chiu, R. Rao, Y. Gu, C. F. Wang, W. J. Choi, H. J. Hu, C. H. Wang, Y. Li, J. W. Song, J. X. Zhang, B. Y. Qi, M. Y. Lin, Z. R. Zhang, A. E. Islam, B. Maruyama, S. Dayeh, L. J. Li, K. S. Yang, Y. H. Lo and S. Xu, *Nature*, 2020, **577**, 209–215.

175 M. Yuan, J. Feng, H. Li, H. Gao, Y. Qiu, L. Jiang and Y. Wu, *Nat. Nanotechnol.*, 2025, **20**, 381–387.

176 J. Wu, J. Chen, Y. Zhang, Z. Xu, L. Zhao, T. Liu, D. Luo, W. Yang, K. Chen, Q. Hu, F. Ye, P. Wu, R. Zhu, Q. Gong, R. Zhu, Q. Gong, R. Zhu and Q. Gong, *Nano Lett.*, 2017, **17**, 3563–3569.

177 Y. Kim, S. S. Cruz, K. Lee, B. O. Alawode, C. Choi, Y. Song, J. M. Johnson, C. Heidelberger, W. Kong, S. Choi, K. Qiao, I. Almansouri, E. A. Fitzgerald, J. Kong, A. M. Kolpak, J. Hwang and J. Kim, *Nature*, 2017, **544**, 340–343.

178 W. Kong, H. Li, K. Qiao, Y. Kim, K. Lee, Y. Nie, D. Lee, T. Osadchy, R. J. Molnar, D. K. Gaskill, R. L. Myers-Ward, K. M. Daniels, Y. Zhang, S. Sundram, Y. Yu, S.-H. Bae, S. Rajan, Y. Shao-Horn, K. Cho, A. Ougazzaden, J. C. Grossman and J. Kim, *Nat. Mater.*, 2018, **17**, 999–1004.

179 H. Li, J. Song, W. Pan, D. Xu, W.-A. Zhu, H. Wei and B. Yang, *Adv. Mater.*, 2020, **32**, 2003790.

180 J. Jiang, X. Sun, X. Chen, B. Wang, Z. Chen, Y. Hu, Y. Guo, L. Zhang, Y. Ma, L. Gao, F. Zheng, L. Jin, M. Chen, Z. Ma, Y. Zhou, N. P. Padture, K. Beach, H. Terrones, Y. Shi, D. Gall, T.-M. Lu, E. Wertz, J. Feng and J. Shi, *Nat. Commun.*, 2019, **10**, 4145.

181 W. Guo, Z. Xu, F. Zhang, S. Xie, H. Xu and X. Y. Liu, *Adv. Funct. Mater.*, 2016, **26**, 8855–8884.

182 L. Liang, Y. Cai, X. Li, M. K. Nazeeruddin and P. Gao, *Nano Energy*, 2018, **52**, 211–238.

183 N. Q. Liu, N. Li, C. K. Jiang, D. L. Han, J. T. Dai, Y. W. Niu, Y. J. Dou, S. S. Chen, Y. M. Chen, Z. L. Chen and X. T. Tao, *Adv. Funct. Mater.*, 2024, **34**, 2410631.

184 C. K. Jiang, N. Li, Y. W. Niu, N. Q. Liu, D. L. Li, G. Jin, Y. Zhong, X. T. Tao and Z. L. Chen, *Angew. Chem., Int. Ed.*, 2024, **63**, e202412485.

185 N. Liu, M. Liu, J. Dai, X. Cheng and Z. Chen, *Angew. Chem., Int. Ed.*, 2025, e202500947.

186 M. Lv, N. Li, G. Jin, X. Du, X. Tao and Z. Chen, *Matter*, 2023, **6**, 4388–4400.

187 K. Almasabi, X. P. Zheng, B. Turedi, A. Y. Alsalloum, M. N. Lintangpradipto, J. Yin, L. Gutierrez-Arzaluz, K. Kotsovos, A. Jamal, I. Gereige, O. F. Mohammed and O. M. Bakr, *ACS Energy Lett.*, 2023, **8**, 950–956.

188 A. Y. Alsalloum, B. Turedi, K. Almasabi, X. Zheng, R. Naphade, S. D. Stranks, O. F. Mohammed and O. M. Bakr, *Energy Environ. Sci.*, 2021, **14**, 2263–2268.

189 N. Q. Liu, N. Li, C. K. Jiang, M. X. Lv, J. M. Wu and Z. L. Chen, *Angew. Chem., Int. Ed.*, 2024, **63**, e202314089.

190 Y. Huang, Y. Zhang, J. Sun, X. Wang, J. Sun, Q. Chen, C. Pan and H. Zhou, *Adv. Mater. Interfaces*, 2018, **5**, 1800224.

191 V. Yeddu, P. Moazzezi, B. Turedi, M. N. Lintangpradipto, D. Y. Zhang, S. Kundu, D. T. Gangadharan, R. Gordon, O. M. Bakr and M. I. Saidaminov, *ACS Appl. Energy Mater.*, 2023, **6**, 2257–2264.

192 A. Y. Alsalloum, B. Turedi, X. P. Zheng, S. Mitra, A. A. Zhumekenov, K. J. Lee, P. Maity, I. Gereige, A. AlSaggaf, I. S. Rogan, O. F. Mohammed and O. M. Bakr, *ACS Energy Lett.*, 2020, **5**, 657–662.

193 Z. Chen, B. Turedi, A. Y. Alsalloum, C. Yang, X. Zheng, I. Gereige, A. AlSaggaf, O. F. Mohammed and O. M. Bakr, *ACS Energy Lett.*, 2019, **4**, 1258–1259.

194 T. P. Zhao, R. Q. He, T. H. Liu, Y. H. Li, D. Yu, Y. X. Gao, G. Y. Qu, N. Li, C. M. Wang, H. Huang, J. Zhou, S. Bai, S. M. Xiao, Z. L. Chen, Y. M. Chen and Q. H. Song, *ACS Nano*, 2025, **19**, 3282–3292.

195 N. Li, A. Feng, X. Guo, J. Wu, S. Xie, Q. Lin, X. Jiang, Y. Liu, Z. Chen and X. Tao, *Adv. Energy Mater.*, 2022, **12**, 2103241.

196 X. Guo, N. Li, Y. Xu, J. Zhao, F. Cui, Y. Chen, X. Du, Q. Song, G. Zhang, X. Cheng, X. Tao and Z. Chen, *Adv. Funct. Mater.*, 2023, **33**, 2213995.

197 M. Younas, M. A. Gondal and M. A. Dastageer, *Int. J. Energy Res.*, 2021, **45**, 5555–5566.

198 H.-L. Yue, H.-H. Sung and F.-C. Chen, *Adv. Electron. Mater.*, 2018, **4**, 1700655.

199 T.-H. Wu, G. D. Sharma and F.-C. Chen, *Processes*, 2022, **10**, 1477.

200 Y. Liu, Q. Dong, Y. Fang, Y. Lin, Y. Deng and J. Huang, *Adv. Funct. Mater.*, 2019, **29**, 1807707.

201 Q. F. Dong, J. F. Song, Y. J. Fang, Y. C. Shao, S. Ducharme and J. S. Huang, *Adv. Mater.*, 2016, **28**, 2816–2821.

202 J. Park, Y. E. Bak, L. Lee, H. Choi, M. A. Khan and M. M. Sung, *ChemSusChem*, 2020, **13**, 1882–1889.

203 T. Ye, W. Fu, J. Wu, Z. Yu, X. Jin, H. Chen and H. Li, *J. Mater. Chem. A*, 2016, **4**, 1214–1217.

204 Y. Liu, X. Ren, J. Zhang, Z. Yang, D. Yang, F. Yu, J. Sun, C. Zhao, Z. Yao, B. Wang, Q. Wei, F. Xiao, H. Fan, H. Deng, L. Deng and S. F. Liu, *Sci. China:Chem.*, 2017, **60**, 1367–1376.

205 Y. Song, W. Bi, A. Wang, X. Liu, Y. Kang and Q. Dong, *Nat. Commun.*, 2020, **11**, 274.

206 J. Zhao, G. Kong, S. Chen, Q. Li, B. Huang, Z. Liu, X. San, Y. Wang, C. Wang, Y. Zhen, H. Wen, P. Gao and J. Li, *Sci. Bull.*, 2017, **62**, 1173–1176.

207 C. C. Kuo, G. D. Sharma and F. C. Chen, *Surf. Interfaces*, 2022, **30**, 101858.

208 W. Peng, L. Wang, B. Murali, K.-T. Ho, A. Bera, N. Cho, C.-F. Kang, V. M. Burlakov, J. Pan, L. Sinatra, C. Ma, W. Xu, D. Shi, E. Alarousu, A. Goriely, J.-H. He, O. F. Mohammed, T. Wu and O. M. Bakr, *Adv. Mater.*, 2016, **28**, 3383–3390.

209 T. Kim, Y. H. Chu, J. Lee, S. H. Cho, S. Kim, K. Bang, H. Lee, C. Lim and Y. S. Lee, *Electron. Mater. Lett.*, 2021, **17**, 347–354.

210 H.-S. Rao, B.-X. Chen, X.-D. Wang, D.-B. Kuang and C.-Y. Su, *Chem. Commun.*, 2017, **53**, 5163–5166.

211 J. Wu, F. J. Ye, W. Q. Yang, Z. J. Xu, D. Y. Luo, R. Su, Y. F. Zhang, R. Zhu and Q. H. Gong, *Chem. Mater.*, 2018, **30**, 4590–4596.

212 L. T. Dai, P. R. I. Roca i Cabarroca, H. X. Ban, Z. G. Zhang, Q. Sun, X. J. Li, A. J. Gu, W. P. Yang, H. X. Yu, Y. Shen and M. K. Wang, *Small*, 2023, **19**, 2208062.
213 T. Singh, J. Singh and T. Miyasaka, *ChemSusChem*, 2016, **9**, 2559–2566.
214 Y. M. Yu and P. Gao, *Chin. Chem. Lett.*, 2017, **28**, 1144–1152.
215 M. A. Mat Teridi, M. F. Mohamad Noh, C. H. Teh, R. Daik, E. L. Lim, C. C. Yap, M. A. A. Ibrahim, N. Ahmad Ludin, A. R. B. Mohd Yusoff and J. Jang, *J. Mater. Chem. C*, 2018, **6**, 682–712.
216 W. Q. Wu, D. H. Chen, R. A. Caruso and Y. B. Cheng, *J. Mater. Chem. A*, 2017, **5**, 10092–10109.
217 P. Ganesan, M. K. Nazeeruddin and P. Gao, *Adv. Funct. Mater.*, 2025, **35**, 2409939.
218 M. Azam, T. Du, Z. Wan, H. Zhao, H. Zeng, R. Wei, C. J. Brabec, J. Luo and C. Jia, *Energy Environ. Sci.*, 2024, **17**, 6974–7016.
219 Y. Yao, C. Cheng, C. Zhang, H. Hu, K. Wang and S. De Wolf, *Adv. Mater.*, 2022, **34**, 2203794.
220 H. Zhu, Z. Shen, L. Pan, J. Han, F. T. Eickemeyer, Y. Ren, X. Li, S. Wang, H. Liu, X. Dong, S. M. Zakeeruddin, A. Hagfeldt, Y. Liu and M. Grätzel, *ACS Energy Lett.*, 2021, **6**, 208–215.
221 National Renewable Energy Laboratory Best Research-Cell Efficiency Chart, **https://www.nrel.gov/pv/cell-efficiency.html** (accessed: March 2025).
222 J. Liu, Y. He, L. Ding, H. Zhang, Q. Li, L. Jia, J. Yu, T. W. Lau, M. Li, Y. Qin, X. Gu, F. Zhang, Q. Li, Y. Yang, S. Zhao, X. Wu, J. Liu, T. Liu, Y. Gao, Y. Wang, X. Dong, H. Chen, P. Li, T. Zhou, M. Yang, X. Ru, F. Peng, S. Yin, M. Qu, D. Zhao, Z. Zhao, M. Li, P. Guo, H. Yan, C. Xiao, P. Xiao, J. Yin, X. Zhang, Z. Li, B. He and X. Xu, *Nature*, 2024, **635**, 596–603.
223 Y. Wang, R. Lin, C. Liu, X. Wang, C. Chosy, Y. Haruta, A. D. Bui, M. Li, H. Sun, X. Zheng, H. Luo, P. Wu, H. Gao, W. Sun, Y. Nie, H. Zhu, K. Zhou, H. T. Nguyen, X. Luo, L. Li, C. Xiao, M. I. Saidaminov, S. D. Stranks, L. Zhang and H. Tan, *Nature*, 2024, **635**, 867–873.
224 H. Zhu, B. Shao, J. Yin, Z. Shen, L. Wang, R.-W. Huang, B. Chen, N. Wehbe, T. Ahmad, M. Abulikemu, A. Jamal, I. Gereige, M. Freitag, O. F. Mohammed, E. H. Sargent and O. M. Bakr, *Adv. Mater.*, 2024, **36**, 2306466.
225 H. Zai, P. Yang, J. Su, R. Yin, R. Fan, Y. Wu, X. Zhu, Y. Ma, T. Zhou, W. Zhou, Y. Zhang, Z. Huang, Y. Jiang, N. Li, Y. Bai, C. Zhu, Z. Huang, J. Chang, Q. Chen, Y. Zhang and H. Zhou, *Science*, 2025, **387**, 186–192.
226 B. Wu, Y. Zhou, G. Xing, Q. Xu, H. F. Garces, A. Solanki, T. W. Goh, N. P. Padture and T. C. Sum, *Adv. Funct. Mater.*, 2017, **27**, 1604818.
227 E. B. Podgoršak, in *Radiation Physics for Medical Physicists*, ed. E. B. Podgorsak, Springer International Publishing, Cham, 2016, pp. 79–142. , DOI: **10.1007/978-3-319-25382-4_2**.
228 H. D. Wu, Y. S. Ge, G. D. Niu and J. Tang, *Matter*, 2021, **4**, 144–163.
229 H. Wei and J. Huang, *Nat. Commun.*, 2019, **10**, 1066.
230 S. Kasap, J. B. Frey, G. Belev, O. Tousignant, H. Mani, J. Greenspan, L. Laperriere, O. Bubon, A. Reznik, G. DeCrescenzo, K. S. Karim and J. A. Rowlands, *Sensors*, 2011, **11**, 5112–5157.
231 R. Devanathan, L. R. Corrales, F. Gao and W. J. Weber, *Nucl. Instrum. Methods Phys. Res., Sect. A*, 2006, **565**, 637–649.
232 X. Liu, J. Ren, Y.-A. Chen, X. Geng, D. Xie and T.-L. Ren, *Sci. China: Inf. Sci.*, 2024, **67**, 131401.
233 T. E. Schlesinger, J. E. Toney, H. Yoon, E. Y. Lee, B. A. Brunett, L. Franks and R. B. James, *Mater. Sci. Eng., R*, 2001, **32**, 103–189.
234 S. D. Sordo, L. Abbene, E. Caroli, A. M. Mancini, A. Zappettini and P. Ubertini, *Sensors*, 2009, **9**, 3491–3526.
235 P. Büchele, M. Richter, S. F. Tedde, G. J. Matt, G. N. Ankah, R. Fischer, M. Biele, W. Metzger, S. Lilliu, O. Bikondoa, J. E. Macdonald, C. J. Brabec, T. Kraus, U. Lemmer and O. Schmidt, *Nat. Photonics*, 2015, **9**, 843–848.
236 N. Kawano, M. Koshimizu, G. Okada, Y. Fujimoto, N. Kawaguchi, T. Yanagida and K. Asai, *Sci. Rep.*, 2017, **7**, 14754.
237 Y. Shen, Y. Liu, H. Ye, Y. Zheng, Q. Wei, Y. Xia, Y. Chen, K. Zhao, W. Huang and S. F. Liu, *Angew. Chem., Int. Ed.*, 2020, **59**, 14896–14902.
238 Y. Huang, L. Qiao, Y. Jiang, T. He, R. Long, F. Yang, L. Wang, X. Lei, M. Yuan and J. Chen, *Angew. Chem., Int. Ed.*, 2019, **58**, 17834–17842.
239 X. Wang, Y. W. Li, Y. B. Xu, Y. Z. Pan, C. Y. Zhu, D. J. Zhu, Y. Wu, G. W. Li, Q. Zhang, Q. Li, X. B. Zhang, J. Wu, J. Chen and W. Lei, *Chem. Mater.*, 2020, **32**, 4973–4983.
240 K. Sakhatskyi, B. Turedi, G. J. Matt, E. Wu, A. Sakhatska, V. Bartosh, M. N. Lintangpradipto, R. Naphade, I. Shorubalko, O. F. Mohammed, S. Yakunin, O. M. Bakr and M. V. Kovalenko, *Nat. Photonics*, 2023, **17**, 510–517.
241 X. Song, X. Zhang, T. He, J. Wang, H. Zhu, R. Zhou, T. Ahmad, O. M. Bakr and O. F. Mohammed, *ACS Cent. Sci.*, 2024, **10**, 2082–2089.
242 X. Ou and F. Gao, *Nat. Commun.*, 2024, **15**, 5754.
243 R. Saran and R. J. Curry, *Nat. Photonics*, 2016, **10**, 81–92.
244 J. Zhao, X. Wang, Y. Li, Q. Cheng, D. C. Onwudiwe, B. S. Bae, M. Ertuğrul, Y. Zhu, W. Lei and X. Xu, *InfoMat*, 2025, **7**, e12632.
245 Y. C. Kim, K. H. Kim, D.-Y. Son, D.-N. Jeong, J.-Y. Seo, Y. S. Choi, I. T. Han, S. Y. Lee and N.-G. Park, *Nature*, 2017, **550**, 87–91.
246 W. Wei, Y. Zhang, Q. Xu, H. Wei, Y. Fang, Q. Wang, Y. Deng, T. Li, A. Gruverman, L. Cao and J. Huang, *Nat. Photonics*, 2017, **11**, 315–321.
247 K. R. Dudipala, T. H. Le, W. Nie and R. L. Z. Hoye, *Adv. Mater.*, 2024, **36**, 2304523.
248 B. Fraboni, A. Ciavatti, L. Basirico and A. Fraleoni-Morgera, *Faraday Discuss.*, 2014, **174**, 219–234.
249 F. Arfelli, G. Barbiellini, G. Cantatore, E. Castelli, P. Cristaudo, L. Dalla Palma, M. Di Michiel, R. Longo, P. Poropat, R. Rosei, M. Sessa, F. Tomasini, G. Tromba and

A. Vacchi, *Nucl. Instrum. Methods Phys. Res., Sect. A*, 1994, **353**, 366–370.
250 G. Rikner and E. Grusell, *Phys. Med. Biol.*, 1983, **28**, 1261.
251 S. Kasap, J. B. Frey, G. Belev, O. Tousignant, H. Mani, J. Greenspan, L. Laperriere, O. Bubon, A. Reznik, G. DeCrescenzo, K. S. Karim and J. A. Rowlands, *Sensors*, 2011, **11**, 5112–5157.
252 D. Chu, B. Jia, N. Liu, Y. Zhang, X. Li, J. Feng, J. Pi, Z. Yang, G. Zhao, Y. Liu, S. F. Liu and N. G. Park, *Sci. Adv.*, 2023, **9**, eadh2255.
253 D. Liu, Y. Zheng, X. Y. Sui, X. F. Wu, C. Zou, Y. Peng, X. Liu, M. Lin, Z. Wei, H. Zhou, Y. F. Yao, S. Dai, H. Yuan, H. G. Yang, S. Yang and Y. Hou, *Nat. Commun.*, 2024, **15**, 2390.
254 Y. Liu, Y. Zhang, X. Zhu, J. Feng, I. Spanopoulos, W. Ke, Y. He, X. Ren, Z. Yang, F. Xiao, K. Zhao, M. Kanatzidis and S. F. Liu, *Adv. Mater.*, 2021, **33**, 2006010.
255 D. Chu, B. Jia, N. Liu, Y. Zhang, X. Li, J. Feng, J. Pi, Z. Yang, G. Zhao, Y. Liu, S. Z. F. Liu and N.-G. Park, *Sci. Adv.*, 2023, **9**, eadh2255.
256 J. Jiang, M. Xiong, K. Fan, C. Bao, D. Xin, Z. Pan, L. Fei, H. Huang, L. Zhou, K. Yao, X. Zheng, L. Shen and F. Gao, *Nat. Photonics*, 2022, **16**, 575–581.
257 L. Zhao, Y. Zhou, Z. F. Shi, Z. Y. Ni, M. R. Wang, Y. Liu and J. S. Huang, *Nat. Photonics*, 2023, **17**, 315–323.
258 V. V. Klepov, M. C. De Siena, I. R. Pandey, L. Pan, K. S. Bayikadi, S. Butun, D. Y. Chung and M. G. Kanatzidis, *ACS Appl. Mater. Interfaces*, 2023, **15**, 16895–16901.
259 Y. Hua, G. Zhang, X. Sun, P. Zhang, Y. Hao, Y. Xu, Y. Yang, Q. Lin, X. Li, Z. Zhai, F. Cui, H. Liu, J. Liu and X. Tao, *Nat. Photonics*, 2024, **18**, 870–877.
260 B. Zhang, T. Zheng, J. You, C. Ma, Y. Liu, L. Zhang, J. Xi, G. Dong, M. Liu and S. F. Liu, *Adv. Mater.*, 2023, **35**, 2208875.
261 M. Xia, X. Sun, F. Ye, M. Liao, J. Liu, S. Liu, D. Wu, Y. Xu, X. Zhang, K. H. Xue, X. Miao, J. Tang and G. Niu, *Adv. Mater.*, 2024, **36**, 2313663.
262 Y. Han, S. Yue and B. B. Cui, *Adv. Sci.*, 2021, **8**, 2004805.
263 A. H. Proppe, M. Wei, B. Chen, R. Quintero-Bermudez, S. O. Kelley and E. H. Sargent, *J. Am. Chem. Soc.*, 2019, **141**, 14180–14189.
264 C. R. Roy, D. Pan, Y. Wang, M. P. Hautzinger, Y. Zhao, J. C. Wright, Z. Zhu and S. Jin, *J. Am. Chem. Soc.*, 2021, **143**, 5212–5221.
265 M. Y. Kuo, N. Spitha, M. P. Hautzinger, P. L. Hsieh, J. Li, D. Pan, Y. Zhao, L. J. Chen, M. H. Huang, S. Jin, Y. J. Hsu and J. C. Wright, *J. Am. Chem. Soc.*, 2021, **143**, 4969–4978.
266 Y. He, W. Pan, C. Guo, H. Zhang, H. Wei and B. Yang, *Adv. Funct. Mater.*, 2021, **31**, 2104880.
267 X. Zhang, X. Song, M. Abulikemu, B. Shao, S. Chen, L. Gutiérrez-Arzaluz, G. Si, T. Ahmad, W. Wu, O. F. Mohammed and O. M. Bakr, *Adv. Funct. Mater.*, 2023, **34**, 2312871.
268 Q. Guan, S. You, Z. K. Zhu, R. Li, H. Ye, C. Zhang, H. Li, C. Ji, X. Liu and J. Luo, *Angew. Chem., Int. Ed.*, 2024, **63**, e202320180.
269 Q. Guan, H. Ye, S. You, Z. K. Zhu, H. Li, X. Liu and J. Luo, *Small*, 2024, **20**, 2307908.
270 K. Guo, W. Li, Y. He, X. Feng, J. Song, W. Pan, W. Qu, B. Yang and H. Wei, *Angew. Chem., Int. Ed.*, 2023, **62**, e202303445.
271 A. T. Gidey, Y. Haruta, A. P. Herman, M. Grodzicki, A. M. Melnychenko, D. Majchrzak, S. Mahato, E. Rogowicz, M. Syperek, R. Kudrawiec, M. I. Saidaminov and A. L. Abdelhady, *J. Phys. Chem. Lett.*, 2023, **14**, 9136–9144.
272 J. Yan, F. Gao, Y. Z. Tian, Y. Li, W. Q. Gong, S. P. Wang, H. Zhu and L. Li, *Adv. Opt. Mater.*, 2022, **10**, 2200449.
273 C. Ma, L. L. Gao, Z. Xu, X. T. Li, X. Song, Y. C. Liu, T. H. Yang, H. J. Li, Y. C. Du, G. T. Zhao, X. M. Liu, M. G. Kanatzidis, S. F. Liu and K. Zhao, *Chem. Mater.*, 2022, **34**, 1699–1709.
274 F. Cui, P. Zhang, L. Zhang, Y. Hua, X. Sun, X. Li, G. Zhang and X. Tao, *Chem. Mater.*, 2022, **34**, 9601–9612.
275 X. Du, Y. Liu, W. Pan, J. Pang, J. Zhu, S. Zhao, C. Chen, Y. Yu, Z. Xiao, G. Niu and J. Tang, *Adv. Mater.*, 2022, 2110252.
276 L. Z. Ying Zhou, Z. Ni, S. Xu, J. Zhao, X. Xiao and J. Huang, *Sci. Adv.*, 2021, **7**, eabg6716.
277 Y. Pan, X. Wang, J. Zhao, Y. Xu, Y. Li, Q. Li, X. Zhang, Z. Zhao, Z. Zhu, C. Jing, W. Jun, E. Emeka Elemike, B. S. Bae and W. Lei, *CrystEngComm*, 2021, **23**, 4954–4962.
278 M. Kovalenko, K. Sakhatskyi, B. Turedi, G. Matt, M. Lintangpradipto, R. Naphade, O. Mohammed, S. Yakunin and O. Bakr, *Research Square Platform LL*, 2023, DOI: 10.21203/rs.3.rs-1117933/v1.
279 A. Feng, S. Xie, X. Fu, Z. Chen and W. Zhu, *Front. Chem.*, 2021, **9**, 823868.
280 X. S. Geng, Q. X. Feng, R. Zhao, T. Hirtz, G. H. Dun, Z. Y. Yan, J. Ren, H. N. Zhang, R. R. Liang, H. Tian, D. Xie, Y. Yang and T. L. Ren, *IEEE Electron Device Lett.*, 2020, **41**, 256–259.
281 Z. Fan, J. Liu, W. Zuo, G. Liu, X. He, K. Luo, Q. Ye and C. Liao, *Phys. Status Solidi RRL*, 2020, **14**, 2000226.
282 Z. Xu, X. Liu, Y. Li, X. Liu, T. Yang, C. Ji, S. Han, Y. Xu, J. Luo and Z. Sun, *Angew. Chem., Int. Ed.*, 2019, **58**, 15757–15761.
283 X. Zhang, T. Zhu, C. Ji, Y. Yao and J. Luo, *J. Am. Chem. Soc.*, 2021, **143**, 20802–20810.
284 Y. Zhang, Y. Liu, Z. Xu, H. Ye, Z. Yang, J. You, M. Liu, Y. He, M. G. Kanatzidis and S. F. Liu, *Nat. Commun.*, 2020, **11**, 2304.
285 Y. Zhang, J. Hao, Z. Zhao, J. Pi, R. Shi, X. Li, N. Yuan, J. Ding, S. F. Liu and Y. Liu, *Adv. Mater.*, 2024, **36**, 2310831.
286 M. Chen, X. Dong, D. Chu, B. Jia, X. Zhang, Z. Zhao, J. Hao, Y. Zhang, J. Feng, X. Ren, Y. Liang, R. Shi, A. Najar, Y. Liu and S. F. Liu, *Adv. Mater.*, 2023, **35**, 2211977.
287 X. Song, G. Hodes, K. Zhao and S. F. Liu, *Adv. Energy Mater.*, 2021, **11**, 2003331.
288 X. Song, Q. Li, J. Han, C. Ma, Z. Xu, H. Li, P. Wang, Z. Yang, Q. Cui, L. Gao, Z. Quan, S. F. Liu and K. Zhao, *Adv. Mater.*, 2021, **33**, 2102190.

289 X. Song, T. Li, H. Li, S. Lin, J. Yin and K. Zhao, *Sci. China Mater.*, 2024, **67**, 1348–1355.
290 X. Song, H. Cohen, J. Yin, H. Li, J. Wang, Y. Yuan, R. Huang, Q. Cui, C. Ma, S. F. Liu, G. Hodes and K. Zhao, *Small*, 2023, **19**, 2300892.
291 S. Tie, D. Xin, S. Dong, B. Cai, J. Zhu and X. Zheng, *ACS Sustainable Chem. Eng.*, 2022, **10**, 10743–10751.
292 J. Guo, Y. Xu, W. Yang, B. Xiao, Q. Sun, X. Zhang, B. Zhang, M. Zhu and W. Jie, *ACS Appl. Mater. Interfaces*, 2021, **13**, 23928–23935.
293 M. Keshavarz, E. Debroye, M. Ottesen, C. Martin, H. Zhang, E. Fron, R. Kuchler, J. A. Steele, M. Bremholm, J. Van de Vondel, H. I. Wang, M. Bonn, M. B. J. Roeffaers, S. Wiedmann and J. Hofkens, *Adv. Mater.*, 2020, **32**, 2001878.
294 M. Daum, S. Deumel, M. Sytnyk, H. A. Afify, R. Hock, A. Eigen, B. Zhao, M. Halik, A. These, G. J. Matt, C. J. Brabec, S. F. Tedde and W. Heiss, *Adv. Funct. Mater.*, 2021, **31**, 2102713.
295 L. Yao, G. Niu, L. Yin, X. Du, Y. Lin, X. Den, J. Zhang and J. Tang, *J. Mater. Chem. C*, 2020, **8**, 1239–1243.
296 C. F. Wang, H. Li, Q. Ji, C. Ma, L. Liu, H. Y. Ye, B. Cao, G. Yuan, H. F. Lu, D. W. Fu, M. G. Ju, J. Wang, K. Zhao and Y. Zhang, *Adv. Funct. Mater.*, 2022, **32**, 2205918.
297 W. Guo, X. Liu, S. Han, Y. Liu, Z. Xu, M. Hong, J. Luo and Z. Sun, *Angew. Chem., Int. Ed.*, 2020, **59**, 13879–13884.
298 M. Xia, J. H. Yuan, G. Niu, X. Du, L. Yin, W. Pan, J. Luo, Z. Li, H. Zhao, K. H. Xue, X. Miao and J. Tang, *Adv. Funct. Mater.*, 2020, **30**, 1910648.
299 Z. Li, G. Peng, H. Chen, C. Shi, Z. Li and Z. Jin, *Angew. Chem., Int. Ed.*, 2022, **61**, 202207198.
300 J. Zhang, A. Li, B. Li, M. Yang, X. Hao, L. Wu, D. Zhao, G. Xia, Z. Ren, W. Tian, J. Yang and J. Zhang, *ACS Photonics*, 2022, **9**, 641–651.
301 H. Li, Y. Lei, G. Peng, Q. Wang, Z. Li, H. Wang, G. Wang and Z. Jin, *Adv. Funct. Mater.*, 2022, **32**, 2208199.
302 B. Yang, W. Pan, H. Wu, G. Niu, J. H. Yuan, K. H. Xue, L. Yin, X. Du, X. S. Miao, X. Yang, Q. Xie and J. Tang, *Nat. Commun.*, 2019, **10**, 1989.
303 L. Liu, S.-Y. Liu, Y. Shi, C.-L. Fang, S. Zhao, H.-Y. Shen, M.-X. Chen, Z.-J. Wang, Y. Ma, Y. Liu, Y. Feng, J. Tang, H.-Y. Ye and G. Niu, *Nat. Photonics*, 2024, **18**, 990–997.
304 J. Wu, S. You, P. Yu, Q. Guan, Z.-K. Zhu, Z. Li, C. Qu, H. Zhong, L. Li and J. Luo, *ACS Energy Lett.*, 2023, **8**, 2809–2816.
305 Z. Li, G. Peng, Z. Li, Y. Xu, T. Wang, H. Wang, Z. Liu, G. Wang, L. Ding and Z. Jin, *Angew. Chem., Int. Ed.*, 2023, **62**, e202218349.
306 Z. Li, Z. Li, G. Peng, C. Shi, H. Wang, S. Y. Ding, Q. Wang, Z. Liu and Z. Jin, *Adv. Mater.*, 2023, **35**, 2300480.
307 X. Li, G. Zhang, Y. Hua, F. Cui, X. Sun, J. Liu, H. Liu, Y. Bi, Z. Yue, Z. Zhai, H. Xia and X. Tao, *Angew. Chem., Int. Ed.*, 2023, **62**, e202315817.
308 K. Dong, H. Zhou, W. Shao, Z. Gao, F. Yao, M. Xiao, J. Li, Y. Liu, S. Wang, S. Zhou, H. Cui, M. Qin, X. Lu, C. Tao, W. Ke and G. Fang, *ACS Nano*, 2023, **17**, 1495–1504.
309 H. Li, X. Song, C. Ma, Z. Xu, N. Bu, T. Yang, Q. Cui, L. Gao, Z. Yang, F. Gao, G. Zhao, Z. Chen, Z. Ding, K. Zhao and S. Liu, *J. Energy Chem.*, 2022, **64**, 209–213.
310 P. Wang, M. Hu, H. Wang, Z. Chen, Y. Feng, J. Wang, W. Ling and Y. Huang, *Adv. Sci.*, 2020, **7**, 2001116.
311 P. Jia, M. Lu, S. Sun, Y. Gao, R. Wang, X. Zhao, G. Sun, V. L. Colvin and W. W. Yu, *Adv. Mater. Interfaces*, 2021, **8**, 2100441.
312 H. S. Jung, G. S. Han, N.-G. Park and M. J. Ko, *Joule*, 2019, **3**, 1850–1880.
313 Y. Liu, Y. Zhang, Z. Yang, H. Ye, J. Feng, Z. Xu, X. Zhang, R. Munir, J. Liu, P. Zuo, Q. Li, M. Hu, L. Meng, K. Wang, D.-M. Smilgies, G. Zhao, H. Xu, Z. Yang, A. Amassian, J. Li, K. Zhao and S. Liu, *Nat. Commun.*, 2018, **9**, 5302.
314 M. Xu, X. Wang, J. Weng, J. Shen, Y. Hou and B. Zhang, *Opt. Express*, 2022, **30**, 40611–40625.
315 J. Song, Q. Cui, J. Li, J. Xu, Y. Wang, L. Xu, J. Xue, Y. Dong, T. Tian and H. Sun, *Adv. Opt. Mater.*, 2017, **5**, 1700157.
316 G. Zhang, D. Wang, B. Lou, C. G. Ma, A. Meijerink and Y. Wang, *Angew. Chem., Int. Ed.*, 2022, **61**, e202207454.
317 Y. Ren, J. Hua, Z. Han, M. Sun and S. Lü, *Chem. Eng. J.*, 2023, **452**, 139160.
318 S. Mirershadi, S. Ahmadi-Kandjani, A. Zawadzka, H. Rouhbakhsh and B. Sahraoui, *Chem. Phys. Lett.*, 2016, **647**, 7–13.
319 J. C. Johnson, Z. Li, P. F. Ndione and K. Zhu, *J. Mater. Chem. C*, 2016, **4**, 4847–4852.
320 M. J. Sun, C. Zheng, Y. Gao, A. Johnston, A. M. Najarian, P. X. Wang, O. Voznyy, S. Hoogland and E. H. Sargent, *Adv. Mater.*, 2021, **33**, 2006368.
321 S. Liu, Z. Cheng, M.-Y. Li, S. Liu, H. Lu, X. Wen, C. Wang, X. Ding and L. Wang, *Matter*, 2024, **7**, 2810–2825.